

The galaxy cluster mass scale and its impact on cosmological constraints from the cluster population

G.W. Pratt · M. Arnaud · A. Biviano · D. Eckert · S. Ettori · D. Nagai · N. Okabe ·
T.H. Reiprich

Received: 31 December 2018 / Accepted: 14 February 2019

Abstract The total mass of a galaxy cluster is one of its most fundamental properties. Together with the redshift, the mass links observation and theory, allowing us to use the cluster population to test models of structure formation and to constrain cosmological parameters. Building on the rich heritage from X-ray surveys, new results from Sunyaev-Zeldovich and optical surveys have stimulated a resurgence of interest in cluster cosmology. These studies have generally found fewer clusters than predicted by the baseline *Planck* Λ CDM model, prompting a renewed effort on the part of the commu-

G.W. Pratt
 AIM, CEA, CNRS, Université Paris-Saclay, Université Paris Diderot,
 Sorbonne Paris Cité, F-91191 Gif-sur-Yvette, France
 E-mail: gabriel.pratt@cea.fr

M. Arnaud
 AIM, CEA, CNRS, Université Paris-Saclay, Université Paris Diderot,
 Sorbonne Paris Cité, F-91191 Gif-sur-Yvette, France

A. Biviano
 INAF-Osservatorio Astronomico di Trieste, via G.B. Tiepolo 11, 34143,
 Trieste, Italy

D. Eckert
 Max-Planck-Institut für extraterrestrische Physik, Giessenbachstrasse 1,
 85748 Garching, Germany

S. Ettori
 INAF-Osservatorio di Astrofisica e Scienza dello Spazio, via P. Gobetti
 93/3, 40129 Bologna, Italy,

D. Nagai
 Department of Physics, Yale University, PO Box 208101, New Haven,
 CT, USA
 Yale Center for Astronomy and Astrophysics, PO Box 208101, New
 Haven, CT, USA

N. Okabe
 Department of Physical Science, Hiroshima University, 1-3-1
 Kagamiyama, Higashi-Hiroshima, Hiroshima 739-8526, Japan

T. H. Reiprich
 Argelander Institute for Astronomy, University of Bonn, Auf dem Hügel
 71, 53121 Bonn, Germany

nity to obtain a definitive measure of the true cluster mass scale. Here we review recent progress on this front. Our theoretical understanding continues to advance, with numerical simulations being the cornerstone of this effort. On the observational side, new, sophisticated techniques are being deployed in individual mass measurements and to account for selection biases in cluster surveys. We summarise the state of the art in cluster mass estimation methods and the systematic uncertainties and biases inherent in each approach, which are now well identified and understood, and explore how current uncertainties propagate into the cosmological parameter analysis. We discuss the prospects for improvements to the measurement of the mass scale using upcoming multi-wavelength data, and the future use of the cluster population as a cosmological probe.

Keywords Galaxy clusters · Large-scale structure of the Universe · Intracluster matter · Cosmological parameters

Contents

1	Introduction	2
2	Theoretical insights from cosmological simulations	3
2.1	Dark matter density profiles	3
2.1.1	NFW model	3
2.1.2	Einasto model	3
2.1.3	Sparsity	4
2.2	The shape and distribution of dark matter and gas	4
2.3	ICM energy budget and departures from equilibrium	4
2.4	The presence of gas inhomogeneities	6
2.5	Baryon budget	7
2.5.1	Total baryonic content	7
2.5.2	Effect of non-gravitational processes	7
2.6	Mass estimates from mass proxies and scaling relations	7
3	Observational mass estimation methods	9
3.1	Kinematics	9
3.1.1	Methods	9
3.1.2	Sources of systematic uncertainty	11
3.2	X-ray and hybrid SZ	11

3.2.1	Method	11
3.2.2	Sources of systematic uncertainty	13
3.3	Weak lensing analysis	14
3.3.1	Method	15
3.3.2	Sources of systematic uncertainty	16
4	Recent advances	18
4.1	Lensing	18
4.1.1	Results from new samples	18
4.1.2	Mass and concentration	20
4.2	X-rays and hybrid SZ	22
4.2.1	Hydrostatic mass and mass profiles	22
4.2.2	New results from combination with SZ	23
4.2.3	Baryon budget and gas fraction	24
4.3	Non-thermal pressure, feedback, and the validity of the hydrostatic assumption	24
4.3.1	Constraints from X-ray and SZ observations	24
4.3.2	Constraints from X-ray and optical observations	25
4.4	Halo triaxiality	26
4.5	Mass estimates from mass proxies	26
5	Impact on cosmology with clusters	29
5.1	Clusters as cosmological probes and the sensitivity to the mass scale	29
5.1.1	The baryon fraction	29
5.1.2	The mass function	30
5.2	Recent results on cosmological constraints from galaxy clusters and their dependence on the mass determination	30
5.3	Summary and Interpretation	33
6	The future	33
6.1	New surveys and samples	33
6.1.1	X-ray	33
6.1.2	Microwave	34
6.1.3	Lensing and optical/IR	34
6.2	Next-generation data	35
6.2.1	eROSITA	35
6.2.2	Euclid and LSST	35
6.2.3	Simons Observatory and CMB-S4	37
6.2.4	XRISM and Athena	38
6.2.5	Studies	39
7	Summary	39

1 Introduction

Clusters of galaxies represent the highest-density peaks of the matter distribution in the Universe. Forming at the intersection of cosmic filaments, they grow hierarchically through continuous accretion of material. Composed of dark matter (DM; 85%), ionised hot gas in the intracluster medium (ICM; 12%), and stars ($\sim 3\%$), their matter content reflects that of the Universe. Their distribution in mass and redshift, and its evolution, allow us to probe both the physics of structure formation through gravitational collapse and the underlying cosmology in which this process takes place (e.g. Allen et al. 2011; Kravtsov & Borgani 2012). Thus together with the redshift, the mass of a cluster is its most fundamental property.

X-ray follow-up of objects in the *Röntgensatellit* (ROSAT) catalogues¹ allowed significant progress to be made on obtaining cosmological constraints from cluster number counts

(e.g. Borgani et al. 2001; Reiprich & Böhringer 2002; Vikhlinin et al. 2009a; Mantz et al. 2010b) and baryon fraction (e.g. Allen et al. 2008). From the beginning, such studies consistently indicated a low matter density, with a mean normalized matter density $\Omega_m \sim 0.3$, and a matter fluctuation amplitude $\sigma_8 \sim 0.7 - 0.8$. However, while the first cosmological constraints from Sunyaev-Zeldovich (SZ) cluster number count studies broadly confirmed these findings (Reichardt et al. 2013; Hasselfield et al. 2013; Planck Collaboration XX 2014), the high statistical precision of the *Planck*² Cosmic Microwave Background (CMB) measurements revealed an up to $\sim 2\sigma$ difference in the measurement of the key parameter σ_8 (Planck Collaboration XX 2014). A number of physical effects have been advanced to explain this discrepancy, including invoking ‘new physics’ (a massive neutrino component), but Occam’s Razor would suggest that the simplest explanation lies in uncertainties in the cluster mass scale.

A number of different methods can be used to obtain individual cluster masses. The most commonly used are galaxy kinematics (the use of galaxy orbits as tracers of the underlying potential), X-ray and SZ observations (using the distribution of the ICM as a probe of the potential), and lensing (using distortions of background galaxies to probe the intervening mass distribution). Each method has its inherent assumptions, and much work has gone into using numerical simulations to explore the possible biases that these assumptions might introduce into the final mass estimation.

When cluster surveys are used to trace the growth of structure and samples are defined for use as cosmological probes, it is not possible to obtain individual masses for every object. Furthermore, one must understand the probability that a cluster of a given mass is detected with a given value of the survey observable O (generally the X-ray or SZ signal, and more recently, the total optical richness), i.e. the relationship between O and the mass and the scatter about this relation. It is common practice to calibrate such a relationship for a limited number of objects, and then apply the resulting scaling law to the full sample. This approach has been successfully applied to a number of cluster samples. It requires accurate mass estimates of the calibration sample, and understanding of how the calibration and survey sample(s) map to the underlying population (i.e. knowledge of the sample selection function). While these uncertainties can be built into the marginalisation over cosmological parameters, tighter parameter constraints go hand in hand with our understanding of these issues.

The mass scale is thus fundamental for the study of clusters. This review aims to take stock of the current status of cluster mass estimation methods and its impact on cosmological parameter estimation using the cluster population, and to address the prospects for future improvements.

¹ <http://www.mpe.mpg.de/xray/wave/rosat/index.php>

² <https://www.cosmos.esa.int/web/planck>

2 Theoretical insights from cosmological simulations

Cosmological simulations have been a workhorse for making predictions for the structure and shape of dark matter haloes for more than twenty years (see e.g. Kravtsov & Borgani 2012; Planck et al. 2015, for reviews). Moreover, the abundance and clustering properties of dark matter haloes that form in the concordance cold dark matter (CDM) models are the standard against which observations are compared in order to derive cosmological constraints. Modern hydrodynamic simulations further provide insights into the effects of baryons on the dark matter halo properties, and on the internal structure of gas and stars within the dominant dark matter potential. In this Section we summarise a number of important insights that numerical simulations have provided for the interpretation of observational data.

The most commonly-used definition of mass, derived from theoretical studies but now used almost universally, is the three-dimensional mass enclosed within a given radius R_A inside which the mean interior density is Δ times the critical mass density, $\rho_c(z)$, at the redshift of the cluster. Alternatively, one can use Δ times the mean mass density $\rho_m(z) = \Omega_m(z)\rho_c(z)$. The standard notation expresses these quantities as

$$\begin{aligned} M_{\Delta c} &= \frac{4\pi}{3} \Delta \rho_c(z) R_{\Delta c}^3, \\ M_{\Delta m} &= \frac{4\pi}{3} \Delta \rho_m(z) R_{\Delta m}^3. \end{aligned} \quad (1)$$

One sometimes simply uses M_A and R_A for the former case. Commonly-used values of Δ in observational studies include 2500 (corresponding to the central parts of the halo), 500 (roughly equivalent to the virialised region that is accessible to the current generation of X-ray telescopes), and 200 (corresponding approximately to the ‘virial’ radius).

2.1 Dark matter density profiles

2.1.1 NFW model

The mass and internal structure of galaxy clusters reflect the properties of primordial density perturbations and the nature of the dark matter. In the standard hierarchical CDM scenario of cosmic structure formation, numerical simulations predict that dark matter haloes spanning a wide mass range can be well described by a universal mass density profile (Navarro et al. 1996, 1997). The so-called Navarro-Frenk-White (NFW) profile is expressed in the form:

$$\rho_{\text{NFW}}(R) = \frac{\rho_s}{(R/R_s)(1+R/R_s)^2}, \quad (2)$$

where ρ_s is the central density parameter and R_s is the scale radius that divides the two distinct regimes of asymptotic mass density slopes $\rho \propto R^{-1}$ and R^{-3} .

The NFW profile is fully specified by two parameters: M_A and the halo concentration $c_A = R_A/R_s$. The three-dimensional spherical mass, M_A , enclosed by the radius, R_A , is given by

$$M_{\text{NFW}}(< R_A) = \frac{4\pi\rho_s R_A^3}{c_A^3} \left[\ln(1 + c_A) - \frac{c_A}{1 + c_A} \right]. \quad (3)$$

As the central density reflects the mean density of the Universe at the time of formation, haloes with increasing mass are expected to have lower mass concentration at a given redshift (e.g. Navarro et al. 1997; Bullock et al. 2001; Gao et al. 2004; Dolag et al. 2004; Duffy et al. 2008; Stanek et al. 2010a; Klypin et al. 2011; Bhattacharya et al. 2013; Meneghetti et al. 2014; Ludlow et al. 2014; Diemer & Kravtsov 2015).

Numerical simulations usually describe the relation between the mass and the NFW concentration (i.e. the $c - M$ relation) for simulated haloes using a power-law function (e.g. Bhattacharya et al. 2013; Meneghetti et al. 2014; Diemer & Kravtsov 2015). This relation exhibits large intrinsic scatter for a given halo mass owing to the wide distribution in formation times (e.g. Neto et al. 2007) and the evidence that not all systems are well described by a NFW model (e.g. Jing 2000). Recently, Diemer & Kravtsov (2015) have proposed that a seven-parameter, double power-law functional form computed by peak height and the slope of the linear matter power spectrum can describe concentrations in the fiducial Λ CDM cosmology with 5% accuracy.

Although non-baryonic dark matter exceeds baryonic matter by a factor of $\Omega_{\text{DM}}/\Omega_b \approx 6$ on average, the gravitational field in the central regions of galaxies is dominated by stars. In the hierarchical galaxy formation model the stars are formed in the condensations of cooling baryons in the halo centre. As the baryons condense in the centre, they pull the dark matter particles inward thereby increasing their density in the central region. The response of dark matter to baryonic infall has traditionally been calculated using the model of adiabatic contraction (Eggen et al. 1962), which has also been tested and/or calibrated numerically using both idealised (Ryden & Gunn 1987; Blumenthal et al. 1986) and cosmological simulations (Gnedin et al. 2004; Rudd et al. 2008; Duffy et al. 2008; Velliscig et al. 2014; Shirasaki et al. 2018).

2.1.2 Einasto model

Recent high-resolution N-body simulations (e.g. Navarro et al. 2004; Gao et al. 2012) indicate that an Einasto profile (Einasto 1965) better describes the spherically averaged mass density profile for dark matter haloes than the NFW profile. The Einasto profile has the form:

$$\rho_{\text{Einasto}} = \rho_{-2} \exp \left(-\frac{2}{\alpha} \left[\left(\frac{R}{R_{-2}} \right)^\alpha - 1 \right] \right) \quad (4)$$

where α is a shape parameter that describes the degree of curvature of the profile, and ρ_{-2} and R_{-2} are a mass density

and a scale radius at which the logarithmic slope is -2 , respectively. The NFW model corresponds to a $\alpha \sim 0.18$ case for the Einasto profile. The spherical mass enclosed within R_A is given by

$$M_A = 4\pi\rho_{-2} R_{-2}^3 \frac{1}{\alpha} \left(\frac{2}{\alpha}\right)^{-3/\alpha} \times \exp(2/\alpha) \left[\Gamma\left(\frac{3}{\alpha}\right) - \Gamma\left(\frac{3}{\alpha}, \frac{2}{\alpha} \left(\frac{R_A}{R_{-2}}\right)^\alpha\right) \right], \quad (5)$$

where $\Gamma(x)$ and $\Gamma(a, x)$ are the gamma function and the upper incomplete gamma function, respectively. The Einasto profile is specified by the three parameters M_A , $c_A = R_A/R_{-2}$, and α .

2.1.3 Sparsity

An alternative to a parameterised description of the dark matter profile is the use of the halo sparsity, s_A . This quantity measures the ratio of halo masses at two different overdensities:

$$s_{A_1 A_2} = M_{A_1}/M_{A_2} \quad (6)$$

and has been recently proposed as new cosmological probe for galaxy clusters (Balmès et al. 2014; Corasaniti et al. 2018). If the halo follows a NFW profile, the sparsity and concentration are directly related. However, halo sparsity has the key feature that the ensemble average value at a given redshift exhibits much smaller scatter than that of the mass concentration, and does not require any modelling of the mass density profile, but only the mass measurements within two overdensities. It is thus also an attractive quantity for comparison with observations.

2.2 The shape and distribution of dark matter and gas

Although the above discussion assumes spherical symmetry, the CDM model predicts that cluster-size dark matter haloes are generally triaxial and are elongated along the direction of their most recent major mergers (e.g. Thomas et al. 1998; Jing & Suto 2002; Hopkins et al. 2005; Kasun & Evrard 2005; Bett et al. 2007; Gottlöber & Yepes 2007). The degree of triaxiality is correlated with the halo formation time (e.g. Allgood et al. 2006), suggesting that at a given epoch more massive haloes are more triaxial. For the same reason, triaxiality is sensitive to the linear structure growth function and is higher in cosmological models in which haloes form more recently (Macciò et al. 2008). Furthermore, inclusion of baryons in simulations modifies the shapes of cluster-size dark matter haloes, causing them to become rounder due to gas dissipation associated with galaxy formation processes (e.g. Kazantzidis et al. 2004).

Lau et al. (2011) showed that gas traces the shape of the underlying potential rather well outside the core, as expected

if the gas were in hydrostatic equilibrium (HE hereafter) in the cluster potential, but that the gas and potential shapes differ significantly at smaller radii. These simulations further suggest that with radiative cooling, star formation and stellar feedback (CSF) intracluster gas outside the cluster core ($R \gtrsim 0.1 R_{500}$) is more spherical compared to non-radiative simulations, while in the core the gas in the CSF runs is more triaxial and has a distinctly oblate shape. The latter reflects the ongoing cooling of gas, which settles into a thick oblate ellipsoid as it loses thermal energy. In the CSF runs, the difference reflects the fact that gas is partly rotationally supported. In non-radiative simulations the difference between gas and potential shape at small radii is due to random gas motions, which make the gas distribution more spherical than the equipotential surfaces. Results are similar for unrelaxed clusters but with considerable scatter. In both CSF and non-radiative runs, the gravitational potential was found to be much more spherical than DM.

Stochastic feedback from a central active galactic nucleus (AGN) will also heat and redistribute the gas in the core regions (e.g. Le Brun et al. 2014; Truong et al. 2018). Due to their shallower potential wells, such feedback has a stronger effect on the gas distribution of lower mass systems, leading to a radial and mass dependent modification of the gas content in the core regions.

2.3 ICM energy budget and departures from equilibrium

The deep potential well of galaxy clusters compresses the collapsing baryons (consisting mostly of pristine hydrogen and helium with densities of $\sim 10^3$ particle cm $^{-3}$), and heats them to temperatures of 10^7 K (~ 1 keV) and above. Given its high temperature, the ICM emits in X-rays principally via thermal Bremsstrahlung, with a continuum emission typically following $\epsilon \propto n_{\text{gas}}^2 T^{1/2}$. Inverse Compton scattering of CMB photons by ICM electrons produces the SZ effect that is observed in millimetric bands (Sunyaev & Zeldovich 1972). The SZ signal is proportional to the electron pressure integrated along the line-of-sight.

The spatial distribution and thermodynamical properties of the ICM depend on the underlying dark matter potential and the merging history of a cluster. From a general point of view, the dynamics of an inviscid collisional gas follows the Euler equation,

$$\frac{\partial \mathbf{v}}{\partial t} + (\mathbf{v} \cdot \nabla) \mathbf{v} + \frac{1}{\rho} \nabla P = -\nabla \Phi \quad (7)$$

where \mathbf{v} denotes the three-dimensional velocity field, P, ρ are the gas pressure and density, and Φ the cluster gravitational potential. After few sound crossing times of the order of 10^9 years, the ICM is expected to reach HE, and the kinetic energy thermalises, such that the pressure support should be dominated by the thermal pressure ($P \approx P_{\text{th}}$). The velocity

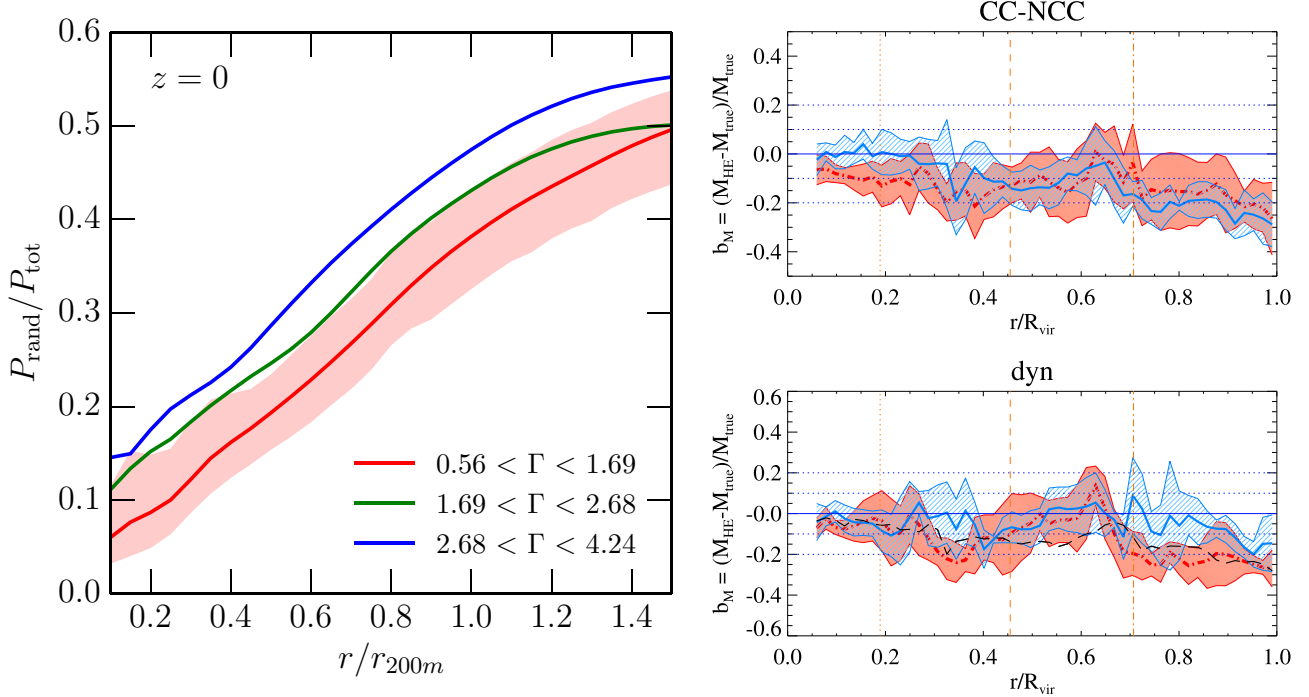


Fig. 1 *Left:* Random-to-thermal pressure ratio for simulated clusters from the Ω_{500} simulation (reproduced from Nelson et al. 2014a). The various curves show the median non-thermal pressure profiles sorted by a proxy for the mass accretion rate Γ defined as the difference in mass between $z = 0.5$ and $z = 0$ (Diemer & Kravtsov 2014). *Right:* Hydrostatic mass bias $b_M = (M_{\text{HSE}} - M_{\text{true}})/M_{\text{true}}$ as a function of radius for a sample of 29 clusters simulated with the SPH code GADGET-3 (reproduced from Biffi et al. 2016). The two panels show the radial profiles of b_M sorted by the system core state, where CC indicates cool core and NCC denotes non-cool core objects (top), and dynamical state (bottom). The shaded areas show the dispersion around the median.

field becomes negligible and the Euler equation reduces to the HE equation,

$$\frac{1}{\rho} \frac{dP_{\text{th}}}{dr} = -\frac{GM(< R)}{R^2}, \quad (8)$$

where G is the gravitational constant. Under this assumption, the mass profile can be reconstructed from the radial profiles of ICM thermodynamic quantities (see Sect. 3.2).

However, residual random gas motions can produce a non-negligible contribution to balance the gravitational field, which causes an underestimation of the true mass when the energy is assumed to be fully thermalised. The total pressure balancing gravity can be described as the sum of thermal pressure and random kinetic pressure,

$$P_{\text{tot}} \simeq P_{\text{th}} + \frac{1}{3} \rho \sigma_v^2, \quad (9)$$

where σ_v denotes the velocity dispersion of isotropically moving gas particles (i.e. turbulent motions). More generally, by integrating the Eqn. 7 over a radial shell, the total enclosed mass within the radius R can be written as,

$$M(< R) = M_{\text{therm}} + M_{\text{rand}} + M_{\text{rot}} + M_{\text{cross}} + M_{\text{stream}} + M_{\text{accel}}, \quad (10)$$

where the expressions for all six terms are given in Lau et al. (2013). The first term in the equation is the hydrostatic mass (see Eqn. 21). The second and third terms indicate the pressure support induced by random and rotational gas motions, respectively. The fourth and fifth terms describe the contribution from cross and stream motions; the final term is the acceleration.

Each of these additional terms will introduce corrections to the HE assumption and need to be properly understood in order to derive accurate masses from the hydrostatic method. Given the difficulty of directly measuring gas motions in the ICM³, numerical simulations have been widely exploited to set constraints on the relative importance of each of these terms (Rasia et al. 2006; Nagai et al. 2007; Vazza et al. 2009; Lau et al. 2009; Nelson et al. 2012; Battaglia et al. 2012; Suto et al. 2013; Rasia et al. 2014; Nelson et al. 2014a,b; Biffi et al. 2016; Shi et al. 2015, 2016). Most studies consistently predict that random residual gas motions (i.e. turbulence) dominate the required correction, independent of the dynamical state. The amplitude of the turbulent pressure support, however, varies from cluster-to-cluster, with predictions in the range of 10 – 30% at R_{500} depending on the mass accretion histories

³ Existing experimental constraints and future prospects on gas motions in the ICM are discussed in detail in another chapter of this series Simionescu et al. (2019).

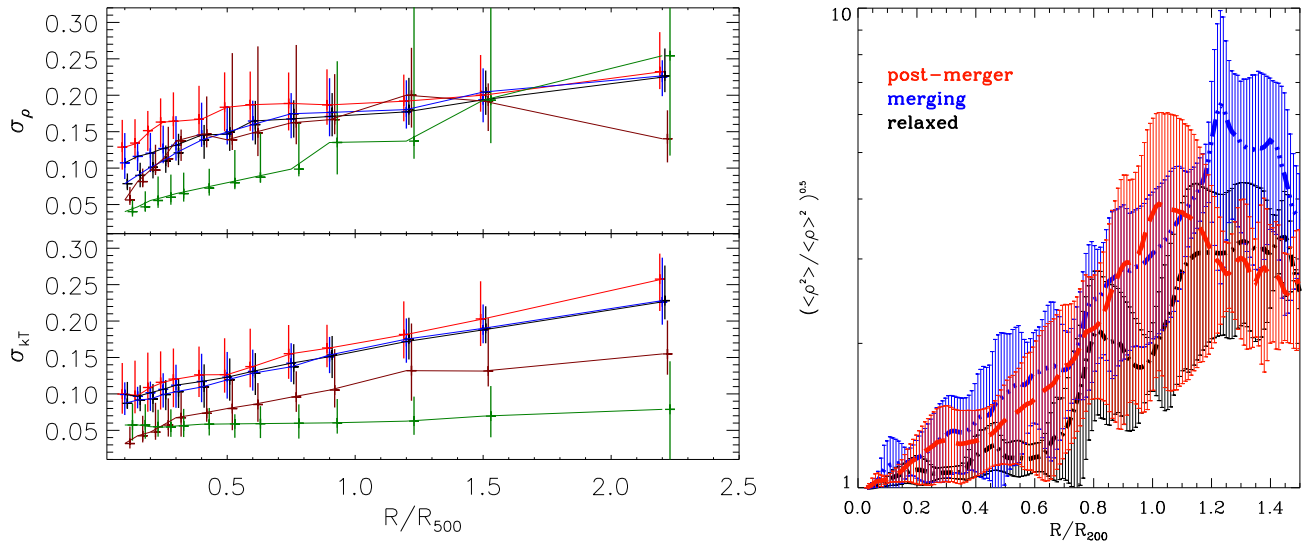


Fig. 2 *Left:* A measure of the predicted inhomogeneity in the gas density and temperature distributions. The Figure shows the average width of the distribution of gas density (top) and temperature (bottom) within spherical shells for five different simulation setups (reproduced from [Rasia et al. 2014](#)). The colours refer to the following runs: non-radiative SPH (red), non-radiative AMR (brown), SPH with cooling and star formation (blue), AMR with cooling and star formation (green), and SPH with AGN feedback (black). *Right:* Radial profiles of gas clumping factor $C = (\langle \rho^2 \rangle / \langle \rho \rangle^2)^{1/2}$ estimated from non-radiative AMR simulations of a set of massive clusters (reproduced from [Vazza et al. 2013](#)). The simulated systems are sorted into relaxed (black), merging (blue), and post-merger (red) categories.

of clusters ([Nelson et al. 2014a; Shi et al. 2015, 2016](#)). Bulk motions and acceleration provide an important contribution only in merging clusters. Note that the acceleration term is very small within the virialised regions of galaxy clusters, but becomes a non-negligible and irreducible mass bias in merging clusters or the outskirts of all clusters ([Lau et al. 2013; Suto et al. 2013; Nelson et al. 2014b](#)).

Figure 1 shows the radial profiles of non-thermal pressure and hydrostatic mass bias from two different sets of simulations ([Nelson et al. 2014a; Biffi et al. 2016](#)). Both studies predict a trend of increasing non-thermal-to-thermal pressure ratio with radius, and hydrostatic mass biases ranging from $< 5\%$ in the core to $\sim 30\%$ at R_{500} . Both studies also find a dependence of the predicted hydrostatic mass bias on the cluster dynamical state and accretion rate, the non-thermal pressure contribution being on average higher in highly accreting systems. The relatively low-values of the non-thermal pressure derived from the X-COP data (in Sect. 4.3.1) are consistent with the expectation that relaxed clusters have the lower level of non-thermal pressure support. Future work should focus on detailed understanding of the nature of gas flows in the density-stratified ICM in cluster outskirts ([Shi et al. 2018; Vazza et al. 2018](#)).

2.4 The presence of gas inhomogeneities

In practice, interpretation of X-ray measurements of the thermodynamical properties of the ICM may be complicated by the presence of structure and inhomogeneities in the gas

temperature and density distributions ([Mazzotta et al. 2004; Vikhlinin 2006](#)). Unfortunately, numerical simulations have not yet converged on what the typical level of temperature inhomogeneities in the ICM should be, as the result appears to depend substantially on the adopted physical and computational setup. The two main hydrodynamical solvers in numerical simulations of clusters are Smoothed Particle Hydrodynamics (SPH) and Adaptive Mesh Refinement (AMR). [Rasia et al. \(2014\)](#) compared the predicted level of temperature anisotropies in five sets of numerical simulations featuring both SPH and AMR hydrodynamical solvers, and for different implementations of baryonic physics (non-radiative, cooling and star formation, and AGN feedback). The predicted level of temperature inhomogeneity ranges from 5 to 25% (see Fig. 2).

Similarly, the gas density determined from X-ray observations of the ICM may be biased by the presence of inhomogeneities in the gas distribution of the ICM. Over-dense regions exhibit an enhanced X-ray signal because of the ρ^2 dependence of the emissivity, which boosts the estimated gas density towards high values ([Mathiesen et al. 1999](#)). The overestimation of the gas density is usually quantified by the clumping factor $C = (\langle \rho^2 \rangle / \langle \rho \rangle^2)^{1/2} \geq 1$. Numerical studies predict that the clumping factor C should increase from values close to 1 in the central regions to 1.2 – 1.3 around R_{200} ([Nagai & Lau 2011; Vazza et al. 2013; Roncarelli et al. 2013; Zhuravleva et al. 2013; Planelles et al. 2017](#)), with substantial scatter from one system to another. As an example, the right-hand panel of Fig. 2 shows the radial profiles of the

clumping factor in a set of 20 massive clusters simulated with the AMR code Enzo and sorted according to their dynamical state, showing that the ICM in merging systems is on average more clumpy than in relaxed objects (Vazza et al. 2013). The HE equation in the presence of clumping should be modified by the gradient of the clumping factor (Roncarelli et al. 2013), neglect of which can cause biases of $\sim 5\%$ on the reconstructed masses. Note that the effect of clumping on the gas fraction is expected to be larger, as it biases simultaneously the gas mass high and the hydrostatic mass low. The corresponding values of f_{gas} can be overestimated by $\sim 10\%$ at R_{500} (Eckert et al. 2015).

2.5 Baryon budget

2.5.1 Total baryonic content

Because of their large mass and deep gravitational potential, the total baryon content in galaxy clusters is expected to reflect that of the Universe as a whole (White et al. 1993; Evrard 1997; Kravtsov et al. 2005). The total baryon fraction $f_b = (M_{\text{gas}} + M_{\star})/M_{\text{tot}}$ should thus match the cosmic baryon fraction estimated from primordial nucleosynthesis and the CMB power spectrum. Simulations using different hydrodynamical solvers and baryonic physics substantially agree in predicting that the depletion of baryons within R_{200} during the hierarchical formation process should be small ($\sim 5\%$, Planelles et al. 2013; Sembolini et al. 2013; Le Brun et al. 2014; Wu et al. 2015; Sembolini et al. 2016a,b; Hahn et al. 2017; Barnes et al. 2017, 2018; Lovell et al. 2018). In particular, Sembolini et al. (2016a) resimulated the region surrounding a massive cluster ($M_{\text{vir}} = 1.1 \times 10^{15} M_{\odot}$) with 13 different hydrodynamical codes from the exact same initial conditions and compared the output. The comparison includes classical SPH (GADGET-2), advanced SPH (GADGET-3), AMR (ART, RAMSES), and moving-mesh (AREPO) codes. In the left-hand panel of Fig. 3 the baryon fraction of the simulated cluster is shown as a function of radius. While in the central regions and out to ~ 300 kpc the various codes do not converge, around R_{500} and beyond they agree within a few percent. Thus, the baryon fraction within R_{200} is very robustly predicted by numerical simulations, independent of the exact input physics or the numerical scheme.

2.5.2 Effect of non-gravitational processes

Various works have also studied the impact of baryonic physics (cooling, star formation, supernova and AGN feedback) on the depletion of baryons within the virial radius. In the case where a large amount of non-gravitational energy is injected within the ICM, the gaseous atmosphere expands and a global depletion of baryons within the virial

radius may occur. AGN feedback is the main source of non-gravitational energy in the ICM (see McNamara & Nulsen 2007, for a review). The baryon depletion caused by AGN feedback is known to be important for haloes with masses below $\sim 10^{14} M_{\odot}$ (Planelles et al. 2013; Le Brun et al. 2014; Wu et al. 2015; Lovell et al. 2018), for which the baryon budget falls short of the cosmic value by a factor ~ 2 . The right-hand panel of Fig. 3 from Le Brun et al. (2014) shows the hot gas fraction in several sets of numerical simulations implementing various prescriptions for baryonic physics (non-radiative, cooling and star formation, and three models for AGN feedback) and compares the results with published datasets. While the non-radiative run predicts little depletion for haloes in the range $10^{13} - 10^{15} M_{\odot}$, the runs implementing additional physics largely differ for haloes of $M_{500} \leq 10^{14} M_{\odot}$. Note that the run including cooling and star formation but no AGN feedback suffers from the overcooling problem, and predicts stellar fractions that are largely in excess of the measured values. At high mass ($M_{500} \sim 10^{15} M_{\odot}$), all but the most extreme AGN feedback model converge to a very similar value for the hot gas fraction, indicating that baryonic effects are subdominant.

2.6 Mass estimates from mass proxies and scaling relations

The gravitational potential of galaxy clusters can be probed through observations of the ICM in X-rays and the SZ effect, or through the richness in optical/NIR wavelengths. One expects simple scaling relations between the mass and global ICM properties such as the X-ray luminosity, L_X , or the SZ Compton parameter Y_{SZ} , and galaxy content. More specifically, the simplest models of structure formation, based on simple gravitational collapse, predict that galaxy clusters constitute a self-similar population. As discussed above (Eqn. 1), the virialised part of a cluster corresponds roughly to a fixed density contrast ($\Delta \sim 500$) as compared to the critical density of the Universe, $\rho_c(z)$ at the redshift in question:

$$\frac{M_{\Delta}}{\frac{4\pi}{3} R_{\Delta}^3} = \Delta \rho_c(z) \quad (11)$$

with a strong similarity in the internal structure of virialised dark matter haloes within the corresponding radius, R_{Δ} . This reflects the fact that there is no characteristic scale in the gravitational collapse. The gas properties directly follow from the dark matter properties, assuming that the gas evolution is purely driven by gravitation, i.e. by the evolution of the dark matter potential. The internal gas structure is universal, as is the case for the dark matter. The gas mass fraction f_{gas} reflects the Universal value, since the gas 'follows' the collapse of the dark matter. It is thus constant:

$$\frac{M_{\text{gas},\Delta}}{M_{\Delta}} = f_{\text{gas}} = \text{const.} \quad (12)$$

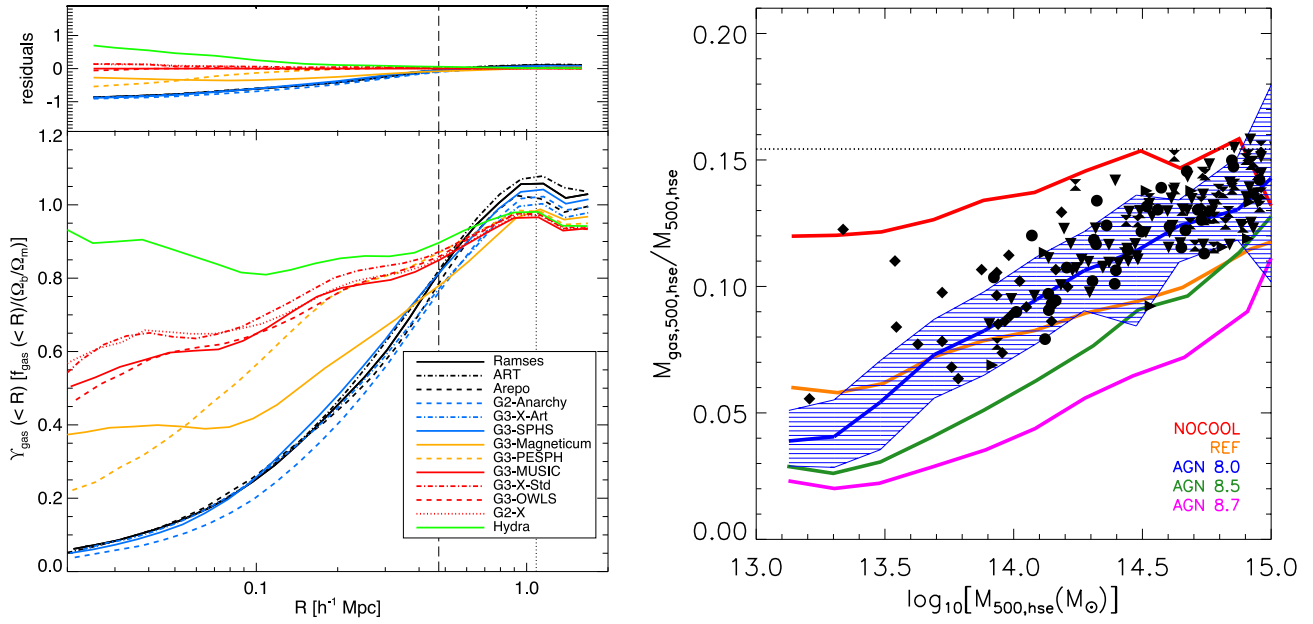


Fig. 3 *Left:* Baryon fraction profiles for a massive galaxy cluster resimulated with 13 different codes from the same initial condition. The dotted vertical line indicates the value of R_{500} . Figure from Sembolini et al. (2016a). *Right:* ICM gas fraction profiles as a function of halo mass in simulations implementing various prescriptions for baryonic physics (non-radiative, red; cooling and star formation, yellow; AGN feedback, blue and magenta). The AGN feedback models range from gentle, self-regulated feedback (AGN 8.0, blue) to more bursty and energetic injection (AGN 8.7, magenta). The black points show a compilation of observed ICM gas fraction measurements. Figure from Le Brun et al. (2014).

Furthermore, as the gas is roughly in HE in the potential of the dark matter, the virial theorem gives:

$$T_X = \beta \frac{G \mu m_p M_A}{R_A} \quad (13)$$

where μ is the mean molecular weight in amu for an ionised plasma, m_p is the proton mass, T_X is the gas mean temperature, and β is a normalization factor which depends on the cluster internal structure. Since this structure is universal, β is a constant, independent of redshift z and cluster mass.

Each cluster can therefore be defined by two parameters only: its mass and its redshift. From the basic equations, Eqn. 11-13, one can derive a scaling law for each physical property, Q , of the form $Q \propto A(z) M_A^\alpha$, that relates it to the redshift and mass. The evolution factor, $A(z)$, in the scaling relations is due to the evolution of the mean dark matter (and thus gas) density, which varies with the critical density of the Universe, $\bar{\rho}_{\text{gas}} \propto \bar{\rho}_{\text{DM}} = A \rho_c(z) \propto E^2(z)$. For instance, the gas mass scales as $M_{\text{gas},A} \propto M_A$, the temperature as $T_X \propto E^{2/3}(z) M_A^{2/3}$. The integrated SZ signal Y_{SZ} , or its X-ray equivalent $Y_X = M_{\text{gas},A} T_X$, introduced by Kravtsov et al. (2006), scales as $Y_{\text{SZ}} \propto E^{2/3}(z) M_A^{5/3}$, while the (bolometric) X-ray luminosity scales as $L_X \propto E(z)^{7/3} M_A^{4/3}$.

These scaling relations then allow estimation of the mass through so-called mass proxies, i.e. global physical properties, directly related to the mass, but easier to measure. However, there are intrinsic limitations to these 'cheap' mass estimates. Even in the simplest, purely gravitational model,

the normalisation of the relations depends on the formation history, and must be derived from numerical simulations. Furthermore, each relation has an intrinsic scatter due to individual cluster formation histories (Poole et al. 2007; Yu et al. 2015). Even more importantly, non gravitational physics (cooling and galaxy/AGN feedback) affects the normalisation, slope, scatter, and evolution of each relation. In particular, as L_X and Y_{SZ} depend on the gas content, the slope of the $L_X - M$ and $Y_{\text{SZ}} - M$ relations is directly affected by the mass dependence of the baryon depletion (Sec. 2.5.2). A large numerical simulation effort has been undertaken to understand how these scaling relations depend on the gas physics (e.g. Pike et al. 2014; Planelles et al. 2014; Le Brun et al. 2014; Truong et al. 2018), including their scatter and evolution (Le Brun et al. 2017). There is now a consensus that AGN feedback is a key ingredient of realistic models. A key recent advance is the development of new cosmological hydrodynamical simulations, with calibrated sub-grid feedback models that are able to reproduce the observed gas and stellar properties of local clusters (McCarthy et al. 2017).

The most robust mass proxies correspond to the lowest-scatter relations that depend as little as possible on the gas physics. In this respect, the SZ signal, proportional to the integral of the pressure, or equivalently to the total thermal energy of the gas, is generally believed to be particularly well-behaved (e.g. da Silva et al. 2004; Motl et al. 2005). The SZ signal and the corresponding pressure profiles beyond the core are mostly governed by the characteristics of the

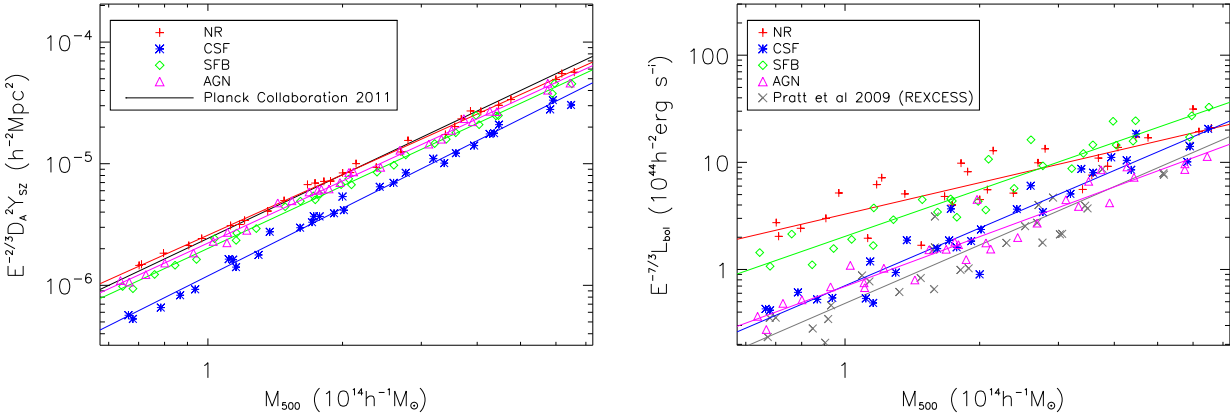


Fig. 4 Relation between the SZ signal (left) or the X-ray luminosity (right) and the mass from the numerical simulations of Pike et al. (2014). Observational data points are from Planck Collaboration XI (2011) and Pratt et al. (2009). The relations are plotted for different implementation of the gas physics: the non-radiative model (NR, red crosses), cooling and star formation model (CSF; blue stars), supernova feedback (SFB; green diamonds) and AGN models (magenta triangles). These relations are compared to observations (black line and black crosses). The Y_{SZ} is proportional to the total thermal energy and the relation between Y_{SZ} and the mass depends weakly on cooling and feedback processes. The scatter is tight, reflecting the similarity in shape of the pressure profiles. In contrast, the X-ray luminosity depends on the square of the density and is dominated by the core properties. It is very sensitive to gas physics and presents a large scatter at a given mass, reflecting the large scatter in the scaled density profile in the core of clusters.

underlying potential well, with a weak dependence on dynamical state and on the poorly-understood non-gravitational physics. Y_{SZ} is thus considered to be a robust, low scatter mass proxy. In contrast, the X-ray luminosity is more complex. The X-ray flux is sensitive to core properties, which presenting a large scatter and a strong dependence on thermodynamical state (Fig. 4). The gas mass may be a good mass proxy for the most massive systems, but not at low mass where it is strongly dependent on galaxy feedback. A recent comparison of the properties of various mass proxies, seen from the point of view of numerical simulations, can be found in Le Brun et al. (2017). Improved understanding of covariances among different observables is one of the important steps toward improving constraining power of upcoming multi-wavelength cluster surveys (e.g. Stanek et al. 2010b; Shirasaki et al. 2016).

3 Observational mass estimation methods

In this Section, we discuss the principal methods that are used to estimate individual cluster masses. Each method is briefly described, along with its underlying assumptions, and the various systematic uncertainties and potential biases that can be encountered in translating the observation into a mass measurement are discussed.

3.1 Kinematics

The first estimate of the mass of a cluster of galaxies (Zwicky 1933, 1937) was obtained by applying the virial theorem to the distribution of cluster galaxies in projected phase-space

(PPS), and it was based on the assumption that galaxies are unbiased tracers of the cluster mass distribution. If this assumption is relaxed, the virial mass estimate can vary by an order of magnitude or more (Merritt 1987; Wolf et al. 2010). It is therefore important not to make any assumption on the relative distribution of the cluster mass and the galaxies, even if several studies have shown that red, passive galaxies do indeed trace the total mass profile of clusters (e.g. van der Marel et al. 2000; Biviano & Girardi 2003). Observational selection tends to make the bias in the spatial distribution stronger than the bias in the velocity distribution (Biviano et al. 2006), so it is more robust to estimate a cluster mass directly from the velocity distribution of cluster galaxies, using a scaling relation (e.g. Evrard et al. 2008; Munari et al. 2013; Ntampaka et al. 2015), rather than using the virial theorem. The intrinsic scatter of the mass-velocity dispersion relation is $\leq 5\%$, but observational effects (see Sect. 3.1.2) increase the scatter to $\sim 40\%$ (White et al. 2010; Saro et al. 2013).

3.1.1 Methods

If $\gtrsim 100$ tracers of the cluster gravitational potential are available, cluster masses and mass profiles can be determined without any assumption about the spatial and/or velocity distribution of the tracers relative to the mass. One possibility is to relate the observed PPS distribution of galaxies to their intrinsic phase-space distribution via (see, e.g., Dejonghe & Merritt 1992)

$$g(R, v_{\text{los}}) = 2 \int_R^\infty \frac{r dr}{(r^2 - R^2)^{1/2}} \int_{-\infty}^{+\infty} \int_{-\infty}^{+\infty} f(E, L) dv_\theta dv_R, \quad (14)$$

where r is the radial distance from the cluster centre in 3D, (v_R, v_θ) are Cartesian components of the velocity along the polar coordinates (R, θ) in the plane of the sky, and v_{los} is the line-of-sight velocity component (i.e. the one we observe via the redshift measurement). The intrinsic phase-space distribution f is expressed in terms of the energy E and angular momentum L . The gravitational potential is related to $f(E, L)$ through the Poisson equation. Since the shape of the $f(E, L)$ distribution function is not known from theory, it is generally estimated for haloes extracted from cosmological simulations (Wojtak et al. 2008, 2009). The $f(E, L)$ method has been used to estimate the mass profiles $M(r)$ of 41 nearby clusters by Wojtak & Łokas (2010) and a stack of sixteen $z = 0.17 - 0.55$ clusters by van der Marel et al. (2000).

Another widely adopted method for the $M(r)$ determination is to search for a solution of the Jeans equation for a collisionless system of galaxies in dynamical equilibrium,

$$G M(r) = -r \langle v_r^2 \rangle \left(\frac{d \ln \nu}{d \ln r} + \frac{d \ln \langle v_r^2 \rangle}{d \ln r} + 2\beta \right). \quad (15)$$

where $\nu(r)$ is the cluster 3d galaxy number density profile, and $\langle v_r^2 \rangle$ is the mean squared radial velocity component, that reduces to the radial velocity dispersion σ_r in the absence of bulk motions. $\beta(r)$ is the velocity anisotropy profile,

$$\beta(r) \equiv 1 - \frac{\langle v_\theta^2 \rangle}{\langle v_r^2 \rangle}, \quad (16)$$

where $\langle v_\theta^2 \rangle$ is the mean squared velocity component along one of the two tangential directions in spherical coordinates, that reduces to the tangential velocity dispersion σ_θ in the absence of bulk motions. Since most clusters of galaxies do not rotate (Hwang & Lee 2007), it is usually assumed that the two tangential components of the velocity are identical. The Abel integral equation relates $\nu(r)$ to the observable (projected) galaxy number density profile $N(R)$ (Binney & Tremaine 1987), under the assumption of spherical symmetry. On the other hand, one cannot directly determine $\sigma_r(r)$ from the observable $\sigma_{\text{los}}(R)$, since knowledge of $\beta(r)$ is required. This is the so-called *mass-anisotropy degeneracy* (MAD hereafter, Binney & Mamon 1982) and it is the critical point of this method. To solve the MAD, one can use the mean $\beta(r)$ of cluster-size haloes extracted from cosmological simulations (Mamon et al. 2010; Lau et al. 2010); $M(r)$ then follows directly from the observables in a non-parametric approach (Mamon & Boué 2010; Wolf et al. 2010). Other possibilities to solve the MAD problem is to use the fourth-order (kurtosis) Jeans equation (Łokas 2002; Łokas & Mamon 2003; Richardson & Fairbairn 2013), or to separately solve the Jeans equation for different tracers, e.g. early-type and late-type galaxies, since they may have different $\beta(r)$ for the same $M(r)$ (Battaglia et al. 2008; Biviano & Poggianti 2009). The Jeans equation has been used to determine $M(r)$ of many individual clusters or stacks of several clusters (e.g. Carlberg

et al. 1997; Biviano & Girardi 2003; Łokas & Mamon 2003; Katgert et al. 2004; Biviano & Poggianti 2009; Lemze et al. 2009).

MAMPOSSt (*Modelling of Anisotropy and Mass Profiles of Observed Spherical Systems*, Mamon et al. 2013) is a hybrid method that solves the Jeans equation Eqn. (15) to compute the probability of observing a galaxy in a given (R, v_{los}) position in PPS, by assuming models for $M(r)$ and $\beta(r)$ and a shape (e.g. a Gaussian) for the 3D velocity distribution (and not, as is usually done, for the line-of-sight velocity). The probability of observing a galaxy with velocity v_{los} at the projected radius R is:

$$p(v_{\text{los}}|R) = (2\pi)^{-1/2} \times \int_0^\infty (\nu/\sigma_{\text{los}}) \exp[-v_{\text{los}}^2/(2\sigma_{\text{los}}^2)] dz / \int_0^\infty \nu dz, \quad (17)$$

where z is the direction of the line-of-sight. The 3D number density profile $\nu(r)$ comes from the observed (projected) number density profile $N(R)$ via the Abel integral. The line-of-sight velocity dispersion comes from σ_r and β via:

$$\sigma_{\text{los}}^2(R, r) = [1 - \beta(r)(R/r)^2] \sigma_r^2(r), \quad (18)$$

and σ_r is obtained from $\beta(r)$ and $M(r)$ as a solution of the Jeans Eqn. (15) (van der Marel 1994),

$$\nu \sigma_r^2 = -G \int_r^\infty \nu(\xi) M(\xi)/\xi^2 \exp[2 \int_r^\xi \beta d\eta/\eta] d\xi. \quad (19)$$

The best-fit parameters of the input models for $M(r)$ and $\beta(r)$ are obtained by maximising the product of the $p(v_{\text{los}}|R)$ probabilities. MAMPOSSt has been used to determine several individual or stack cluster mass profiles (Biviano et al. 2013; Munari et al. 2014; Durret et al. 2015; Balestra et al. 2016; Biviano et al. 2016; Verdugo et al. 2016; Biviano et al. 2017b,a). In combination with gravitational lensing (see Sect. 3.3) MAMPOSSt has also been used to constrain the nature of gravity (Pizzuti et al. 2016, 2017) and the equation of state of dark matter (Sartoris et al. 2014).

The Caustic method (Diaferio & Geller 1997; Diaferio 1999; Serra et al. 2011) has been developed to estimate cluster masses beyond the virial region, i.e. outside the domain of validity of the methods described above, that all rely on the assumption of dynamical equilibrium. This method defines the caustic in PPS by identifying steep density gradients in PPS along the velocity axis. N-body simulations show that the caustic amplitude $\mathcal{A}(R)$ can be used to estimate $M(r)$ via

$$G [M(r) - M(r_0)] = \int_{r_0}^r \mathcal{A}^2(x) \mathcal{F}_\beta(x) dx. \quad (20)$$

$\mathcal{F}_\beta(x)$ is a radial varying function of both $\beta(r)$ and the gravitational potential itself. Eqn. 20 can be solved by assuming a constant value for \mathcal{F}_β . This assumption is violated within the virial region, leading to a mass over-estimate (Serra et al. 2011), but it is a valid one outside the virial region, where

numerical simulations indicate $\mathcal{F}_\beta \approx 0.5 - 0.7$ (Gifford et al. 2013, and references therein). Since Eqn. (20) is differential in $M(r)$, one can obtain the mass profile out to a given radius r_0 by another technique, e.g. MAMPOSSt, and then use the Caustic method to determine $M(r > r_0)$ (Biviano & Girardi 2003; Biviano et al. 2013). The Caustic method has been extensively used to determine cluster mass profiles (e.g. Biviano & Girardi 2003; Biviano et al. 2013; Geller et al. 2014; Guennou et al. 2014).

3.1.2 Sources of systematic uncertainty

In Sect 3.1.1 we have already mentioned the systematic uncertainties that are specific to each individual method. Here we discuss how these and other issues propagate into systematic effects in the resulting mass estimate. The typical level of systematic uncertainty in cluster mass estimates inherent in current methods, assuming typical data-sets of ~ 100 cluster members, is summarised below in percentages (a value of 0 means the bias can be fully corrected):

- mass-anisotropy degeneracy 8%
- uncertainty in \mathcal{F}_β 15% (Caustic-method specific)
- dynamical equilibrium 30% (irrelevant for Caustic method)
- interlopers 10%
- spatial incompleteness 0%
- triaxiality 30%

Dynamical equilibrium: Deviation from dynamical equilibrium can result from ongoing major mergers between a cluster and a massive accreting subcluster. Takizawa et al. (2010) find that a cluster-subcluster collision may lead to a factor ~ 2 mass over-estimate from kinematics, for ~ 1 Gyr after each core passage of the subcluster, but only if the collision axis is aligned with the line-of-sight. Most of the effects of the collision are erased after a dynamical timescale. Observationally, deviation from dynamical equilibrium can be identified by the analysis of the shape of the velocity distribution of cluster galaxies (Biviano et al. 2006; Ribeiro et al. 2011; Roberts et al. 2018).

Interlopers: Interlopers can be defined in two ways: (1) galaxies that are located in projection within a given radius from the cluster centre, but are outside the sphere of same radius, or (2) galaxies that are unbound to the cluster. While interloper-removal techniques have become increasingly sophisticated with time (e.g. Yahil & Vidal 1977; Fadda et al. 1996; Wojtak et al. 2007; Mamon et al. 2013), it is impossible to reduce contamination by interlopers to zero and, at the same time, retain all the real members in the sample (Mamon et al. 2010). Comparison to numerical simulations indicate that contamination by interlopers and incompleteness of real

cluster members tend to overestimate cluster masses at the low-mass end and underestimate cluster masses at the high-mass end (Wojtak et al. 2018).

Spatial incompleteness: A particular observational set-up (e.g. caused by fiber collision of slit positioning) can cause a spatially-dependent incompleteness of the spectroscopic sample. If not properly corrected, this incompleteness induces an error in the determination of $v(r)$. On the other hand, the velocity distribution of cluster galaxies is mildly, if at all, affected by spatially-dependent incompleteness. If the incompleteness cannot be corrected it is more robust to base the cluster mass estimate on the velocity distribution only (Biviano et al. 2006), or to use the complete photometric sample with background subtraction, to estimate $v(r)$ (see, e.g. Biviano et al. 2013).

Triaxiality: All clusters are triaxial, and the velocity dispersion tensor is elongated along the same direction as the galaxy spatial distribution. If the cluster major axis is aligned along (perpendicular to) the line-of-sight, the observed velocity dispersion will be higher (lower) than the average of the three components of the velocity dispersion tensor (Wojtak 2013). The cluster projection angle relative to the cluster major axis is generally very difficult to determine (Sereno 2007), so triaxiality becomes an important source of (systematic) error in the cluster mass estimate, up to $\sim 60\%$, but generally much lower than this (Wojtak 2013). Stacking several clusters together is a simple and effective way of getting rid of the triaxiality problem (e.g. van der Marel et al. 2000).

3.2 X-ray and hybrid SZ

Upon reaching equilibrium, the thermodynamical properties of the ICM satisfy the HE relation between the ICM pressure P_{gas} , the ICM density $\rho_{\text{gas}} = \mu m_p n_{\text{gas}}$ and the potential (see Eqn. 8). We discuss in Sect. 2.3 the insights gained from numerical simulations for when the condition of HE is not satisfied, and what this implies for the mass reconstruction. Measurement of cluster masses in X-rays, through the hydrostatic assumption, gained significant traction after the launch of ROSAT in 1990, owing to the easy availability of spatially resolved density profile observations.

3.2.1 Method

Assuming a spherically symmetric distribution, one can write the HE equation:

$$M_{\text{tot}}(< r) = - \frac{r P_{\text{gas}}}{\mu m_u G n_{\text{gas}}} \frac{d \log P_{\text{gas}}}{d \log r}, \quad (21)$$

where G is the gravitational constant, $m_u = 1.66 \times 10^{-24}$ g is the atomic mass unit, and $\mu = \rho_{\text{gas}} / (m_u n_{\text{gas}}) \approx (2X + 0.75Y +$

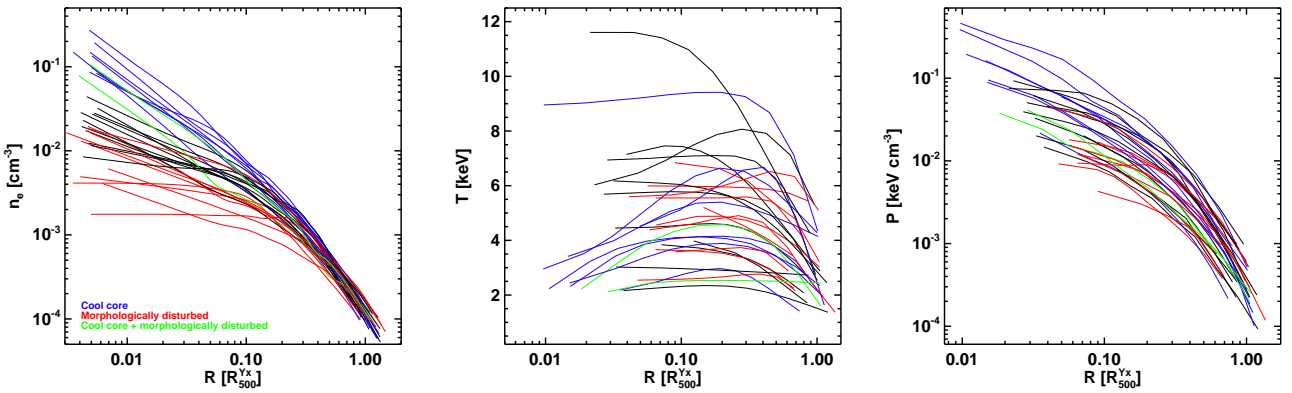


Fig. 5 Left to right: Reconstructed gas density, temperature, and pressure profiles from the REXCESS sample (Pratt et al. 2010; Arnaud et al. 2010), plotted as a function of R_{500} . The profiles are colour-coded as a function of dynamical state as defined in Pratt et al. (2009): cool core (blue), morphologically disturbed (red), cool core and morphologically disturbed (green) and intermediate (black).

$0.56Z)^{-1} \approx 0.6$ is the mean molecular weight in atomic mass unit for an ionized plasma; X , Y and Z being the mass fraction for hydrogen, helium and other elements, respectively. For a typical metallicity of 0.3 times Solar abundance, and assuming the abundance table of Anders & Grevesse (1989), $X + Y + Z = 1$, with $X \approx 0.716$ and $Y \approx 0.278$.

Assuming the ICM follows the equation of state for a perfect gas ($P_{\text{gas}} = kT_{\text{gas}}n_{\text{gas}}$, where k is the Boltzmann constant), the directly-observable physical quantities in X-rays are the radial density n_{gas} and temperature T_{gas} of the plasma (e.g. Fig. 5). The gas density can be obtained from the geometrical deprojection of the X-ray surface brightness, extracted in thin annuli. Corrections for contaminating gas clumps can be obtained by masking substructures (which are spatially resolved with XMM-Newton and Chandra), and by measuring the azimuthal median, instead of the azimuthal mean (Zhuravleva et al. 2013; Morandi et al. 2013; Eckert et al. 2015). The radial gas temperature distribution is built from spectra extracted in annuli that are wider than those used for the surface brightness, and can be modelled with an absorbed thermal component.

A relatively recent development is the availability of spatially-resolved SZ electron pressure profiles, P_{gas} , which can be obtained from geometric deprojection of the azimuthally-averaged integrated Comptonization parameter y (e.g. Mroczkowski et al. 2009; Planck Collaboration Int. V 2013; Sayers et al. 2016; Romero et al. 2017; Ruppin et al. 2018). Joint deprojection of SZ and X-ray images can be applied to avoid the use of X-ray spectroscopic data (e.g. LaRoque et al. 2006; Ameglio et al. 2007; Adam et al. 2016; Ruppin et al. 2017; Shitanishi et al. 2018; Ghirardini et al. 2019), and also for total mass estimates (e.g. Ameglio et al. 2009; Adam et al. 2016; Ruppin et al. 2017, 2018).

The two main approaches adopted to solve Eqn. 21 are known as the *backward* and *forward* methods. In the *backward* method, a parametric mass model is assumed and com-

bined with the gas density profile to predict a gas temperature profile T , which is then compared to the measured T_m in the spectral analysis. In the *forward* method, functional forms are fitted to the deprojected gas density or surface brightness profiles, and to the temperature (e.g. Pratt & Arnaud 2002; Vikhlinin et al. 2006a; Pointecouteau et al. 2005) or pressure profiles (e.g. Pratt et al. 2016; Ghirardini et al. 2018; Ettori et al. 2019), with no assumptions on the form of the gravitational potential. In all cases, the procedure takes into account projection and PSF effects (the latter can be neglected for Chandra data). The HE equation (Eqn. 21) is then applied to evaluate the radial distribution of the mass. More details on the traditional methods applied to X-ray data to estimate the mass profile can be found in Ettori et al. (2013a).

The forward method has several variants, as described by Bartalucci et al. (2018). The fully parametric method (e.g. Vikhlinin et al. 2006a) directly uses the best-fitting analytic density and temperature or pressure models. Another approach, the non-parametric like method (e.g. Pratt et al. 2016), uses parametric models only to correct the observed temperature profiles for projection and PSF effects, and to smooth the density gradients.

The various methods have been compared by Bartalucci et al. (2017) and Bartalucci et al. (2018). They showed that the density profile is exceptionally robust to both the method used for its reconstruction and to instrumental systematic effects. They found that mass profile estimates are also insensitive to the reconstruction method in the radial range of the measured temperature profile. On the other hand, the mass uncertainty does depend on the method, with fully parametric methods yielding the smallest uncertainties. The mass estimate also depends on the method when extrapolation is required, especially in the case of irregular profiles (see Fig. 6).

If SZ data are available, the likelihood can also include a comparison with $T = P_{\text{SZ}}/n_{\text{gas}}$. This method takes advan-

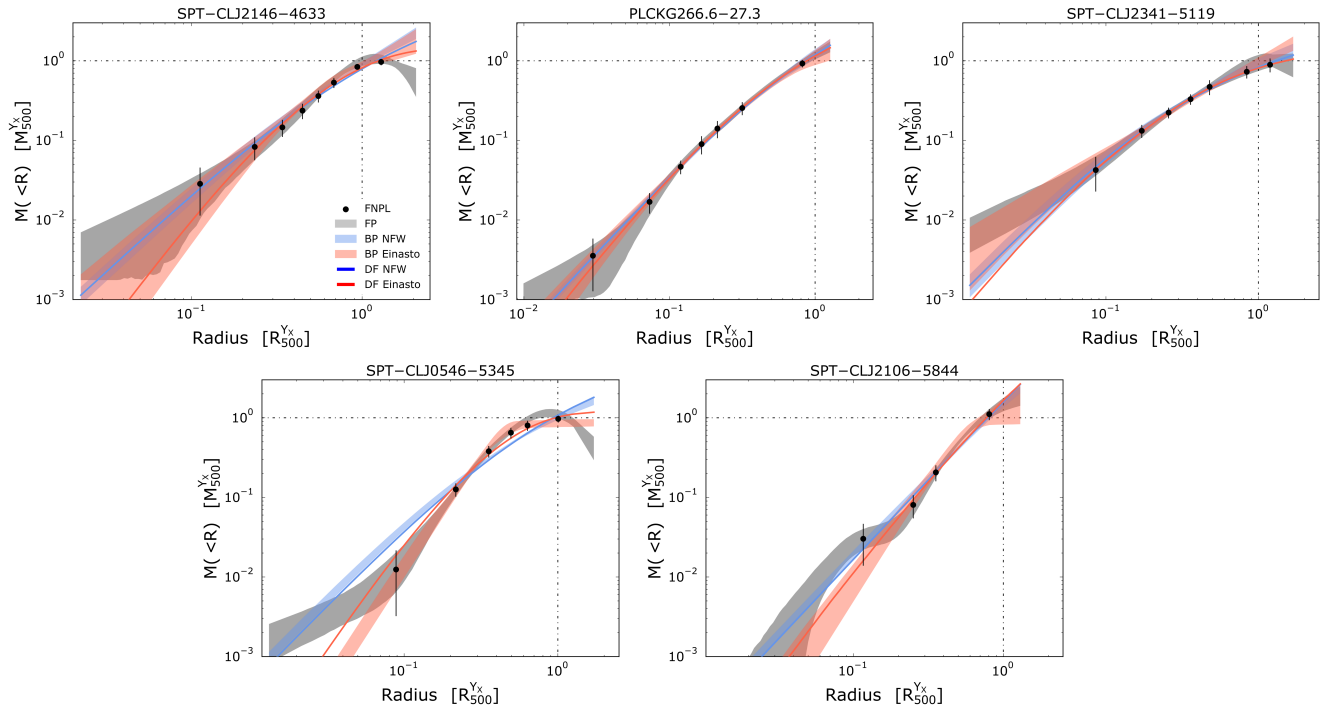


Fig. 6 3D total mass profiles of the clusters in the sample analysed by [Bartalucci et al. \(2018\)](#) at $z \sim 1$, with several mass distribution reconstruction methods overplotted.

tage of the larger extension of the SZ signal in constraining the mass profile model (e.g. [Planck Collaboration Int. V 2013](#); [Ghirardini et al. 2018](#); [Ettori et al. 2019](#)). As combination with SZ data does not need spectroscopic temperature measurements, this method also allows for hydrostatic mass profile estimates out to higher redshift ([Ruppin et al. 2018](#)).

3.2.2 Sources of systematic uncertainty

The hydrostatic mass estimate depends on the direct measurement of the gas density profile from X-ray data, combined with the radial profile of either the X-ray spectroscopic temperature, or the SZ-derived pressure of the ICM. Any bias on these measurements propagates into systematic effects on the resulting mass estimate, which can be roughly summarised in percentages as follows:

- assumption of spherical symmetry few %
- hydrostatic mass bias < 10 - 30%
- gas temperature inhomogeneities few - 10-15%
- gas clumping few %
- absolute X-ray temperature calibration 15-20%

Spherical assumption: The biases induced by the assumption of spherical symmetry were investigated by [Buote & Humphrey \(2012\)](#), who found that while the mean bias is small ($\lesssim 1\%$), substantial variations can occur on a cluster to cluster basis, depending on the exact viewing orientation.

Hydrostatic mass bias: The fundamental assumption of the X-ray and SZ analyses described above is that the gas is in HE in the dark matter potential. As discussed in Sect. 2.3, numerical simulations are unanimous in predicting that such an assumption is likely to lead to an underestimate of the mass due to neglect of bulk motions and turbulence in the ICM. The effect will naturally be most important in dynamically disturbed systems (up to $\sim 30\%$), and least important in relaxed objects ($\lesssim 10\%$). The actual magnitude of this so-called ‘hydrostatic bias’ is difficult to ascertain both numerically (see Sect. 2.4) and observationally, although great progress has recently been made in this area and is discussed below in Sect. 4.

Gas temperature inhomogeneities: An issue that can potentially affect the X-ray analysis is the presence of temperature inhomogeneities in the gas (Sect. 2.4). If a significant amount of cool gas is present, then a single temperature fit will be biased towards lower temperatures, which will in turn have an impact on the mass estimate. Usually, X-ray spectra are accumulated within annular regions and their spectral shape is fitted assuming that the gas temperature within the considered shell is uniform. Essentially all X-ray instruments used thus far for estimating ICM temperatures possess an effective area that peaks around 1 keV and declines steeply above ~ 5 keV. This renders current X-ray telescopes intrinsically more sensitive to the gas in the temperature range $\approx 1-3$ keV ([Mazzotta et al. 2004](#); [Vikhlinin 2006](#)). If the gas distri-

bution within a given shell is multiphase, the X-ray spectra fitted assuming that the plasma is single-phase should in principle underestimate the mean gas-mass-weighted temperature. This effect can be enhanced in cases where the cooler gas phase coincides with infalling substructures, which feature an increased gas density with respect to their environment and thus contribute strongly to the total X-ray flux. The percentages listed above come from numerical simulations (Rasia et al. 2014), but estimates of the effect vary widely owing to differences in numerical schemes and input physics. For example, simulations with heat conduction always predict more homogeneous temperature distributions, minimising any bias, while simulations lacking non-gravitational input from supernovae and AGN predict long-lasting, dense cool cores that will strongly contribute to any bias. While most observational studies attempt to make allowances for temperature inhomogeneities by masking detected structures and taking the line-of-sight gradient into account with a spectral-like temperature weighting while deprojecting, there may remain an additional source of temperature inhomogeneities which current studies cannot pinpoint.

Gas clumping: A further issue is gas clumping, i.e. deviations from an isotropic distributions induced by substructures, which can potentially bias measurements of the gas density, and thus the mass, when the X-ray signal is azimuthally averaged over concentric annuli. Current limits from X-ray observations (Eckert et al. 2015; Morandi & Cui 2013; Urban et al. 2014; Tchernin et al. 2016) agree with the predictions from numerical simulations (e.g. Roncarelli et al. 2013). Observational constraints on gas clumping are described in detail in the chapter of this series related to galaxy cluster outskirts (Walker et al. 2019).

Absolute X-ray calibration: A final issue is the absolute calibration of X-ray instrumentation. In recent years, it has become apparent that ICM temperatures estimated with different X-ray instruments (in particular XMM-Newton and *Chandra*) show a systematic offset (Nevalainen et al. 2010; Mahdavi et al. 2013; Martino et al. 2014; Donahue et al. 2014; Schellenberger et al. 2015). The observed differences result from the calibration of the effective area of the two telescopes, which is inconsistent at the 5-10% level. In Fig. 7, taken from Schellenberger et al. (2015), we show a comparison between spectroscopic temperatures measured with XMM-Newton and *Chandra* for the same regions. While for temperatures below 5 keV the offset between the two is small, at high temperatures the measured temperatures differ by 15-20%. Hydrostatic masses estimated with X-ray data only are principally proportional to the gas temperature. The corresponding uncertainty propagates linearly to the hydrostatic mass in the first approximation (for a mass at a fixed overdensity, the scaling is roughly $\propto M \sim T^{1.5}$). However the

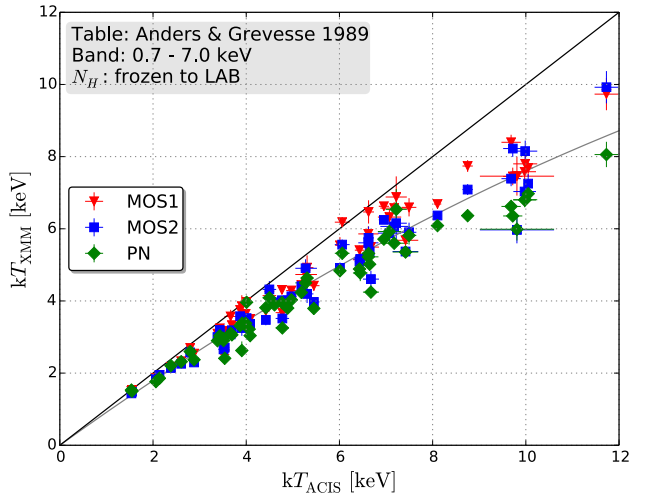


Fig. 7 ICM gas temperatures measured with the three XMM-Newton instruments (MOS1, MOS2, and PN) plotted against temperatures measured with *Chandra*/ACIS for the same regions. The black line is the one-to-one relation. Reproduced from Schellenberger et al. (2015).

hydrostatic mass also depends on the temperature gradient. In this context, we note that Martino et al. (2014) actually found a very good agreement (within 2%) between hydrostatic masses estimated from *Chandra* and XMM-Newton.

One possible way of investigating the issue is to compare in a systematic way the spectroscopic X-ray temperatures with the temperatures estimated by combining the gas density with the pressure measured through the SZ effect, $\eta_T = T_{\text{X}} n_{\text{X}} / P_{\text{SZ}}$. Bourdin et al. (2017) measured $\eta_T = 1.02^{+0.02}_{-0.03}$ with a low-redshift XMM-Newton sample. A very similar value, $\eta_T = 1.04 \pm 0.08$, was reported for the XCOP sample (Ghirardini et al. 2019). Adam et al. (2017) performed a detailed comparison of temperatures in the hot cluster MACS J0717.5+3745 between XMM-Newton, *Chandra* and NIKA, and found that the joint X/SZ temperatures lie somewhat in between, $\eta_T \sim 0.9$ and $\eta_T \sim 1.1$ for XMM-Newton and *Chandra*, respectively. The statistical quality of such comparisons is expected to increase substantially in the near future given the growing number of systems with available deep SZ data.

3.3 Weak lensing analysis

The deep potential well of a galaxy cluster weakly and coherently distorts the shapes of background galaxies through the differential deflection of light rays. A statistical treatment of the coherent distortion pattern allows us to measure cluster masses without assumptions about their physical nature or dynamical state. This is the well-known weak gravitational lensing (WL hereafter) effect, which has recently become extremely competitive as a means to estimate cluster masses. In

general, wide-field cameras installed on large ground-based telescopes are the best instruments for weak-lensing analysis; e.g. Suprime-cam and Hyper Suprime-Cam (HSC) on the Subaru telescope, and MegaCam of the Canada-France-Hawaii Telescope, and Dark Energy Camera (DECam) of the Victor M. Blanco 4-meter Telescope. Specifically, large mirrors can observe galaxies up to $z \sim 1$ in short observing times, and the wide field-of-view cameras cover out to the virial radius with superb image quality. The advent of the prime-focus cameras installed on large mirror telescope has made a tremendous progress of weak-lensing analysis for the last decade.

3.3.1 Method

Images of background source galaxies are distorted by the tidal gravitational field. Image distortion of background source galaxies is expressed by the complex shear, $\gamma \equiv \gamma_1 + i\gamma_2$. The complex shear is related to the convergence κ , through

$$\gamma(\theta) = \frac{1}{\pi} \int d^2\theta' D(\theta - \theta') \kappa(\theta') \quad (22)$$

with

$$D(\theta) = \frac{\theta_2^2 - \theta_1^2 - 2i\theta_1\theta_2}{|\theta|^4}, \quad (23)$$

where θ is an apparent angular position. Here, the convergence κ is the dimensionless projected mass density, given as

$$\kappa(\theta) = \frac{\Sigma(\theta)}{\Sigma_{\text{cr}}(z_l, z_s)}, \quad (24)$$

with the dimensional projected mass density Σ and the critical surface mass density

$$\Sigma_{\text{cr}}(z_l, z_s) = \frac{c^2}{4\pi G} \frac{D_s}{D_l D_{ls}}. \quad (25)$$

Here D_l is the angular diameter distance to the lens, and D_s and D_{ls} are the angular diameter distances from the observer to the sources and from the lens to the sources, respectively.

The complex ellipticity of individual galaxies is defined as (Bartelmann & Schneider 2001),

$$\varepsilon = \frac{Q_{11} - Q_{22} + 2iQ_{12}}{Q_{11} + Q_{22} + 2(Q_{11}Q_{22} - Q_{12}^2)^{1/2}} \quad (26)$$

(e.g. Kaiser et al. 1995; Okabe & Umetsu 2008; Kitching et al. 2008; Oguri et al. 2012; Heymans et al. 2012; Miller et al. 2013; Applegate et al. 2014; Umetsu et al. 2014; Hoekstra et al. 2015b; Okabe & Smith 2016; Jarvis et al. 2016; Okura & Futamase 2018) or

$$\chi = \frac{Q_{11} - Q_{22} + 2iQ_{12}}{Q_{11} + Q_{22}} \quad (27)$$

(e.g. Bernstein & Jarvis 2002; Hirata & Seljak 2003; Mandelbaum et al. 2018), where Q_{ij} is the quadrupole moment of the surface brightness. The observed ellipticities, ε, χ are

distorted by the gravitational lensing effect, and expressed in the weak-limit ($\kappa \ll 1$ and $\gamma \ll 1$), as follows, $\varepsilon \rightarrow \varepsilon_s + g$ and $\chi \rightarrow \chi_s + 2g$, where the subscript s denotes the intrinsic (unlensed) ellipticity and g is the reduced shear

$$g = \frac{\gamma}{1 - \kappa}. \quad (28)$$

Since the gravitational lensing signals in the central regions of galaxy clusters are somewhat strong, one in general uses the reduced shear, g , rather than the shear γ for cluster mass measurements. Assuming that orientations of intrinsic ellipticity are random ($\langle \varepsilon_s \rangle = 0$ and $\langle \chi_s \rangle = 0$), the gravitational lensing signal can be measured by an ensemble average of background galaxies, $\langle g \rangle \simeq \langle \gamma \rangle \simeq \langle \varepsilon \rangle \simeq \langle \chi \rangle / 2$. The statistical uncertainty of the shear component, $\sigma_g \simeq (\langle \varepsilon_s^2 \rangle / N)^{1/2}$, decreases with increasing the number of background galaxies, N . Therefore, weak-lensing analysis requires a large number of background galaxies.

Weak-lensing observables do not provide direct estimates of three-dimensional masses of clusters because the lensing signal probes the two-dimensional projected mass distribution. One therefore estimates M_A by fitting a three-dimensional model to the data. For this purpose, a tangential distortion profile as a function of cluster-centric radius is widely used in weak-lensing mass measurements. This quantity is computed in a given annulus by azimuthally averaging the measured galaxy ellipticities. In recent studies, the expression of a dimensional component, $\Delta\Sigma_+$, is being widely used rather than a dimensionless expression, g_+ , thanks to recent updates of photometric redshifts. The tangential components of reduced shear in the i -th radial bin are estimated as

$$\langle \Delta\Sigma_+ \rangle(R_i) = \frac{\sum_n \Sigma_{\text{cr},n} \varepsilon_{+,n} w_n}{\sum_n w_n}, \quad (29)$$

where the subscript n denotes the n -th galaxy located in the annulus spanning $R_1 < R_i < R_2$ and $w_n \propto \Sigma_{\text{cr},n}^{-2}$ is the weighting function considering the intrinsic ellipticity and shape measurement errors. We here use the notations of projected radii R and three-dimensional radii r . When Σ_{cr} is computed by integrating the full probability function, $P(z)$, $\Sigma_{\text{cr}} \equiv \langle \Sigma_{\text{cr}}^{-1} \rangle^{-1}$ where the bracket denotes the average over redshifts. The projected distance from a given cluster centre, R_i , is defined by the weighted harmonic mean radius of sparsely distributed galaxies

$$R_i = \frac{\sum_n w_n}{\sum_n w_n R_n^{-1}}, \quad (30)$$

(Okabe & Smith 2016). When one corrects the measured values using the multiplicative calibration bias m for individual galaxies (Heymans et al. 2006; Massey et al. 2007), the measured ensemble shear becomes $\Delta\Sigma_{+,i} \rightarrow \Delta\Sigma_{+,i} / (1 + K_i)$, where the correction factor, K , is described by

$$K_i = \frac{\sum_n m_n w_n}{\sum_n w_n}. \quad (31)$$

When one computes the tangential shear profile in comoving coordinates, all the equations are computed with the conversion factors of $\Sigma_{\text{cr}}^{\text{c}} \equiv \Sigma_{\text{cr}}(1 + z_i)^{-2}$ and $R^{\text{c}} \equiv (1 + z_i)R$.

Given the tangential shear profile, the log-likelihood is expressed by

$$-2 \ln \mathcal{L} = \ln(\det(C_{ij})) + \sum_{i,j} (\Delta\Sigma_{+,i} - f_{\text{model}}(R_i)) C_{ij}^{-1} (\Delta\Sigma_{+,j} - f_{\text{model}}(R_j)), \quad (32)$$

where the subscripts i and j are the i - and j -th radial bins. Here, f_{model} is the reduced shear prediction for a specific mass model. The covariance matrix, C , in Eqn. 33 is given by:

$$C = C_g + C_s + C_{\text{LSS}} + C_{\text{int}}, \quad (33)$$

(e.g. Gruen et al. 2015; Umetsu et al. 2016; Miyatake et al. 2018). Here C_g , C_s , and C_{LSS} are the shape noise, the photometric redshift error, and the covariance matrix of uncorrelated large-scale structure (LSS) along the line-of-sight (Schneider et al. 1998), respectively. The covariance matrix of uncorrelated large-scale structure (LSS), C_{LSS} , along the line-of-sight (Schneider et al. 1998) is given by

$$C_{\text{LSS},ij} = \Sigma_{\text{cr}}^2(z_i, \langle z_s \rangle) \int \frac{l dl}{2\pi} C^{\kappa\kappa}(l) J_2(lR_i/D_l) J_2(lR_j/D_l), \quad (34)$$

where $J_2(l\theta_i)$ is the first kind and second order Bessel function (Hoekstra 2003) and $C^{\kappa\kappa}(l)$ is the weak-lensing power spectrum, obtained by

$$C^{\kappa\kappa} = \frac{9H_0^2 Q_m^2}{4c^4} \int_0^{\chi_s} d\chi \left(\frac{\chi_s - \chi}{\chi_s a(\chi)} \right)^2 P_{\text{nl}}(l/\chi; z), \quad (35)$$

(e.g. Schneider et al. 1998; Hoekstra 2003). Here, χ_s is the comoving distance for the source at the average source redshift, $\langle z_s \rangle$. The latter is calculated by \mathcal{L} (Eqn. 37) averaged over the radial range of the tangential shear profile. P_{nl} is the non-linear matter power spectrum (e.g. Smith et al. 2003; Eisenstein & Hu 1998). C_{int} accounts for the intrinsic variations of projected cluster mass profiles such as halo triaxiality and the presence of correlated haloes (Gruen et al. 2015). The intrinsic covariance becomes a significant component of the uncertainty budget of WL mass measurements as the mass increases and the data quality improves. Since this component strongly depends on the prior and realisations, one should carefully consider applications and limitations to the data. In general, each paper clearly specifies which components in the covariance matrix are considered, and thus it is important to undertake a careful reading to understand each analysis.

The model for the dimensional reduced tangential shear, f_{model} , is expressed by

$$f_{\text{model}}(R_i) = \frac{\bar{\Sigma}_{\text{model}}(< R_i) - \Sigma_{\text{model}}(R_i)}{1 - \mathcal{L}_i \Sigma_{\text{model}}(R_i)}, \quad (36)$$

with

$$\mathcal{L} = \frac{\sum_n \Sigma_{\text{cr},n}^{-1} w_n}{\sum_n w_n}. \quad (37)$$

Here, $\bar{\Sigma}$ and Σ are the averaged surface mass density within the radius and the local surface mass density at the radius, respectively. The average source redshift, $\langle z_s \rangle$, is calculated by \mathcal{L} . The denominator describes the non-linear correction in terms of the reduced tangential shear, and can be also rewritten by $(1 - \mathcal{L}\Sigma_{\text{model}})^{-1} \simeq 1 + \mathcal{L}\Sigma_{\text{model}}$.

3.3.2 Sources of systematic uncertainty

A weak-lensing analysis is generally composed of four steps: shape measurement, estimation of photometric redshifts, selection of background galaxies, and mass modelling. Systematic errors inherent in the steps can be roughly summarised in percentage terms as follows:

- accuracy of shape measurements \sim a few - 10 %
- accuracy of photometric redshifts \lesssim sub - a few %
- background galaxies in shape catalogues \lesssim 40 %
- mass modelling \sim 10 %.

The first three systematic errors depend on the technical details adopted in each paper and/or the data quality. The last is related to both assumed mass models and intrinsic cluster physics, such as the distribution of internal structures, halo triaxiality, outer slope of dark matter halo and surrounding environments. A key effort of recent studies of cluster weak-lensing analysis is how to control these systematic issues.

Shape measurements: Shape measurement methods can be categorised into several types: moment measurements in real space or Fourier space, model fitting through maximum likelihood method or Bayesian approach, and machine learning (e.g. Kaiser et al. 1995; Mandelbaum et al. 2015). The anisotropic PSF ellipticities can be decomposed into three components: optical aberration, atmospheric turbulence and chip-misalignment (Hamana et al. 2013), of which the optical aberration is the major contributor. The PSF anisotropy is corrected via the stellar ellipticity ε^* , where an asterisk denotes stellar objects. A good star and galaxy separation is essential in this procedure. Since both galaxies and stars are sparsely distributed over images, a model function of the distortion patterns, such as bi-polynomial functions, is computed by fitting stellar ellipticites. However, the isotropic PSF correction cannot be tested by the imaging data itself, thus mock analysis of simulated images is essential to assess the reliability of shape measurement technique of faint small galaxies (see the details Heymans et al. 2006; Massey et al. 2007; Bridle et al. 2010; Kitching et al. 2012, 2013; Mandelbaum et al. 2015, 2017). The STEP programme (Heymans et al. 2006; Massey et al. 2007) introduces a formula to describe the accuracy of measurement pipelines, defined by

$$g - g_{\text{input}} = m g_{\text{input}} + c \quad (38)$$

where g and g_{input} are the measured and input shear, m is a multiplicative bias and c is a residual additive term. Based

on their pipeline tests, a multiplicative bias can correct the measured shear (Eqn. 31) if necessary. Potential systematic uncertainties can be examined using cross-correlations between maps derived from different quantities (e.g. [Vikram et al. 2015](#); [Oguri et al. 2018](#)): E-mode and B-mode maps with galaxy ellipticities, raw stellar ellipticities, residual stellar ellipticities, and foreground galaxies.

Photometric redshifts: It is important to estimate the redshifts of background galaxies because the lensing efficiency is proportional to $\beta \equiv D_{ls}/D_s$ (Eqns. 24 and 25) at a fixed cluster redshift (z_l). This quantity is significantly affected by changing source redshifts for objects at $z \gtrsim 0.4$. As it is not realistic to obtain spectroscopic redshifts for all background galaxies, photometric redshifts (photo-z) are always used.

Typically, weak-lensing analysis of individual clusters uses two- or three-band imaging due to limitations in observing times. Such a minimum combination of bands cannot in principle be used to estimate photometric redshifts, one instead determines them by matching magnitudes of source galaxies with those in photometric redshift catalogues in the literature (e.g. [Okabe et al. 2010](#); [Oguri et al. 2012](#); [Hoekstra et al. 2012](#); [Applegate et al. 2014](#); [Hoekstra et al. 2015b](#); [Okabe & Smith 2016](#); [Umetsu et al. 2016](#)). To be more precise, the value of β of the i -th background galaxy (β_i) or the average value ($\langle \beta \rangle$) in the target fields is computed by taking into account adequate weights assigned to the background galaxies. The most widely-used external photometric catalogue is from the COSMOS survey ([Ilbert et al. 2013](#)), for which the limiting magnitude $i' \simeq 27.5$ is sufficiently deep for galaxies used in weak-lensing analysis. The COSMOS photometric redshifts based on the thirty bands are well-calibrated by comparing with spectroscopic values. Some papers also compute β_i or $\langle \beta \rangle$ using the full probability function $P(z)$ from the COSMOS photometric catalog. The photometric redshift distribution can also be computed from pointed observations with five- or four-band imaging (e.g. [Applegate et al. 2014](#); [Ziparo et al. 2016](#)), and wide area galaxy surveys, e.g. the Canada France Hawaii Telescope Legacy Survey (CFHTLS; [Ilbert et al. 2006](#)), the Hyper SuprimeCam Survey (HSC-SSP; [Tanaka et al. 2018](#)), the Dark Energy Survey (DES; [Sánchez et al. 2014](#); [Hoyle et al. 2018](#)), and the Kilo-Degree Survey (KiDS; [Bilicki et al. 2017](#)). The advantage of this method is that the photo-z are estimated using the same data as those used for the shape measurements.

An accurate characterisation of the true underlying redshift distribution of galaxies is one of the major challenges. The photo-z estimations are roughly categorised into two types: template-fitting methods (e.g. [Arnouts et al. 1999](#); [Ilbert et al. 2013](#)), and machine-learning methods (e.g. [Colclister & Lahav 2004](#); [Carrasco Kind & Brunner 2014](#)). Both template-fitting and machine learning methods are complementary and necessary to each other (e.g. [Salvato et al. 2018](#)).

To test the performance of photo-z estimations, one can apply a few standard quantities such as bias (a systematic offset between photo and spectro-z), scatter, and outlier fraction. Given five broad-band filters, a sub-percent level bias between photo- and spectro-z is typically achieved (e.g. [Ilbert et al. 2006](#); [Tanaka et al. 2018](#); [Sánchez et al. 2014](#); [Hoyle et al. 2018](#); [Bilicki et al. 2017](#)), with a scatter of a few percent after $N \sigma$ clipping. Since weak-lensing analysis of galaxy clusters uses a large number of galaxies at $z \sim 1$, the statistical uncertainty of average photometric redshift would be reduced by $\sim N^{-1/2}$ where $N \gtrsim O(10^4)$ is the number of the background galaxies. Therefore, the statistical uncertainty of cluster masses caused by photo-z estimations is typically in the order of sub percent. Such a photo-z uncertainty effect on cluster mass measurements can be considered in the error covariance matrix (Eqn. 33).

Background Galaxy Selection and dilution effects: Contamination of background catalogues by unlensed galaxies leads to an underestimate of the weak-lensing signal, and thus it is of critical importance to obtain a secure background catalogue. The main source of contaminated unlensed galaxies are faint galaxies belonging to the cluster, rather than foreground objects ([Broadhurst et al. 2005](#)). The number density of cluster galaxies increases with decreasing projected cluster-centric radius. The ratio of cluster galaxies to background galaxies, f_{mem} , increases with decreasing projected cluster-centric radius, and thereby dilutes the shear signal more at smaller radii than at larger radii, resulting in a significant underestimate in the concentration parameter of the universal mass density profile. This is often referred to as a dilution effect (e.g. [Broadhurst et al. 2005](#); [Umetsu et al. 2010, 2014, 2015](#); [Okabe et al. 2010, 2013](#); [Okabe & Smith 2016](#); [Medezinski et al. 2010, 2017](#)). The number of cluster members increases as cluster richness increases, while the ratio of cluster member galaxies to background galaxies decreases as cluster redshift decreases ([Okabe et al. 2016](#)). Therefore, the dilution effect is a redshift-, richness-, and radially-dependent phenomenon. [Okabe & Smith \(2016\)](#) have shown that dilution of lensing signals for massive clusters at $z \sim 0.2$ can reach up to $\sim 40\%$ at small radii, which is significantly larger than the systematic errors of shape measurements and photometric redshifts. Therefore, background selections are the dominant source of systematic bias in weak-lensing measurements of galaxy clusters.

Corrections for dilution can take the form of the co-called ‘boost factor correction’, which attempts to correct lensing signals for a number density excess, $(1 + n_{\text{non-bkg}}/n_{\text{bkg}})$, under the assumption of a radially uniform distribution of background galaxies (e.g. [Applegate et al. 2014](#); [Hoekstra et al. 2015b](#); [Melchior et al. 2017](#)). However, the assumption of a flat observed number density profile of background galaxies ignores magnification bias (e.g. [Broadhurst et al. 1995](#);

(Umetsu et al. 2014) – i.e. the depletion of the number density of background galaxies at small radii due to lensing magnification. In addition, as the boost factor correction and the concentration parameter are highly degenerate at small radii, this approach cannot constrain the overall mass profiles of galaxy clusters.

Another approach is to obtain a pure background source catalogue using colour information (e.g. Okabe & Umetsu 2008; Umetsu et al. 2014, 2015; Okabe et al. 2010, 2013; Okabe & Smith 2016; Medezinski et al. 2010, 2018) or photometric redshifts (Applegate et al. 2014; Medezinski et al. 2018). The basic idea is to select a colour space region in which the contribution from cluster member galaxies is negligible by monitoring the consistency of the information from colour, lensing signal, and the external photometric redshift catalogue. The advantages of this technique are the consistency assessment between different datasets of galaxy colour, lensing information and photometric redshifts; the quantitative control of the purity of background galaxies; and no assumption of specific cluster mass models or a radial distribution for the background galaxies. Okabe et al. (2016) have shown that lensing signals corrected by the boost factor, with the assumption of the uniform background distribution, are significantly underestimated compared to those derived from the pure background catalogue. A final method is to use photometric redshifts directly computed by the same dataset, simply selecting with the criteria $z_s > z_{\min}$. Here z_{\min} is the minimum redshift defined by authors. With the full probability function, $P(z)$, background galaxies can be also defined as

$$p_0 < \int_{z_{\min}}^{\infty} P(z) dz, \quad (39)$$

where $<$ means that the probability beyond z_{\min} is higher than the requirement for background selection, p_0 (e.g. Heymans et al. 2012; Applegate et al. 2014; Medezinski et al. 2018).

Mass modelling of the tangential shear profile: Given mass models, such as NFW (Eqn. 2) and Einasto (Eqn. 4) one can analytically or numerically compute the local $\Sigma(R)$ and averaged surface mass density within a radius $\bar{\Sigma}(< R)$ by integration of the three-dimensional mass density along the line-of-sight. The NFW form has an analytic expression for Σ and $\bar{\Sigma}$ (Bartelmann 1996), while the other models mentioned above require numerical integrations. In addition to the cluster halo model, the projected mass density of the outer density profiles (i.e. a two-halo term) can also be considered when tangential shear profiles extend far into the outskirts of galaxy clusters (Oguri & Takada 2011; Oguri & Hamana 2011). Such a two-halo term is sometimes shown in stacked lensing profiles.

The haloes of real clusters are not perfectly spherical, but have many subhaloes and a triaxial structure. Lensing-projection bias caused by such intrinsic properties induces

bias and scatter into weak-lensing mass measurements. For instance, if the major axis of a triaxial halo is aligned along the line-of-sight, this leads to an overestimate of the halo concentration (Oguri & Keeton 2004). The presence of massive subhaloes enhances the local surface mass density and consequently underestimates the tangential shear (Okabe et al. 2014). Since both the angular resolution and the signal-to-noise ratio of a tangential shear profile of an individual cluster are relatively low, it is very difficult to uncover all the internal properties through lensing information alone.

Becker & Kravtsov (2011) have estimated weak-lensing masses using the tangential shear profile of simulated haloes considering the shape noise only, and found that the bias and scatter in M_{500} for massive clusters are $\sim -5\%$ and $\sim 30\%$, respectively. Oguri & Hamana (2011) have shown using numerical simulations that weak-lensing masses, M_{vir} are underestimated by up to 5 – 10% and a choice of the outer boundary for fitting affects mass estimates. Meneghetti et al. (2010) have compared weak-lensing masses at three overdensities of $\Delta = 2500, 500$ and 200 with input true mass from numerical simulations, and found that the mean masses agree with the input value but there is 16% scatter in realisations. Okabe & Smith (2016) have shown, based on a method to adaptively choose the radial ranges for fitting, that the geometric mean of WL masses agrees with the input masses for massive clusters with $\sim 5\%$ scatter. Since the assumed set-up parameters for observing conditions, such as cluster mass ranges and redshifts, the number density of background galaxies, and the fitting method, are all different in the literature, it is difficult to quantitatively compare results.

4 Recent advances

In this Section, we discuss recent advances in lensing and X-ray methods in addressing the various outstanding questions and problems outlined above. We also discuss recent mass measurement comparisons between methods.

4.1 Lensing

4.1.1 Results from new samples

In lensing, possibly the most significant recent advance is the ready availability of mass measurements and profile shape parameters for moderately-large samples (many 10s) of objects. In this context, weak-lensing mass measurements for individual clusters have been carried out by several projects, e.g. the Local Cluster Substructure Survey (LoCuSS; Okabe et al. 2010, 2013; Okabe & Smith 2016), the Canadian Cluster Comparison Project (CCCP; Hoekstra et al. 2012, 2015b), the Cluster Lensing And Supernova survey with

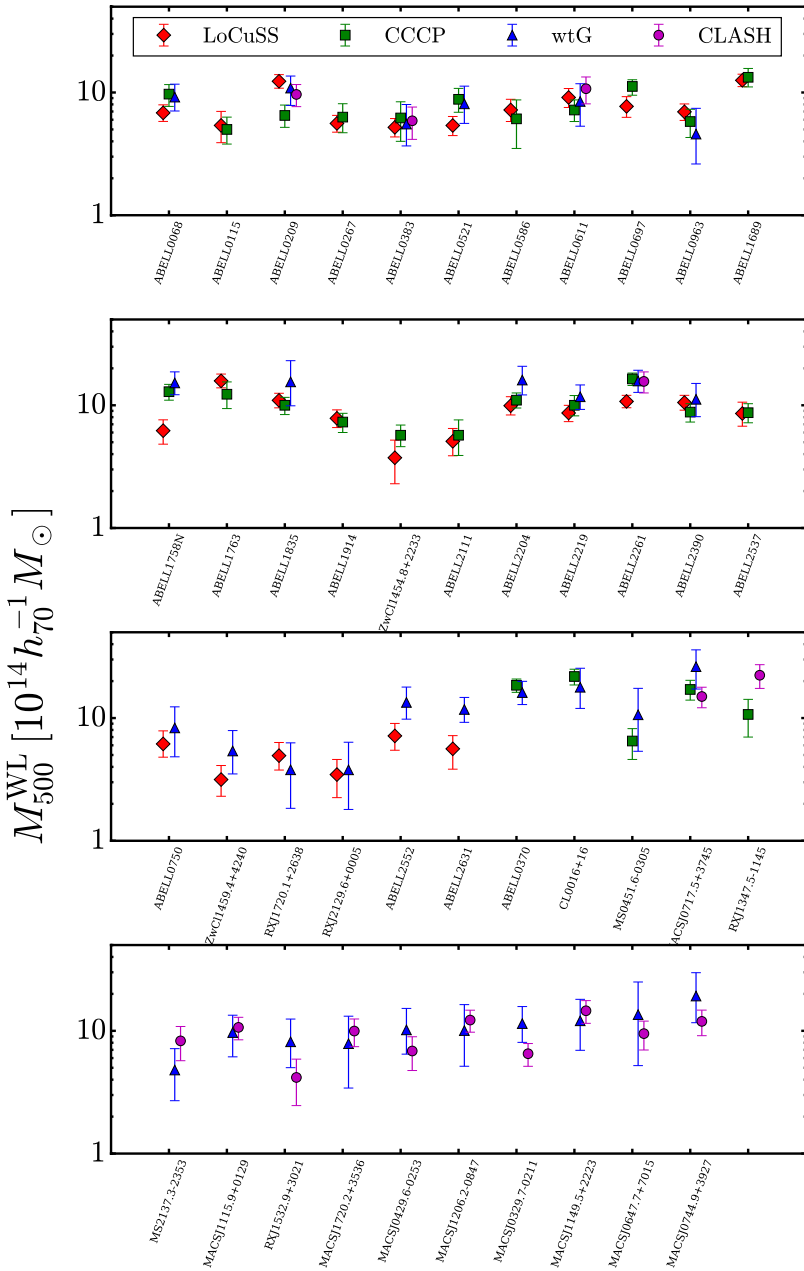


Fig. 8 Weak lensing total mass comparisons at $\Delta = 500$ for LoCuSS (Okabe & Smith 2016), CCCP (Hoekstra et al. 2015b), WtG (Applegate et al. 2014), and CLASH (Umetsu et al. 2016).

Hubble (CLASH; Merten et al. 2014; Umetsu et al. 2014, 2016), and Weighing the Giants (von der Linden et al. 2014; Kelly et al. 2014; Applegate et al. 2014, WtG). The LoCuSS project presented Subaru weak-lensing mass measurements of 50 clusters, selected in X-ray luminosity from the RASS, in the redshift range of $0.15 - 0.3$. The CCCP project complied CFHT data of 50 clusters at redshifts $0.15 < z < 0.55$; 30 out of 50 clusters were selected to have ASCA X-ray temperatures of $kT > 5$ keV. CLASH presented results for a sample of 16 X-ray-regular and 4 high magnification galaxy

clusters at $0.19 < z < 0.69$, combined with Subaru and *HST* data. WtG carried out Subaru weak-lensing analysis for 51 of the most X-ray luminous galaxy clusters at $0.15 < z < 0.7$.

The weak-lensing analysis philosophies for the four projects demonstrate some strong differences, as summarised in Table 1. The LoCuSS project (Okabe & Smith 2016) made a pure background catalogue by checking the consistency between colour, lensing strength and photo- z in the colour-magnitude plane. They treated mass and concentration as free parameters and carried out tangential shear fitting with

various combinations of radial ranges and number of bins, to choose a set close to the average mass and concentration, because sparse distributions of background galaxies and intrinsic cluster properties such as substructures might affect mass estimations. The CCCP project (Hoekstra et al. 2015b) selected background galaxies in colour-magnitude planes, adopted a boost factor correction, and restricted the fit to $0.5 - 2h_70^{-1}$ Mpc to minimise lensing bias (Becker & Kravtsov 2011). They assumed the mass-concentration relation of Dutton & Macciò (2014) because of the radial range of the fit. The uncertainty in the determination of photometric redshifts is the largest source of systematic error for their mass estimates. The CLASH project (Umetsu et al. 2016) selected background galaxies in the colour-colour plane and combined information on the tangential shear profile, the magnification bias, and the projected mass estimated by *HST* strong lensing for the mass measurements. They did not employ a boost factor to compensate for contamination of their background galaxy catalogues. The halo concentration for the NFW model was treated as a free parameter. Their covariance error matrix is composed of the shape noise, photo- z error, uncorrelated LSS lensing, and the intrinsic scatter. The WtG (Applegate et al. 2014) selected background galaxies in the colour-magnitude plane and corrected tangential shear profiles ($0.75 - 3h_70^{-1}$ Mpc) with a boost factor profile using priors from the X-ray gas distribution of Mantz et al. (2010c). They assumed a concentration parameter of $c_{200} = 4$. The uncertainty of mean source redshifts is negligible in their analysis. They also selected background galaxies using the full probability function of the photometric redshifts for a subsample of clusters with five-band imaging.

Comparison of the cluster mass measurements between these different surveys is of paramount importance for cluster cosmology experiments. Mass comparisons can be expressed in terms of the geometric mean $\exp(\langle \ln(Y/X) \rangle)$, or fitting with the lognormal quantities ($\ln X$ and $\ln Y$), because the two quantities are interchangeable. Hoekstra et al. (2015b), Umetsu et al. (2016), and Okabe & Smith (2016) found that the latest weak-lensing masses of CCCP, CLASH and LoCuSS are in excellent agreement, within $\sim 5\%$, and that the WtG masses are somewhat larger than the others ($\sim 10-15\%$). A comparison of M_{500} is shown in Figure 8. All the projects use only two- or three-band imaging, nevertheless weak-lensing masses estimated from different methods show good agreement, which is promising for further weak-lensing surveys for galaxy clusters. Okabe & Smith (2016) pointed out that the mass discrepancy between the WtG and the others is caused by a shallow number density profile for the boost factor. They found a number density excess in the boost-factor profile even outside R_{200} , which may incorrectly enhance lensing signals and overestimate cluster masses.

4.1.2 Mass and concentration

NFW models A weak-lensing study is a powerful direct way to constrain the mass and concentration relation, because tangential shear profiles computed from the wide-field data easily cover the entire radial extent of galaxy clusters, in contrast to X-ray observations which typically cover out to $\sim R_{500}$. The purity of background galaxies in shape catalogues is the most important issue for studies of mass-concentration relation. Okabe et al. (2013) have shown that the concentration parameter is significantly underestimated by the inclusion of unlensed cluster member galaxies in a shape catalogue. The contamination from member galaxies should be at the 1% level, otherwise the concentration parameter is underestimated (Okabe et al. 2010). The CLASH project (Umetsu et al. 2014; Merten et al. 2015) have shown through a joint shear and magnification study and a strong- and weak-lensing study that the concentration for 20 X-ray clusters at $z \sim 0.35$ is in a good agreement with a recent prediction (Meneghetti et al. 2014). Okabe & Smith (2016) have found that the mass and concentration relation for 50 X-ray selected clusters at $z \sim 0.23$ is in good agreement with those of three independent numerical simulations (the left panel Figure 9). A fitting formula of the mass and concentration relation should take account of the correlation between the errors on concentration and mass by calculating the error covariance matrix. The intrinsic scatter of halo concentration could be considered if necessary.

Cibirka et al. (2017) have carried out a stacked lensing analysis for 27 richness selected galaxy clusters at $z \sim 0.5$ and found a good agreement with expectations for shape and evolution. Miyazaki et al. (2018a) have discovered 67 galaxy clusters through peak-finding in weak-lensing mass maps reconstructed from the high number density of background galaxies ($n_g \sim 25 [\text{arcmin}^{-2}]$) of the HSC-SSP survey (Aihara et al. 2018a). The clusters in the resulting catalogue are referred to as ‘shear-selected clusters’, and represent one of the first applications to the HSC of this potentially powerful selection method which is complementary to X-ray, SZ and optical selection. They have carried out a stacked lensing analysis and found that the halo concentration for shear-selected clusters agrees well with those for X-ray selected clusters. This indicates that shear-selected clusters are less biased by halo orientation, in contrast to high concentration parameter for strong-lensing clusters (e.g. Broadhurst et al. 2005; Umetsu et al. 2011).

Current observational studies probe the relation between mass and concentration only in narrow redshift ranges. This is purely caused by dataset limitations. On-going and future optical surveys such as the DES (Dark Energy Survey Collaboration et al. 2016a), HSC-SSP (Aihara et al. 2018a) and the Large Synoptic Survey Telescope (LSST; Ivezic et al. 2008) will detect large samples of galaxy clusters in wide mass and

Table 1 Summary of weak-lensing analysis methods of LoCuSS (Okabe & Smith 2016), CCCP (Hoekstra et al. 2015b), CLASH (Umetsu et al. 2016) and WtG (Applegate et al. 2014). Column *Method* denotes either tangential shear fitting (g_+), or joint fitting using tangential shear profiles, strong-lens and the magnification bias (SL, g_+ & μ). Column *Calibration factor* is the shear-calibration factor, with ‘Yes’ indicating that such a factor was applied to the shear signal before fitting mass models, and ‘No’ indicating otherwise. Column *Boost factor* is the correction factor by the number density caused by imperfect background selection – Yes/No indicates whether or not this factor was calculated and applied to the data. Column *Radial bins* gives the choice of radial binning scheme for the fitting of the shear profile. c_A states whether the concentration parameter was a free parameter in the fit, or fixed, or scaling with the mass. Noise denotes treatments of covariance matrix in the fitting (Eqn. 34).

Name	Method	Calibration factor	Boost factor	Radial bins	c_A	Noise
LoCuSS	g_+	No/Yes	No	Adaptive	Free	$C_g + C_s + C_{\text{LSS}}$
CCCP	g_+	Yes	Yes	Fixed	Scaling	$C_g + C_s$
CLASH	SL, g_+ & μ	Yes	No	Fixed	Free	$C_g + C_s + C_{\text{LSS}} + C_{\text{int}}$
WtG	g_+	Yes	Yes	Fixed	Fixed	C_g

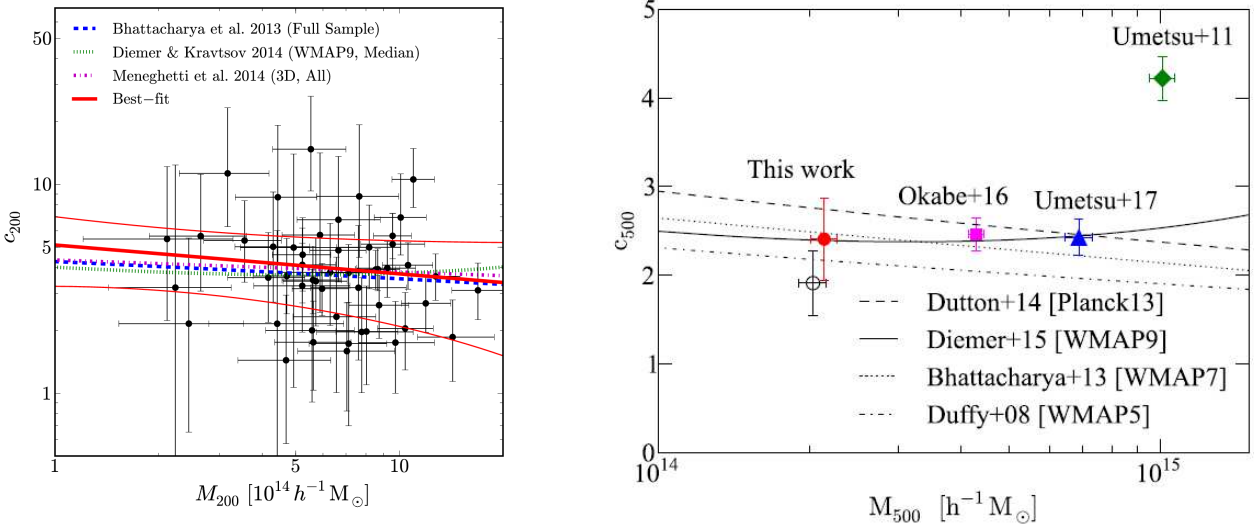


Fig. 9 (Left): The observed distribution of the concentration parameters c_{200} as a function of the cluster masses M_{200} for 50 clusters (Okabe & Smith 2016). The errors denote 68% confidence intervals. The thick and thin lines (red) are the best-fit function and the errors, respectively. The dashed blue, dotted green and dotted-dashed magenta lines are the mean mass-concentration relation from recent numerical simulations of Bhattacharya et al. (2013), Diemer & Kravtsov (2014) and Meneghetti et al. (2014) at $z_l = 0.23$, respectively. (Right): constraints on the mass-concentration relation for shear-selected clusters (Miyazaki et al. 2018a). The open and filled circles denote the halo concentration computed with and without the dilution effect, respectively. The filled triangle shows the results for 16 X-ray-selected clusters at an average redshift of 0.34 obtained from a strong and WL analysis of Umetsu & Diemer (2017). The filled square is from Okabe & Smith (2016), estimated from 50 X-ray luminous (LoCuSS) clusters at redshifts between 0.15 and 0.3, The filled diamond shows the results for a sample of four strong-lensing selected superlens clusters at an average redshift of 0.32 from a strong and WL analysis of Umetsu et al. (2011).

redshift ranges, and will enable us to constrain the redshift evolution of the mass and concentration. Moreover, sample selection biases will be investigated in detail.

Einasto models As a next step for mass modelling, one aims to measure the shape parameter, α , of the Einasto (1965) profile (Eqn. 4) which describes the spherically averaged mass density profile for simulated haloes better than the NFW profile (Navarro et al. 2004). Since it is very difficult to distinguish between the NFW and Einasto profiles with the tangential profiles of individual clusters, one in general adopts the NFW model for individual mass measurements. On the other hand, a stacked lensing profile (e.g. Okabe et al. 2010, 2013; Umetsu et al. 2014, 2016; Umetsu & Diemer

2017; Okabe & Smith 2016; Cibirka et al. 2017; Miyazaki et al. 2018a) is a powerful route to constrain the average mass density profile. First, the average distortion or projected mass profiles are less sensitive to internal substructures and the asphericity of the individual cluster mass distributions and also to uncorrelated large-scale structure along the same line-of-sight. This is because these structures are averaged out via the stacking, under the assumption that the universe is statistically homogeneous and isotropic. Second, stacking procedures improve the signal-to-noise ratio of lensing profiles. Since the lensing signals at larger radii could be detected, one usually adopts a main halo and the two halo term.

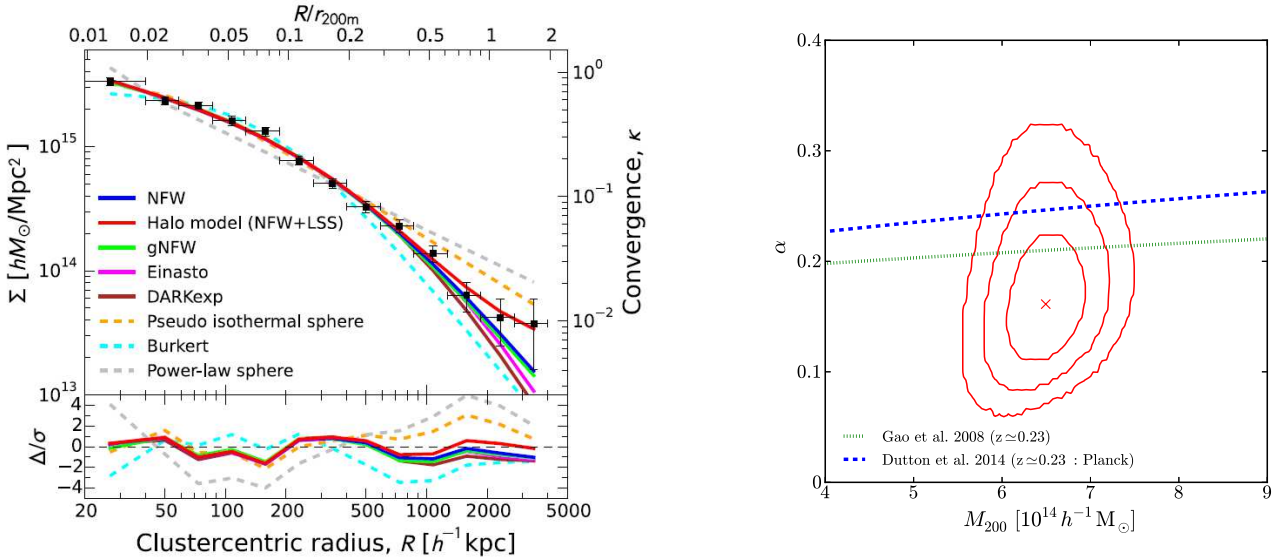


Fig. 10 *Left:* Comparison of models to the ensemble-averaged surface mass density $\Sigma(R)$ (Umetsu et al. 2016) (black squares) obtained for 16 X-ray-selected clusters. Models with a probability, p , corresponding to χ^2 is higher than 0.05 are shown with solid lines, while those with $p < 0.05$ are shown with dashed lines. The blue, red and magenta solid curves show the best-fit for NFW, NFW+two halo term and Einasto profiles, respectively. The lower panel shows the deviations in units of σ of the best-fit profiles with respect to the observed Σ profile. *Right:* α -mass relation (Okabe & Smith 2016). The cross denotes the best-fit parameters and the contours show the 68.3%, 95.4%, and 99.7% confidence levels. Blue dashed and green dotted lines are from Dutton & Macciò (2014) and Gao et al. (2008), respectively.

Umetsu et al. (2016) have computed the stacked Σ profile for 16 X-ray selected clusters and constrain $\alpha = 0.232^{+0.042}_{-0.038}$ (left panel of Figure 10). Okabe & Smith (2016) have compared the relation between the shape parameter and mass for 50 X-ray selected clusters with predictions of numerical simulations (Dutton & Macciò 2014; Gao et al. 2008), and found that they are in agreement with each other (right panel of Figure 10). More precise observational constraints on the density profile shape of clusters, including on the mass dependence of the Einasto profile parameters, awaits larger cluster samples from on-going or future surveys.

4.2 X-rays and hybrid SZ

4.2.1 Hydrostatic mass and mass profiles

The launch of *XMM-Newton* and *Chandra* opened the way to precise spatially resolved X-ray spectroscopy, enabling measurement of both the gas density and the temperature profiles, and thus the total mass profile using the HE equation. Pointecouteau et al. (2005) and Vikhlinin et al. (2006a), using respectively *XMM-Newton* and *Chandra*, measured high precision mass profiles for small samples (~ 10) of local ($z < 0.15$) relaxed clusters ($M_A > 10^{14} M_\odot$). Buote et al. (2007) extended this work into the group regime (see also Gastaldello et al. 2007), while Ettori et al. (2010) studied a larger sample, albeit with lower precision, using the *XMM-Newton* archive (44 clusters at $z < 0.3$).

The consistent picture that emerges from these observations is that the dark matter profile is indeed cuspy. Fits with parametric models usually reject profiles with a finite core or are inconclusive (see also Buote & Lewis 2004; Voigt & Fabian 2006). Generally, self-similarity of shape is also evident from all techniques, although there is no quantitative assessment of the intrinsic scatter. All quantitative tests of Λ CDM predictions are based on parametric profile fitting with the NFW profile. X-ray determinations of the $c - M$ relation are consistent with theoretical predictions, and have even been used to provide independent constraints on Ω_m and σ_8 (Buote et al. 2007; Ettori et al. 2010). When constraints can be put on more general profiles, such as the generalised NFW or Einasto profiles (e.g. Voigt & Fabian 2006; Mantz et al. 2016a), the central logarithmic slope has been found to be consistent with unity, i.e. with an NFW profile.

More recent studies have pushed the measurements for relaxed clusters to higher redshifts, e.g. the studies of Schmidt & Allen (2007, 34 relaxed clusters at $0.06 < z < 0.7$), Mantz et al. (2016a, 40 relaxed objects at $0.1 < z < 1.1$), or Amodeo et al. (2016, an archival sample at $0.4 < z < 1.2$), but the individual mass profiles in these studies generally have large uncertainties, particularly at the highest redshifts. The evolution factor of the corresponding $c - M$ relations, expressed as $(1+z)^\alpha$, is consistent with theoretical expectations, but with large uncertainties ($\alpha = 0.71 \pm 0.52$, and $\alpha = 0.12 \pm 0.61$, respectively). Bartalucci et al. (2018, see Fig. 11) have recently reconstructed the hydrostatic mass profiles of the five most massive ($M_{500} > 5 \times 10^{14} M_\odot$) SZ-selected clusters at

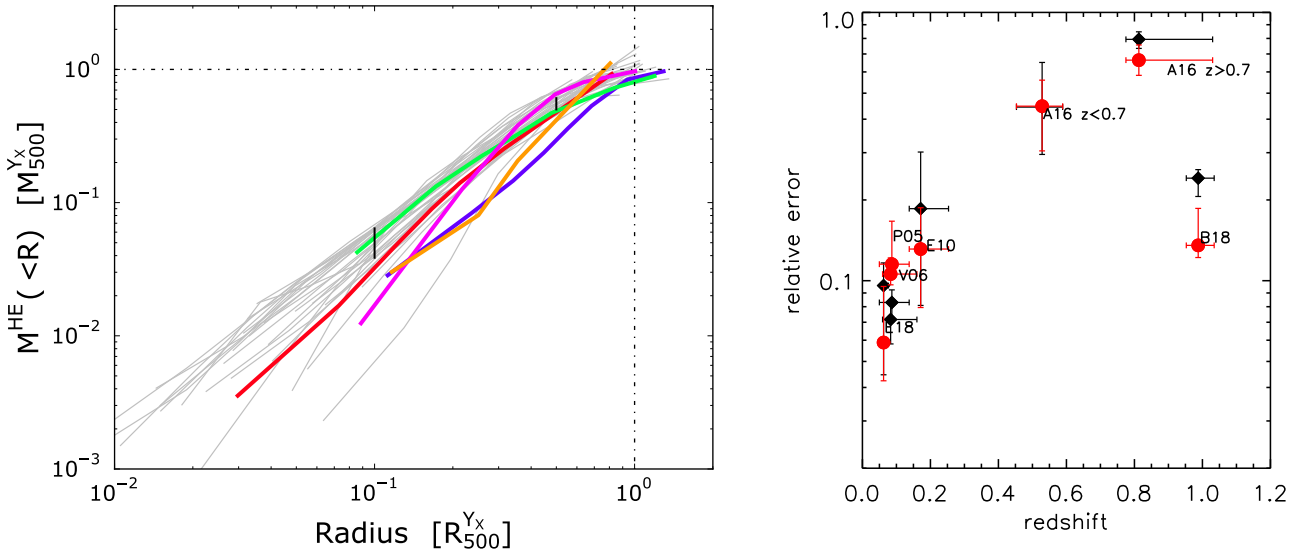


Fig. 11 *Left:* Mass profiles for a sample of five clusters at $z \sim 1$ derived by Bartalucci et al. (2018) using XMM-Newton and Chandra data (coloured lines), compared to local REXCESS mass profiles (grey lines). *Right:* Relative errors (median, and 1st and 3rd quartiles) on the mass (red dots) and NFW concentration (black diamonds) estimated in the following studies: P05 (Pointecouteau et al. 2005), V06 (Vikhlinin et al. 2006a), E10 (Ettori et al. 2010), A16 (Amodeo et al. 2016), E18 (Ettori et al. 2019), B18 (Bartalucci et al. 2018).

high redshift ($z \sim 1$), combining deep observations from XMM-Newton and Chandra. Using both forward and backward methods, they investigated halo shape parameters such as sparsity and concentration, measured to high accuracy. Comparing to local clusters, they found hints for evolution in the central regions (or for selection effects). The total baryonic content is in agreement with the cosmic value at R_{500} . Comparison with numerical simulations shows that the mass distribution and concentration are in line with expectations. Bartalucci et al. (2018) also investigated the sparsity of their sample, finding good agreement with expectations (see also Corasaniti et al. 2018). Typical uncertainties on the NFW concentration as a function of redshift are illustrated in the right hand panel of Fig. 11.

4.2.2 New results from combination with SZ

As detailed in Sect. 3.2.1, a recent observational development is the ready availability of spatially-resolved SZ electron pressure profiles, which can be obtained from geometrical deprojection of the azimuthally-averaged integrated Comptonization parameter. The power of the SZ effect is that it directly measures the line-of-sight pressure. However, measurement of other key thermodynamic quantities such as temperature and entropy requires access to the gas density. This is trivial to obtain from X-ray imaging. Previous studies (e.g. Basu et al. 2010; Planck Collaboration Int. V 2013) have been limited to a few massive local systems due to the intrinsic faintness of the SZ signal and the 1-2 orders of magnitude difference in angular resolution between X-ray and SZ observations.

For local systems ($z < 0.2$), in the most recent works published on the hydrostatic mass, improved data quality and refined analysis techniques have allowed to reach statistical uncertainties on the reconstructed mass of about 10% at R_{200} (see Fig. 12). In nearby ($z < 0.1$) massive systems, the XCOP collaboration (e.g. Ghirardini et al. 2019; Ettori et al. 2019; Eckert et al. 2019) has been able to reconstruct hydrostatic mass profiles out to $2R_{500}$ by combining X-ray and SZ data. They find that (i) the NFW mass model provides, on average, the best-fitting mass model in reproducing the observed radial profiles of relaxed massive nearby systems, with relative errors at R_{200} lower than 10% (see Fig. 12), (ii) alternative models of gravity that do not require any dark matter contribution (such as MOND or Emergent Gravity) show significant tensions when compared with the prediction from the HE equation, (iii) estimates of the dark matter distribution obtained for the same objects with different techniques (as e.g. lensing, galaxy dynamics, scaling laws) are consistent with the hydrostatic mass with differences in the order of 15%.

At higher redshifts ($z > 0.5$), the new sensitive, high resolution SZ instruments such as NIKA2 and Mustang/Mustang2, are potentially game-changers. For example, the angular resolution of NIKA2 is comparable to that of XMM-Newton, over a 6.5' diameter field of view, finally opening the way to effective exploitation of the X-ray/SZ synergy. As an example, Ruppin et al. (2018) recently published a novel non-parametric X-ray/SZ analysis of the cluster PSZ2 G144.83

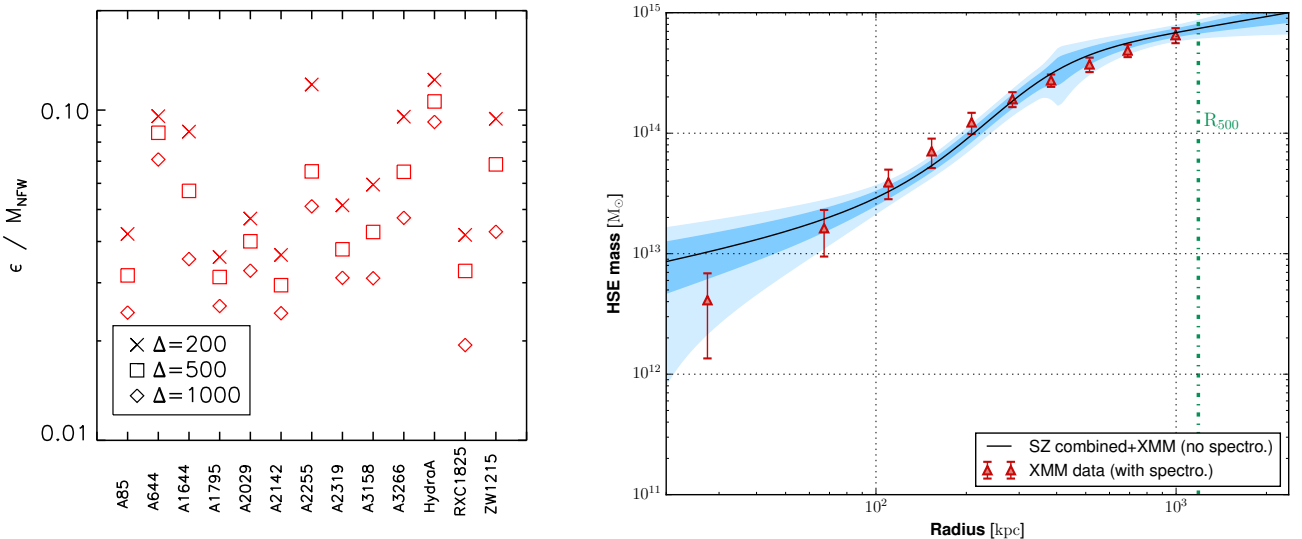


Fig. 12 *Left:* Relative statistical errors on the hydrostatic masses measured at R_{200} in the X-COP sample from Ettori et al. (2019). *Right:* HE mass profile of PSZ2 G144.83 + 25.11 at redshift $z = 0.58$, derived from XMM-*Newton* density and temperature profiles (triangle), compared to the mass profile derived from the XMM-*Newton* density combined with the NIKA2 pressure profile (dark blue region). Figure from Ruppin et al. (2018).

+25.11 at $z = 0.59$. The 150 GHz image at $< 18''$ resolution showed a clear extension to the SW that may be a merging subclump. Excluding this region, the radial profiles resulting from the combination of the density from XMM-*Newton* and the SZ pressure from NIKA2 and *Planck* were in excellent agreement with those obtained from the X-ray data alone (see Fig. 12). The resulting hydrostatic mass profile provides competitive constraints to the X-ray only analysis.

4.2.3 Baryon budget and gas fraction

As described in Sect. 2.5, galaxy clusters are expected to be fair archives of the baryon budget in the Universe. *Planck* data constrain the cosmic baryon fraction with a statistical precision of just 2% ($f_b = 0.156 \pm 0.003$, Planck Collaboration XIII 2016). Thus, the baryon fraction of massive clusters within their virial radius is in principle known with a high level of accuracy, and measurements are highly sensitive to the accuracy of the estimated mass. The ICM contains the vast majority of the baryons, with stars within galaxies and intracluster light typically contributing 1 – 1.5% of the total mass within R_{200} (e.g. Gonzalez et al. 2007, 2013; Leauthaud et al. 2012; Laganá et al. 2013; Coupon et al. 2015; Eckert et al. 2016; Chiu et al. 2017).

Measurements of the ICM gas fraction using hydrostatic mass estimates typically infer gas fractions of 10–15% within R_{500} (Vikhlinin et al. 2006b; Allen et al. 2008; Ettori et al. 2009; Pratt et al. 2010; Mantz et al. 2014a), in good agreement with the expected cosmic baryon budget. However, recent observations extending measurements out to R_{200} and beyond have reported excesses in the gas fraction over the cosmic value when using hydrostatic masses (Simionescu

et al. 2011; Kawaharada et al. 2010; Ichikawa et al. 2013; Ghirardini et al. 2018). Such differences disappear when computing gas fractions with weak-lensing masses (Okabe et al. 2014). On the other hand, several studies have also reported hydrostatic gas fractions consistent with expectations all the way out to the virial radius (Tchernin et al. 2016; Walker et al. 2012, 2013).

Recently, Eckert et al. (2019) reported ICM gas fractions estimated using the HE assumption for the X-COP sample, a sample of 12 clusters with deep XMM-*Newton* X-ray and *Planck* SZ data out to R_{200} and beyond. In the left-hand panel of Fig. 13 we show the gas fraction profiles estimated through a joint fit to XMM-*Newton* and *Planck* SZ data. With the exception of one system, A2319, for which substantial non-thermal pressure support was detected (Ghirardini et al. 2018), all measurements converge towards a gas fraction at the virial radius that is very close to the expected baryon budget.

4.3 Non-thermal pressure, feedback, and the validity of the hydrostatic assumption

4.3.1 Constraints from X-ray and SZ observations

The gas fraction can be used to put constraints on the non-thermal pressure support if it is assumed that the deviations from the expected true (i.e. Universal) value originate from random isotropic gas motions (see Eqn. 10). The ratio of hydrostatic to true gas fraction is related to the non-thermal pressure fraction $\alpha = P_{\text{rand}}/P_{\text{tot}}$ as (see Sect. 3.2 of Eckert

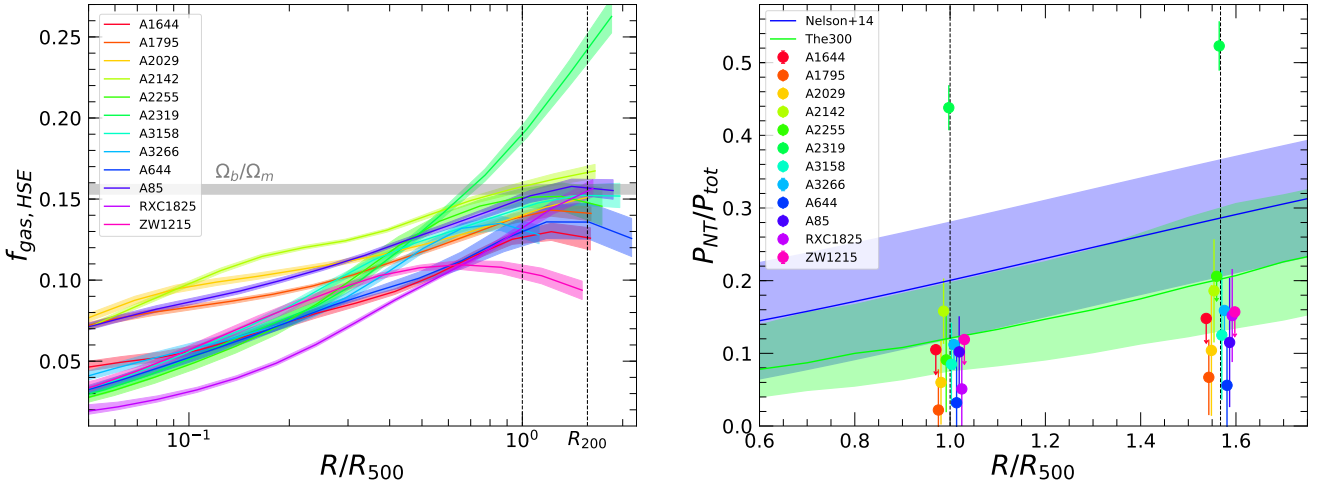


Fig. 13 *Left:* Hydrostatic gas fraction profiles $f_{\text{gas,HE}}(R) = M_{\text{gas}}(< R) / M_{\text{HE}}(< r)$ for 12 clusters in the X-COP sample (reproduced from Eckert et al. 2019). The dashed and dash-dotted vertical lines represent the position of R_{500} and R_{200} , respectively. The horizontal shaded area show the cosmic baryon fraction from Planck CMB (Planck Collaboration XIII 2016). *Right:* Non-thermal pressure fraction at R_{500} and R_{200} inferred by comparing the measured hydrostatic gas fraction of X-COP clusters with the expectations, taking into account baryon depletion and stellar fraction. The blue and green lines and shaded areas are the predictions for the random-to-thermal pressure fraction from two sets of numerical simulations (Nelson et al. 2014a; Cui et al. 2018).

et al. 2019),

$$\frac{f_{\text{gas,HE}}}{f_{\text{gas,true}}} = \left(1 - \frac{P_{\text{th}} R^2}{(1-\alpha) \rho_{\text{gas}} G M_{\text{HE}}} \frac{d\alpha}{dR} \right) (1-\alpha)^{-1}. \quad (40)$$

Taking into account the expected depletion of baryons induced by hydrodynamical processes and the stellar fraction, constraints on the amount of pressure in the form of random gas motions can be obtained.

In the right-hand panel of Fig. 13 we show the inferred non-thermal pressure fraction for the 12 X-COP clusters, which is then compared with the predictions from two different sets of numerical simulations (Ω_{500} , Nelson et al. 2014a; The300, Cui et al. 2018). The median non-thermal pressure fraction is 6% at R_{500} and 10% at R_{200} , which can be translated into a typical Mach number $M_{3D} = \sigma_v/c_s \approx 0.33$ at R_{500} .

While the ICM gas fraction is very sensitive to the hydrostatic mass bias, one may argue whether the assumption that the true baryon fraction should match the cosmic baryon fraction with small ($\sim 5\%$) corrections can be violated. This can occur if a large amount of non-gravitational energy is injected within the ICM, in particular by AGN feedback (see Sect. 2.5). Given the measured gas fractions for the X-COP sample (see Fig. 13), a large hydrostatic bias ($> 20\%$) would imply that a substantial amount of baryons have been driven outside of the virial radius even for the most massive local clusters. These systems contain a total thermal energy of several 10^{63} ergs, implying that feedback energies in excess of 10^{62} ergs are required to substantially deplete the overall baryon fraction. Such an energy input corresponds to an overall AGN luminosity of $\sim 10^{45}$ ergs/s injected continuously

over 10 Gyr, assuming 100% coupling with the ICM and neglecting cooling losses.

The recent high spectral resolution results from *Hitomi* have provided an unprecedented view of gas motions in the Perseus cluster (Hitomi Collaboration et al. 2016, 2018). Although the purpose of these observations was to obtain constraints on the interaction between the central AGN and the surrounding ICM, these unique data have given insight into the level of turbulence close to the core of Perseus. They have shown that even in the presence of the AGN the turbulent line broadening is rather modest ($164 \pm 10 \text{ km s}^{-1}$). Better constraints will be obtained from XRISM and Athena (Sect. 6.2).

The above illustrates that the constraints on departures from HE and the gas depletion due to feedback are linked on a fundamental level, and can be used more as a consistency check than as an absolute constraint. For example, an extreme HE bias of $\sim 60\%$, as would be suggested from the tension between *Planck* SZ cluster counts and CMB, would imply a level of gas depletion that is completely at odds with reasonable feedback prescriptions in cosmological simulations. The two issues should thus be addressed self-consistently in both observations and simulations.

4.3.2 Constraints from X-ray and optical observations

A comparison of HE and WL masses for a large number of clusters is a useful route to test the validity of the HE assumption. The mass bias, b_{WL} , relative to the WL mass,

can be estimated by the geometric mean for targeted clusters,

$$1 - b_{WL} = \exp \left[\left(\sum_i \ln \left(\frac{M_{HE}}{M_{WL}} \right)_i w_i \right) \left(\sum w_i \right)^{-1} \right], \quad (41)$$

where w_i is a weight function ($w_i = 1$ for a uniform weight), or equivalently by fitting the lognormal quantities.

[Mahdavi et al. \(2013\)](#) compared X-ray masses with weak-lensing masses for 50 CCCP clusters and found that the average mass ratio of X-ray to WL masses is $1 - b_{WL} = 0.88 \pm 0.05$ at R_{500} . [Hoekstra et al. \(2015b\)](#) subsequently updated the CCCP WL masses and reported masses on average 19% higher. Thus, applying a factor 1.19 correction to the denominator of the CCCP implies an average mass ratio $1 - b_{WL} \sim 0.74$.

[Smith et al. \(2016\)](#) have compiled 50 LoCuSS clusters at $0.15 < z < 0.3$ and found the mean ratio of X-ray to lensing mass $1 - b_{WL} = 0.95 \pm 0.05$, where X-ray masses ([Martino et al. 2014](#)) used spectroscopic-like temperature ([Mazzotta et al. 2004](#)) and WL masses are from Subaru/Suprime-Cam ([Okabe & Smith 2016](#)). We note that the [Martino et al. \(2014\)](#) X-ray masses are on average $\sim 14\%$ higher than those of [Mahdavi et al. \(2013\)](#).

[Applegate et al. \(2016\)](#) have investigated a lensing to X-ray mass ratio for 12 relaxed clusters from the WtG project, using WL masses ([Applegate et al. 2014](#)) and *Chandra* masses. They reported $b_{WL} - 1 = 0.967^{+0.063}_{-0.092}$ and $1.059^{+0.092}_{-0.092}$ at R_{2500} and R_{500} , respectively.

[Siegel et al. \(2018\)](#) carried out a joint analysis of *Chandra* X-ray observations, Bolocam thermal SZ observations, HST strong-lensing data, and Subaru/Suprime-Cam weak-lensing data for 6 CLASH clusters, and constrained the nonthermal pressure fraction at R_{500} to be < 0.11 at 95% confidence.

A recent analysis of a sample of 16 massive clusters by [Maughan et al. \(2016\)](#) suggested that the mass profiles obtained independently from X-ray hydrostatic and caustic (Sect. 3.1.1) methods agree to better than 20% on average across the radial range probed by the observations. At R_{500} , they measure a mass ratio $M_X/M_C \gtrsim 0.9$, implying a low or zero value of the hydrostatic bias if the caustic masses are assumed to be equivalent to the true mass. Interestingly, [Maughan et al. \(2016\)](#) found no dependence of the M_X/M_C scatter on dynamical state.

To further illustrate the above, we compare in Fig. 14 the X-ray mass measurements from LoCuSS ([Martino et al. 2014](#)), WtG ([Applegate et al. 2016](#)) and CLASH ([Siegel et al. 2018](#)) at $\Delta = 2500$. Since the CCCP X-ray masses ([Mahdavi et al. 2013](#)) are measured within radii determined by the WL mass measurement, we do not include them in the comparison. The *Chandra* and *XMM-Newton* results are denoted by open and solid symbols, respectively. Scatter between each X-ray measurement is significantly larger than that of WL mass measurements (Fig. 8). [Sereno & Ettori \(2015a\)](#), compiling WL and X-ray masses from the literature,

have found that the intrinsic scatter of HE masses ($\sim 20 - 30$ per cent) is larger than that of WL masses ($\sim 10 - 15$ per cent). The *Chandra* masses are generally systematically higher than those from *XMM-Newton* due to the absolute temperature calibration issues described above. The WtG masses are also systematically higher than those of other projects.

4.4 Halo triaxiality

Halo asphericity and orientation induces significant scatter in the projected lensing signals. Simultaneous modelling of the mass, concentration, shape, and orientation using lensing data and/or independent data has been proposed by various papers (e.g. [Oguri et al. 2005](#); [De Filippis et al. 2005](#); [Sereno 2007](#); [Corless et al. 2009](#); [Sereno & Umetsu 2011](#); [Sereno et al. 2013](#); [Umetsu et al. 2015](#)). The previous review by [Limousin et al. \(2013\)](#) gives a good summary of the technique. Lensing information probes the structure and morphology of the matter distribution in projection. X-ray observations provide us with the characteristic size and orientation of the ICM in the sky plane. The elongation of the ICM along the line-of-sight can be constrained from the combination of X-ray and thermal SZ observations, because of a difference of emissivity. Therefore, the triaxial model can be constrained by combining these complementary data. Recently, [Sereno et al. \(2013\)](#) have developed a parametric triaxial framework to combine and couple independent morphological constraints from lensing and X-ray/SZ data, using minimal geometric assumptions. [Umetsu et al. \(2015\)](#) applied the technique to A1689 and found that the mass distribution is elongated with an axis ratio of ~ 0.7 in projection and the thermal gas pressure contributes to $\sim 60\%$ of the total pressure balanced with the mass. [Chiu et al. \(2018\)](#) have carried out a three-dimensional triaxial analysis (see also [Umetsu et al. 2018](#)) for 20 CLASH clusters and obtained a joint ensemble constraint on the minor-to-major axis ratio $q = 0.652^{+0.162}_{-0.078}$. Assuming priors on the axis ratios derived from numerical simulations, they found that the degree of triaxiality for the full samples prefers a prolate geometry for cluster haloes. [Sereno et al. \(2018\)](#) have measured based on a full 3D analysis of lensing, X-ray and SZ measurements shapes of X-ray selected CLASH clusters and found that it is in a good agreement with numerical simulations for dark matter only.

4.5 Mass estimates from mass proxies

The mass estimate is essential both when using clusters to constrain cosmology, and for studying structure formation physics. Mass proxies play an important role in this context. They can provide statistically more precise mass measurements, especially at high redshift and low mass, as compared to WL or hydrostatic masses, and in some cases the masses

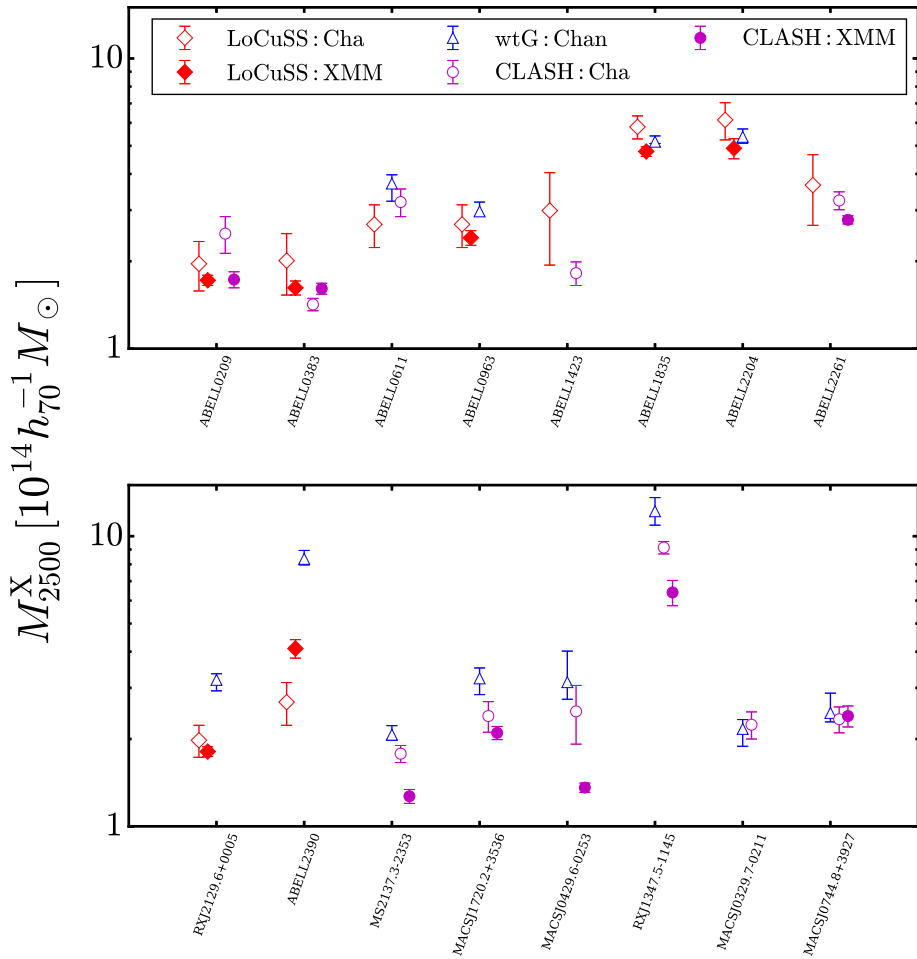


Fig. 14 X-ray mass comparisons of LoCuSS (diamonds), WtG (triangles) and CLASH (circles) at $\Delta = 2500$. Open and solid symbols are from *Chandra* and *XMM-Newton* observations.

from mass proxies may even be less biased (e.g. for highly disturbed systems far from HE).

We recall also that in cluster surveys, objects are never detected directly by the mass, but through their observable baryon signature (i.e. through a mass proxy). The calibration of the corresponding mass proxy scaling relations is always needed to understand the selection function (i.e. the probability that a cluster of a given mass is detected via its given baryon signal). This step is necessary even if individual masses were available for all objects in subsequent follow up, in order to relate the theoretical mass function to the observed number counts.

There is a vast amount of literature on the subject of scaling relations, a discussion of which is beyond the scope of the current paper. A recent observational review can be found in [Giordini et al. \(2013\)](#). We summarise here some important recent advances.

- The precise measurements available from *XMM-Newton* and *Chandra* have enabled excellent convergence in X-

ray scaling relations, calibrated using hydrostatic masses of well-chosen samples of relaxed clusters, to minimize the HE bias. This is illustrated in the left hand panel of Fig. 15, which shows the $M_{500}-Y_X$ relations from [Vikhlinin et al. \(2006a\)](#) and [Arnaud et al. \(2007\)](#) are consistent at the 1σ level, with a normalisation that differs by less than 5%. These measurements have also allowed exploration of the scatter about the scaling relations (for relaxed objects), confirming that the X-ray luminosity is a high-scatter mass proxy except when the core is excised ([Maughan 2007; Pratt et al. 2009; Mantz et al. 2018](#)), and that Y_X is a low-scatter proxy ([Arnaud et al. 2007](#)).

- These scaling relations were then exploited for the cosmological analysis of the X-ray selected sample of [Vikhlinin et al. \(2009b\)](#) and the new SZ samples from [Planck. Planck Collaboration XX \(2014\)](#) combined the $M_{500}-Y_X$ relation obtained on a sample of *relaxed* clusters with masses derived from HE equation ([Arnaud et al. 2010](#)), and the Y_X-Y_{SZ} relation calibrated on the sub-sample

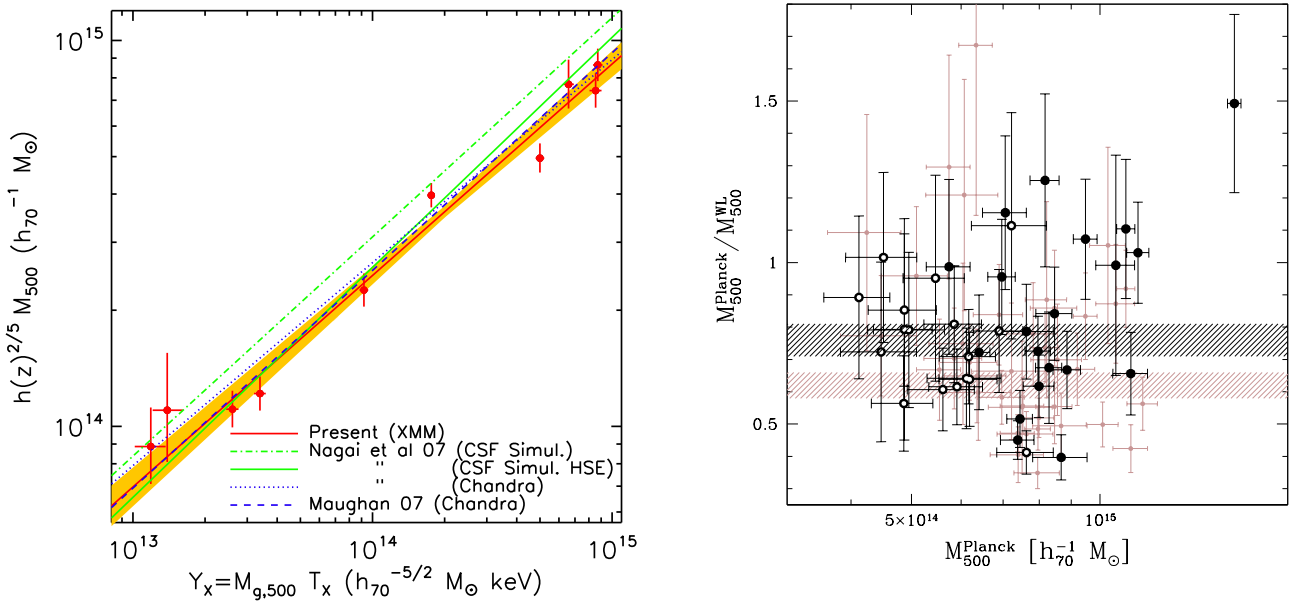


Fig. 15 (Left): The observed M_{500} - Y_X relation from *XMM-Newton* observations of ten relaxed clusters (Arnaud et al. 2007, red points with 1σ uncertainty envelope) compared to the predicted relation from numerical simulations including cooling and galaxy feedback (green dot-dash line, true mass; solid green line, HE mass, from Nagai et al. 2007). The observed relations from *Chandra* are also shown (Nagai et al. 2007; Maughan 2007). (Right): Ratio of the hydrostatic and the weak lensing mass estimates as a function of mass, from Hoekstra et al. (2015b). The CCCP sample yields an average value of 0.76 ± 0.05 (dark hatched region), while the average for the WtG measurements is 0.62 ± 0.04 (pink region).

- of 71 *Planck* clusters in the cosmological sample with archival *XMM-Newton* data. They introduced a mass bias parameter, b , allowing for any difference between the X-ray determined masses and true cluster halo mass: $M_{\text{HE},X} = (1 - b) M_A$. This factor encompasses all systematics in our knowledge of the exact relationship between the SZ signal and the mass (see the extensive discussion in the Appendix of Planck Collaboration XX 2014). Such a difference can arise from cluster physics, such as a violation of HE or temperature structure in the gas, or from observational effects, essentially instrumental calibration. Even with a fiducial $(1 - b) = 0.8$ motivated by numerical simulations, this calibration yielded the well-known tension between cosmology from cluster number counts and the *Planck* CMB cosmology.
- This generated a large effort to recalibrate the relation between *Planck* Y_{SZ} and mass using next-generation WL data from CCCP, WtG, LoCuSS, CLASH, etc, as described above in Sect. 4.3.2. The resulting $1 - b$ from these lensing data is summarised in Table 2 of Planck Collaboration XXIV (2016), and ranges from 0.688 ± 0.072 to 0.780 ± 0.092 , with systematic differences between studies on the $\sim 10\%$ level (Hoekstra et al. 2015b, see right-hand panel of Fig. 15).
 - In parallel, a large effort has been undertaken on the calibration of optical mass proxies based on the richness, exploiting large-area optical surveys such as SDSS. These studies have developed new, robust mass proxies based

on richness (e.g. Rykoff et al. 2012, 2014a), and calibrated them using WL stacking techniques (e.g. Rozo et al. 2009).

- Another key effort has been the critical comparison of various mass estimates, obtained from proxies and/or from direct lensing and/or X-ray analysis, and published in the literature (e.g. Rozo et al. 2014b; Sereno & Ettori 2015b; Sereno 2015; Groener et al. 2016). These studies use the various samples to better understand the relation between different proxies and their associated biases, and have proposed new calibrations based on an approach that aims for consistency between different analyses (Rozo et al. 2014a; Sereno & Ettori 2017). These studies have underlined the necessity to properly take into account the covariance between various quantities, and the need for treatment of the Eddington/Malmquist bias effects due to the scatter about the relations.

The last point is especially important when calibrating the relation between the mass and the survey observable using external mass estimates of a sub sample. This is illustrated in the left hand panel of Fig. 16, which shows the importance of the Malmquist bias in the survey observable. Here Giles et al. (2017), analysing a complete sample of 34 luminous X-ray clusters, found that not correcting for selection biases would result in a 40 per cent underestimation of the mass of a cluster at a given luminosity. As this bias depends on both the cluster mass function and the survey selection function, it is becoming more common to perform a fully-consistent joint

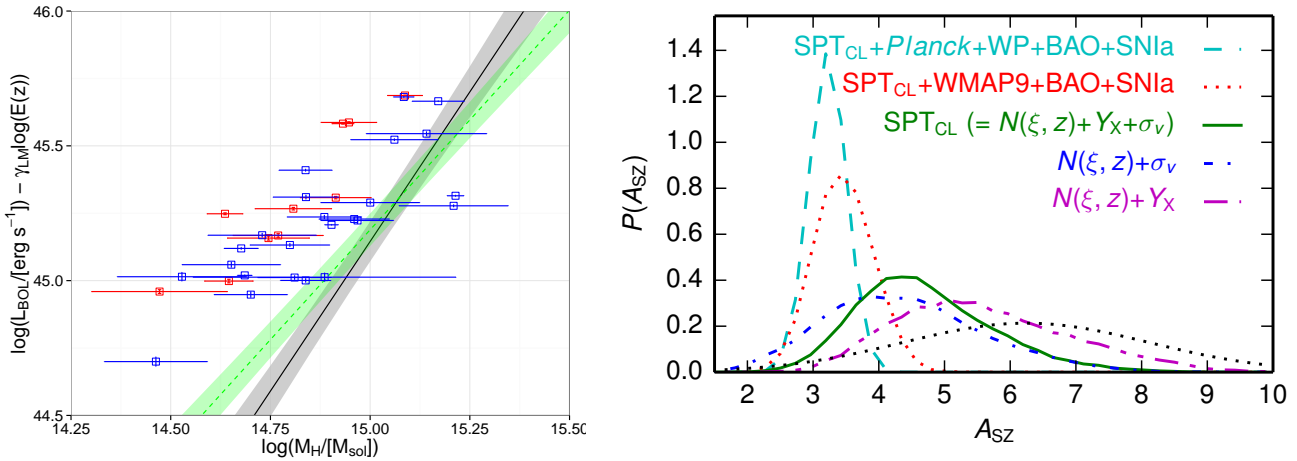


Fig. 16 (Left): Illustration of the importance of selection biases in scaling relations, and the need to take them into account in cosmological analyses using the cluster population. Giles et al. (2017) showed that neglect of selection effects in their sample would lead to a 40 per cent underestimate in the mass for a given luminosity. The solid line in this plot is the estimated relation when selection effects are accounted for. Red points in this plot represent relaxed systems; blue points represent disturbed objects. The green line and shaded area represent the best-fitting relation of Mantz et al. (2010a) and the corresponding 1σ uncertainty. (Right): The normalisation of the M_{500} – Y_{SZ} relation depends on the underlying cosmological prior (Bocquet et al. 2015).

analysis of the scaling laws and cosmological constraints (e.g. Mantz et al. 2014b; de Haan et al. 2016).

However, there is a certain degeneracy between the normalisation of the scaling laws and the cosmology, as discussed further below. In these analyses, it is critically important to understand where the constraints are really coming from when imposing consistency on a multi-dimensional data set. An example is shown in the right hand panel of Fig. 16, taken from Bocquet et al. (2015), which illustrates how the normalisation of the scaling relation depends on the prior on the underlying cosmology.

5 Impact on cosmology with clusters

5.1 Clusters as cosmological probes and the sensitivity to the mass scale

The methods used to estimate cosmological parameters with clusters include use of the baryon fraction (and its evolution), cluster number counts (and their evolution), and the internal cluster shape. All of these approaches require a robust and precise mass estimate. The first two methods have so far provided the most competitive constraints, so in this Section we summarise the nature of these studies, and discuss their sensitivity to the mass scale.

5.1.1 The baryon fraction

In galaxy clusters, the relative amount of baryons and dark matter should be close to the cosmic baryon fraction Ω_b/Ω_m , provided that the measurement has been performed over a

sufficiently large volume inside which the effects of baryonic physics can be neglected. Using X-ray observations, the dominant component of the baryon budget can be well constrained and combined with total mass measurements (from e.g. lensing signal or assuming the HE of the X-ray emitting plasma with the gravitational potential) to recover the gas mass fraction $f_{\text{gas}} = M_{\text{gas}}/M_{\text{tot}}$. When combined with the total stellar content to give the total baryon fraction, f_b , some fundamental cosmological parameters can be constrained. This is because, as first proposed in White et al. (1993), the cosmic matter density Ω_m is equal to $Y_b \Omega_b / f_b$, where Y_b is the depletion parameter indicating the fraction of cosmic baryons that fall into the cluster halo as estimated from hydrodynamical cosmological simulations (see e.g. Planelles et al. 2013). In addition, if f_{gas} is adopted as a standard ruler and assumed to be constant as function of cosmic time in the ‘correct’ cosmology, constraints can be obtained on the dark energy component Ω_Λ (see Sasaki 1996). Here the cosmological constraints come from the dependence of the observed f_{gas} value on the angular distance, $f_{\text{gas}} \propto D_A(z)^{3/2}$ (for X-rays; for SZ, $f_{\text{gas}} \propto (D_A(z))$).

These methods all need a robust and precise calibration of the total gravitating mass. The error on Ω_m and $D_A(z)^{3/2}$ depends linearly on the mass uncertainty with f_{gas} , which can be translated into a corresponding accuracy on Ω_Λ via the functional dependence of $D_A(\Omega_m, \Omega_\Lambda)$ in the z range under consideration. Application of the methods have typically relied on X-ray masses derived from the HE equation (of better statistical precision than lensing mass) and are thus directly sensitive to corresponding systematic effects in the HE mass estimates, in particular the HE bias. Furthermore, a good understanding of the depletion factor and its evolution

is required. This quantity is expected to be more robust for massive systems, where gravity dominates the energy budget over other physical phenomena such as AGN and SN feedback and gas cooling. To minimise these systematics, the methods have been essentially applied using the most massive relaxed systems (e.g. LaRoque et al. 2006; Allen et al. 2008; Ettori et al. 2009; Mantz et al. 2014a).

Conversely, the methods can provide a consistency check of the mass estimates in galaxy clusters, if the cosmological parameters are adopted from independent techniques (such as modelling of the temperature anisotropies in the CMB, or SN). Indeed, a knowledge of Ω_b and Ω_m , combined with the measurements of M_{gas} , which is one of the better constrained quantities from X-ray observations, limits the level of systematics on the measurement of M_{tot} (see Sect. 4.3.1).

5.1.2 The mass function

The mass function, defined as the number of haloes of a given mass per unit volume, can be written as:

$$\frac{dN}{dM}(M, z) = f(\sigma_M) \frac{\rho_m(z=0)}{M} \frac{d \ln \sigma_M^{-1}}{dM}, \quad (42)$$

where $\rho_m(z=0)$ is the mean matter density at $z=0$, and σ_M is the power spectrum of density perturbations (Jenkins et al. 2001; Tinker et al. 2008). Its dependence on mass and redshift can be written as:

$$\sigma_M(M, z) = \sigma_M(M, z=0) D_{\text{grow}}(z) \\ \text{with } \sigma_M(M, z=0) \sim \sigma_8 \left(\frac{M}{M_8} \right)^\alpha \quad (43)$$

where $D_{\text{grow}}(z)$ is the growth factor, and considering that the present day power spectrum $\sigma_M(M, z=0)$ is close to a power law at cluster scales, with $\alpha \sim -1/3$. The logarithmic derivative term in Eqn. 42 is approximately constant, and the mass function depends on mass and σ_8 essentially as:

$$\frac{dN}{dM} \propto f(\sigma_8 M^\alpha)/M \quad (44)$$

The mass function is thus very sensitive to σ_8 , via the exponential behaviour of the function

$$f(\sigma) \propto [1 + (\sigma/b)^{-\alpha}] \exp(-c/\sigma^2). \quad (45)$$

The determination of σ_8 will thus essentially be degenerate with any mass bias, expressed as $M_{\text{obs}} = (1-b) M_{\text{true}}$, along the degeneracy line $\sigma_8(1-b)^{-\alpha} = \text{cst}$, i.e. $\sigma_8 \propto (1-b)^{1/3}$ or $(1-b) \propto 1/\sigma_8^3$.

5.2 Recent results on cosmological constraints from galaxy clusters and their dependence on the mass determination

In the last ~ 5 years there has been significant progress in cluster cosmology, including new samples selected in different wavebands and improved treatments of cluster masses. In the following we call a mass calibration procedure ‘internal’ if mass measurements are available for (a subset of) the clusters in the sample used for the cosmological tests; we call it ‘external’ if the mass calibration is based on other clusters, e.g. a scaling relation from the literature. As discussed above, the cosmological parameters σ_8 and Ω_M are particularly strongly affected by systematic mass uncertainties therefore we list those constraints as well.

Figure 17 shows galaxy cluster constraints on σ_8 from the last ~ 5 years, plus selected other constraints (cosmic shear/galaxy clustering and CMB). The Figure shows results from the following studies.

– X-ray samples:

Pacaud et al. (2016, 2018): These mass function constraints are based on the XXL sample of 178 X-ray selected galaxy clusters detected out to $z = 1$. A mostly internal WL mass calibration of a subset of clusters is performed. For $\Omega_M = 0.3$ the authors approximately find $\sigma_8 = 0.752 \pm 0.060$. These uncertainties are large because they use a large prior on $h = 0.7 \pm 0.1$, use only the redshift distribution (which peaks around $0.3 < z < 0.5$), and allow for a large prior on the evolution of cluster luminosities in the scaling laws $(L(T, z)/L(T, z=0) = E(z)^{0.47 \pm 0.68})$.

Schellenberger & Reiprich (2017b): The sample of the X-ray brightest clusters in the sky is used (HIFLUGCS, 64 clusters with $\bar{z} = 0.05$). The focus of this work is not on using large numbers of clusters but on taking advantage of very high-quality data for all objects in the sample (i.e., 100% internal mass ‘calibration’). This includes on average about 100 ks of *Chandra* data and 200 cluster galaxy velocities per cluster. Hydrostatic masses are taken from Schellenberger & Reiprich (2017a) and dynamical masses from Zhang et al. (2017). Furthermore, a comparison to *Planck* ‘SZ masses’ is undertaken. They find $\sigma_8(\Omega_M/0.3)^{0.5} = 0.793^{+0.029}_{-0.026}$ for their default results combining mass function, and f_{gas} , and $\sigma_8(\Omega_M/0.3)^{0.5} = 0.759^{+0.040}_{-0.042}$ when using the mass function alone.

Mantz et al. (2015): The mass function is determined using 224 clusters from RASS-selected samples, extending to $z = 0.5$. *Chandra* and ROSAT X-ray data for 94 clusters are used for gas mass determinations. Weak gravitational lensing data from the WtG project are used directly

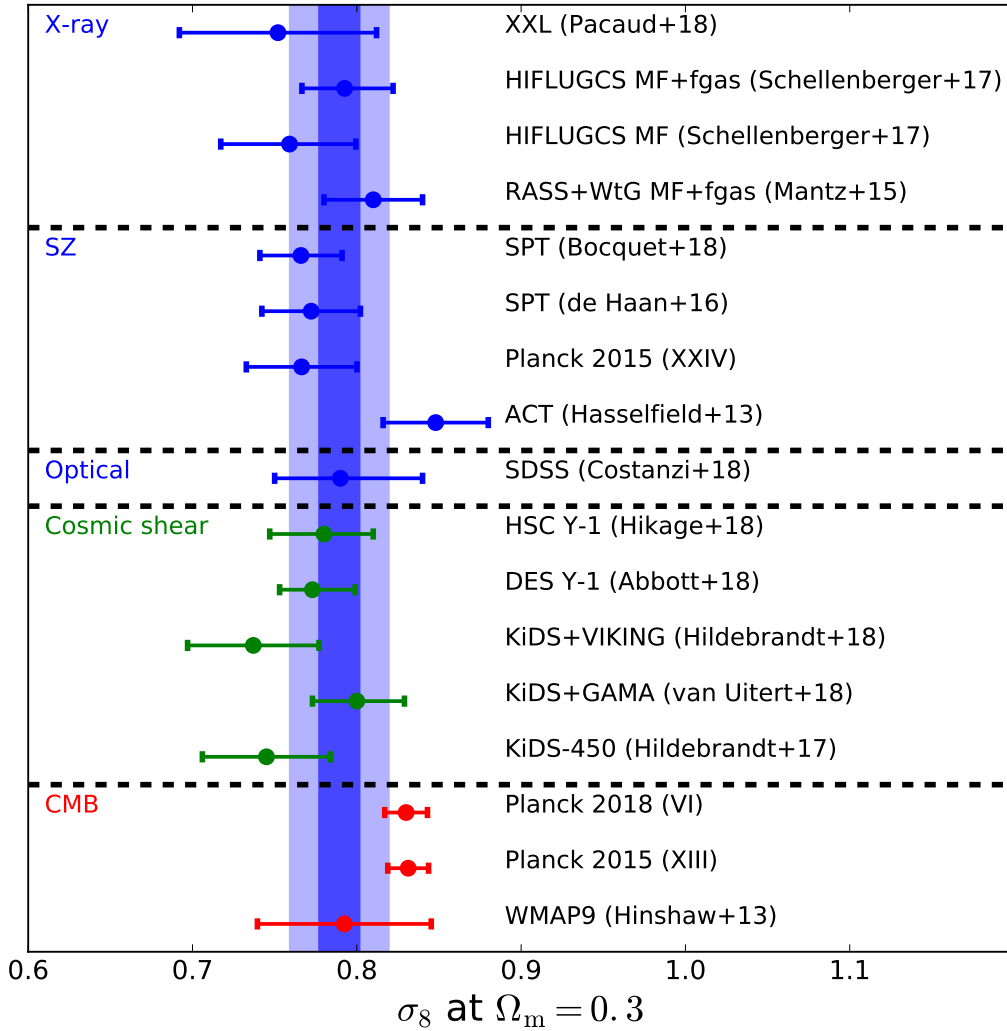


Fig. 17 Constraints on σ_8 at $\Omega_M = 0.3$ from the cluster mass function (sometimes combined with f_{gas} constraints) are shown with blue symbols. Standard deviation ($= 0.033$) and error ($= 0.012$) around the unweighted mean ($= 0.789$) of all seven independent cluster analyses are shown as light and dark blue shaded bands, respectively. Also shown are constraints from WL/cosmic shear/galaxy clustering (green symbols) and from CMB (red symbols). Details on all the constraints are provided in Sections 5.2 and 5.3. Note that analysis details differ for the various works. Adapted from Schellenberger & Reiprich (2017b).

for the 27 internal clusters and for 23 further clusters through the (therefore partially external) gas mass–total mass relation. Furthermore, the f_{gas} constraints described in the paragraph below are incorporated. Shear profiles are compared to an NFW model with $c = 4$ for the lensing mass determination, the cosmology-dependence of the predicted NFW model is accounted for. They find $\sigma_8(\Omega_M/0.3)^{0.17} = 0.81 \pm 0.03$.

Mantz et al. (2014a): The gas mass fraction, f_{gas} , for a sample of 40 massive, relaxed clusters is determined at a range of redshifts. The nearby clusters are used to constrain Ω_M and the apparent evolution of the gas mass fraction to constrain dark energy parameters. Gas masses

are obtained from *Chandra* X-ray observations; total masses from X-ray hydrostatic analysis and, for a subset of 12 clusters, weak gravitational lensing observations from the WtG project. The radial range $0.8\text{--}1.2 R_{2500}$ is exploited for these measurements. The cosmology-dependence of the f_{gas} measurements is taken into account self-consistently, including modelling the radial dependence of f_{gas} as an *average* power law in the relevant range. The mass calibration is internal. They find $\Omega_M = 0.27 \pm 0.04$.

Mantz et al. (2016b): The authors study the mass distribution of 40 relaxed clusters from the Weighing the

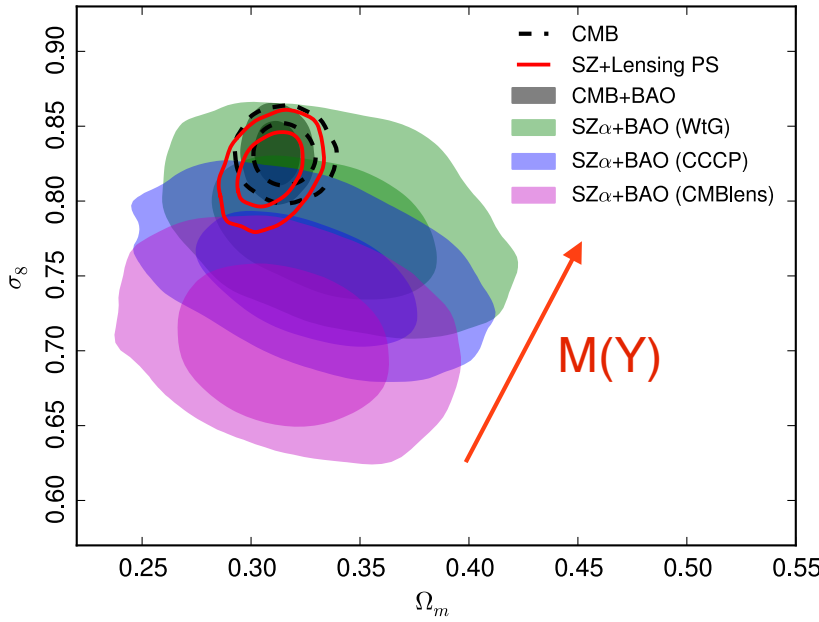


Fig. 18 Dependence of the constraints on cosmological parameters σ_8 and Ω_m on the normalisation of the $M_{500}-Y_{\text{SZ}}$ relation. Each coloured contour represents the cosmological constraints for a given prior on the mass normalisation. The red arrow indicates the effect of an increasing normalisation of the $M_{500}-Y_{\text{SZ}}$ scaling relation. Reproduced from Planck Collaboration XXIV (2016); Arnaud (2017).

Giants sample. They find consistency with a simple NFW profile in the central parts, but also significant scatter.

Böhringer et al. (2017a) determine the cluster mass function at 10% level of uncertainty over the mass range $3 \times 10^{12} - 5 \times 10^{14} M_\odot$ by fitting the observed cluster X-ray luminosity distribution from the REFLEX II galaxy cluster survey. They conclude that about 14% (4.4%) of the matter in the Universe is bound in clusters with a mass larger than $10^{13}(10^{14})M_\odot$, and that it is unlikely that any cluster with a mass $M_A \gtrsim 10^{15} M_\odot$ is present at $z > 1$.

Böhringer et al. (2017b) present the NORAS II galaxy cluster survey, based on X-ray data from the northern part of the RASS down to a flux limit of 1.8×10^{-12} erg s $^{-1}$ cm $^{-2}$ (0.1-2.4 keV), containing 860 objects with a median redshift of 0.1. They constrain σ_8 and Ω_m using the X-ray luminosity, finding results that are in agreement with their previous findings (Böhringer et al. 2014).

- SZ samples:

Planck Collaboration XXIV (2016): The cluster sample consists of 439 clusters selected from Planck data. Internal mass calibrations based on gravitational lensing are applied, including as baseline the CCCP (Hoekstra et al. 2015a) constraints. For their baseline assumptions (CCCP+BAO+BBN) they find $\sigma_8(\Omega_M/0.31)^{0.3} = 0.774 \pm 0.034$. Planck Collaboration XXIV (2016) explored several different mass normalisations, including for the first time a calibration based on CMB lensing (Melin & Bartlett 2015). Figure 18 illustrates the dependence of the cosmological constraints on the mass

normalisation. These results refine and confirm the previous results of Planck Collaboration XX (2014), for which the (internal) mass calibration came from an $M_{500}-Y_{\text{SZ}}$ relation calibrated from X-ray data, with a bias estimated from comparison to numerical simulations, as discussed extensively in the Appendix of Planck Collaboration XX (2014).

de Haan et al. (2016): For the mass function constraints 377 clusters with $z > 0.25$ are selected from the South Pole Telescope (SPT) survey⁴. An external WL mass calibration is applied as well as an additional constraint from Chandra data for 82 clusters. Note that the central value and uncertainties in the arXiv version (arXiv:1603.06522v1) differ from those in the published version. Here, we use the results from the published version: $\sigma_8(\Omega_M/0.27)^{0.3} = 0.797 \pm 0.031$. This analysis has been expanded recently to internal WL mass calibration in Bocquet et al. (2018), who find $\sigma_8(\Omega_M/0.3)^{0.2} = 0.766 \pm 0.025$.

Hasselfield et al. (2013): The mass function is determined using 15 Atacama Cosmology Telescope (ACT)⁵ clusters, using external mass calibration. We show the BBN+H0+ACTcl(B12) constraints from their Tab. 3, which assume a fixed scaling relation: $\sigma_8(\Omega_M/0.27)^{0.3} = 0.848 \pm 0.032$.

- Optical samples:

Costanzi et al. (2018): Clusters selected from a redMaPPer (Rykoff et al. 2014b) search of the Sloan Digital

⁴ <https://pole.uchicago.edu/spt/>

⁵ <https://act.princeton.edu/>

Sky Survey (DR8) are used. Weak lensing mass profiles stacked in richness bins from the same data are employed for internal mass calibration. They find $\sigma_8(\Omega_M/0.3)^{0.5} = 0.79^{+0.05}_{-0.04}$.

– Other constraints shown in Fig. 17:

Hikage et al. (2018): Cosmic shear constraints from the Subaru Hyper Suprime-Cam first-year data. They find $\sigma_8(\Omega_M/0.3)^{0.5} = 0.780^{+0.030}_{-0.033}$.

Hildebrandt et al. (2018, 2017); van Uitert et al. (2018): Cosmic shear constraints from the VST KiDS survey. They find, respectively $\sigma_8(\Omega_M/0.3)^{0.5} = 0.737 \pm 0.040$, 0.745 ± 0.039 , and $0.800^{+0.029}_{-0.027}$.

Abbott et al. (2018): DES Y-1 constraints from galaxy clustering and WL. Note that the central value and uncertainties in the arXiv version (arXiv:1708.01530v1) differ from those in the published version. Here, we use the results from the published version: $\sigma_8(\Omega_M/0.3)^{0.5} = 0.773^{+0.026}_{-0.020}$.

Planck Collaboration VI (2018); Planck Collaboration XIII (2016): Planck 2018 (VI) and Planck 2015 (XIII) constraints from the CMB. For the former, we show the TT,TE,EE+lowE+lensing results from the ‘Combined’ column of their Table 1: $\sigma_8(\Omega_M/0.3)^{0.5} = 0.830 \pm 0.013$. For the latter, we show the TT,TE,EE+lowP+lensing results⁶ from their Tab. 4: $\sigma_8(\Omega_M)^{0.5} = 0.4553 \pm 0.0068$

Hinshaw et al. (2013): WMAP9 constraints from the CMB. We show the values quoted in their Section 5: $\sigma_8(\Omega_M)^{0.5} = 0.434 \pm 0.029$.

5.3 Summary and Interpretation

Figure 17 leads us to draw the following conclusions:

- All the recent cluster constraints agree surprisingly well with each other within the uncertainties despite the fact that they differ dramatically in selection, mass treatment, and analysis. One apparent slight exception is the ACT result for fixed default scaling relation; however, on the one hand, this is expected statistically given seven independent constraints and, on the other hand, as *Hasselfield et al. (2013)* describe in their paper (see, in particular, their Fig. 14) choosing a different fixed scaling relation (their ‘UPP’) would in fact bring σ_8 *below* the mean of all the cluster results.

⁶ Note that because of this choice these constraints are tighter than the ones shown in *Schellenberger & Reiprich (2017b)*.

- The standard deviation of the cluster results is comparable to the typical uncertainty of the individual results, which can be viewed as indication that confirmation bias is small among the cluster results.
- The cosmic shear/galaxy clustering results agree with the cluster results within their uncertainties.
- The CMB constraints from WMAP agree with the cluster and cosmic shear results.
- The *Planck* CMB constraints are close to all of the above, but outside the standard error of the mean of the cluster results.

The general agreement between different probes seems healthy, and one could argue that within the statistical expectations and the still reasonably small ($\ll 25$) total number of constraints, there is nothing to be excited about. However, progress in physics (also) comes from measurement disagreements, and, initially, these are typically small. Let us briefly outline possible interpretations of the slight tension between the mean cluster constraints ($\sigma_8 = 0.789 \pm 0.012$) and the *Planck Collaboration VI (2018)* CMB constraints ($\sigma_8 = 0.830 \pm 0.013$).

The first suspect is unaccounted-for systematic effects. For both clusters and CMB these might come from, e.g. instrumental calibration or modelling issues. For galaxy clusters, further sources of systematic uncertainty include cluster selection effects and the mass determination, and this review article indeed focusses on the cosmological impact of the latter.

Other, more exotic explanations can also be brought to bear. In terms of physics and cosmology, a summed neutrino mass higher than the minimum mass, ~ 0.06 eV, might help alleviate the tension. It is also interesting to speculate about possible more exotic physics that might be causing this tension. For instance, a modification of gravity, a self-interacting dark matter component, warm dark matter, or a dark energy component that interacts with dark matter would all change the predicted mass function.

6 The future

6.1 New surveys and samples

6.1.1 X-ray

X-ray surveys: The ROSAT All-Sky Survey (RASS) was performed almost 30 years ago and many cluster cosmology samples have been derived from it (e.g. Section 5.2). New opportunities based on this venerable dataset include running more sophisticated source detection algorithms, as well as combining the X-ray data with a wealth of new multiwavelength data, particularly in the optical/IR and sub-mm/mm (SZ) regimes.

As an example for the former, Xu et al. (2018) recently showed that galaxy groups and clusters with unusually extended surface brightness profiles were missed in previous RASS cluster surveys. They achieved this by employing a dedicated source detection pipeline particularly sensitive to extended low surface brightness emission, while many of the previous RASS source catalogues were constructed using detection methods optimized for point sources. If missed clusters are not accounted for, their number density will be underestimated, resulting in underestimated values for Ω_M and/or σ_8 (e.g., Fig. 10 in Schellenberger & Reiprich 2017b); i.e. a qualitatively similar effect as a systematic underestimate of cluster masses. Whether or not the unaccounted-for missed fraction is large enough to significantly affect cosmological parameter constraints derived from previous RASS cluster samples is not yet clear.

Examples of the multiwavelength studies include Schuecker et al. (2004) and Tarrío et al. (2018) who combined RASS data in a matched filter approach for joint detection with SDSS and *Planck* data, respectively. They showed that detection probability, purity, and source identification can be improved in such an approach.

With the still-functioning satellites XMM-*Newton* and *Chandra*, progress is being made particularly in surveys for new clusters serendipitously detected using archival XMM-*Newton* observations. Recent examples include, e.g. the XMM-*Newton* Cluster Survey (XCS-DR1 Mehrtens et al. 2012), the XMM-*Newton* CLuster Archive Super Survey (XCLASS; Clerc et al. 2012; Ridl et al. 2017), and XXL (Pacaud et al. 2016, 2018). These surveys have by now detected well over 1 000 new clusters. Given these surveys are typically much deeper but cover a much smaller area than the RASS, the recovered cluster populations are typically at higher redshifts and/or have lower masses.

Mass and mass proxy calibration A large amount of effort continues to be put into follow-up and archival studies of the mass and calibration of the mass proxy relations. Some examples of recent *Chandra* and XMM-*Newton* archival and/or dedicated follow-up of *Planck*-, SPT-, and ACT-selected clusters, include Planck Collaboration XI (2011), Planck Collaboration Int. III (2013), Planck Collaboration XX (2014), Lovisari et al. (2017), Bulbul et al. (2018), Menanteau et al. (2013), and of RASS-selected clusters (e.g. eeHIFLUGCS, Reiprich 2017). The high-quality X-ray data enable many cluster studies but also the determination of hydrostatic masses as well as very precise mass-proxies like the gas mass, temperature, or the Y_X parameter.

One outcome of these studies has been that the comparison of *Planck* SZ-selected clusters with X-ray selected clusters (Rossetti et al. 2016, 2017; Andrade-Santos et al. 2017; Lovisari et al. 2017) has indicated that there may be a tendency in X-ray surveys to preferentially detect clusters

with a centrally-peaked morphology, which are more luminous at a given mass, and on average more relaxed. This raises concerns about how representative the X-ray selected samples, used to define our current understanding of cluster physics and to calibrate numerical simulations, have been. In addition, mass comparisons between various samples are hampered by the heterogeneous nature of the data. A large effort is now ongoing, in the form of a multi-year heritage project on the XMM-*Newton* satellite, to obtain homogeneous X-ray and lensing mass estimates up to R_{500} , of a well-defined *Planck* SZ-selected sample of more than 100 clusters.

6.1.2 Microwave

The recent arrival of large-area SZ galaxy clusters surveys, by ACT (Marriage et al. 2011; Hasselfield et al. 2013), SPT (Bleem et al. 2015) and *Planck* (Planck Collaboration VIII 2011; Planck Collaboration XXIX 2014; Planck Collaboration XXVII 2016) has resulted in a rapid growth in the number of known, massive galaxy clusters especially at $z > 0.5$ – a regime which was classified as ‘high redshift’ by the galaxy cluster community as recently as a decade ago due to the paucity of known systems at these distances. To date, on the order of 1000s of massive galaxy clusters have been detected through blind surveys using the thermal SZ effect. SZ surveys have the advantage over more traditional cluster-detection methods (e.g. X-ray, optical, near-IR) in that they are roughly redshift independent, selecting only on mass.

There is also a strong complementarity in the coverage of the mass-redshift plane between the new SZ surveys and their X-ray counterparts. The spatial resolution of ACT and SPT ($\sim 1'$) allows them to probe the cluster population above a nearly constant mass threshold up to very high redshift, $z \sim 1.5$, but their smaller area limits the number of high mass objects. The lower spatial resolution of *Planck* ($\sim 5'$) is offset by its being the first all-sky blind survey since the *ROSAT* All Sky Survey (RASS). Although less sensitive, it is uniquely suited to finding high mass, high redshift systems.

In the future, one way to improve the cluster mass calibration is through lensing of the CMB (Melin & Bartlett 2015; Planck Collaboration XXIV 2016; Baxter et al. 2018). CMB-cluster lensing offers a robust and accurate way to constrain galaxy cluster masses, especially at high redshift ($z > 1$) where optical lensing measurements are challenging. With CMB lensing we expect to improve mass uncertainty to 3% for upcoming experiments such as AdvACT, SPT-3G etc., and to 1% for next generation CMB experiments such as CMB-S4 (discussed below).

6.1.3 Lensing and optical/IR

On-going imaging surveys (HSC-SSP, DES, and KiDS) enable identification of galaxy clusters using luminous red

Table 2 Wide-field survey properties (Mandelbaum et al. 2018; Zuntz et al. 2018; Kuijken et al. 2015). ^(a) surveys, ^(b) bands, ^(c) planned survey area, ^(d) limiting magnitude, ^(e) the number of background galaxies for weak-lensing analysis, and ^(f) typical seeing-size for shape measurements

Survey ^(a)	Bands ^(b)	Area ^(c) (deg ²)	$m_{\text{lim}}^{(d)}$ (ABmag)	$n_g^{(e)}$ (arcmin ⁻²)	Seeing ^(f) (arcsec)
HSC-SSP	<i>grizy</i>	1400	$r \sim 26.4$ ($S/N = 5$)	~ 25	~ 0.58
DES	<i>grizY</i>	5000	$r \sim 23.3$ ($S/N = 10$)	~ 7	~ 0.9
KiDS	<i>ugri</i>	1500	$r \sim 24.9$ ($S/N = 5$)	~ 7	~ 0.66

galaxies and weak-lensing mass maps, and/or enable direct weak-lensing mass measurements of galaxy clusters. The respective survey properties are summarised in Table 2.

The HSC-SSP survey⁷ (Aihara et al. 2018b) is an ongoing wide-field imaging survey using the HSC (Miyazaki et al. 2018b) which is a new prime focus camera on the 8.2m-aperture Subaru Telescope, and is composed of three layers of different depths (Wide, Deep and UltraDeep). The Wide layer is designed to obtain five-band (*grizy*) imaging over 1400 deg². The HSC-SSP survey has both excellent imaging quality (~0.7" seeing in *i*-band) and deep observations ($r \lesssim 26$ AB mag). Oguri et al. (2018) constructed a CAMIRA cluster catalogue from HSC-SSP S16A dataset covering ~ 240 deg² using the CAMIRA algorithm (Oguri 2014) which is a red-sequence cluster finder based on the stellar population synthesis model fitting. The catalogue contains ~ 1900 clusters at $0.1 < z < 1.1$. Miyazaki et al. (2018a) have searched galaxy clusters based on weak-lensing analysis of the 160 deg² area and discovered 65 shear-selected clusters of which signal-to-noise ratio is higher than 4.7 in the weak-lensing mass map.

The DES survey⁸ (Dark Energy Survey Collaboration et al. 2016b) covers a 5000 deg² area of the southern sky using the new Dark Energy Camera (DECam) mounted on the Blanco 4-meter telescope at the Cerro Tololo Inter-American Observatory. Rykoff et al. (2016) have applied a photometric red-sequence cluster finder (redMaPPer) to 150 deg² of Science Verification and found ~ 800 clusters at $0.2 < z < 0.9$.

The Kilo-Degree Survey⁹ (KiDS; de Jong et al. 2015) covers 1500 deg² using the VLT Survey Telescope (VST), located at the ESO Paranal Observatory. Bellagamba et al. (2019) have developed Adaptive Matched Identifier of Clustered Objects (AMICO) algorithm and applied to ~ 440 deg² survey data. They found ~ 8000 candidates of galaxy clusters in the redshift range $0.1 < z < 0.8$ down to $S/N > 3.5$ with a purity approaching 95% over the entire redshift range.

The optical and weak-lensing cluster finders are complementary to the ICM observations through the SZ and X-ray method. Future multi-wavelength comparison for optical,

shear-selected, X-ray and SZ clusters will give detailed insights into cluster physics and the sample selection functions.

6.2 Next-generation data

6.2.1 *e*ROSITA

*e*ROSITA¹⁰ is the main instrument onboard the Spektrum-Roentgen-Gamma satellite to be launched in 2019 (Predehl et al. 2014). It will perform eight X-ray all-sky surveys resulting in at least 20 times higher sensitivity than the RASS (Merloni et al. 2012). The primary science driver is the study of dark energy with galaxy clusters. *e*ROSITA is expected to detect about 100,000 galaxy clusters (Pillepich et al. 2012, 2018; Clerc et al. 2018). For a small subsample (~2 000 clusters) precise gas temperatures will be measured directly from the survey data (Borm et al. 2014; Hofmann et al. 2017). Competitive constraints on dark energy are expected: e.g., $\Delta w_0 = \pm 0.07$ and $\Delta w_a = \pm 0.25$ in an optimistic scenario with accurate mass calibration down to the low-mass galaxy group regime (Pillepich et al. 2018, see Fig. 19), making *e*ROSITA one of the first Stage IV dark energy experiments. Mock light cones based on cosmological simulations and including, e.g., expected *e*ROSITA photon count rates, are publicly available (Zandanel et al. 2018). The dependence of *e*ROSITA cosmological constraints on the mass calibration accuracy are shown in Fig. 20.

As discussed in Section 5.2, precise and accurate internal mass calibration is important. For *e*ROSITA, the plan is to rely particularly on weak gravitational lensing mass calibration using data from, e.g., the VST, DECam, and HSC surveys, and later from Euclid and LSST (Merloni et al. 2012; Grandis et al. 2018).

6.2.2 *Euclid* and LSST

The LSST¹¹ (Ivezic et al. 2008) will cover 20,000 deg² south of +15 deg, with a limiting magnitude of 26.9 during ten years of operation. The LSST will have first light in 2020, and start the operations phase in 2022. LSST will construct a large catalogue of clusters detected through their member

⁷ <https://hsc.mtk.nao.ac.jp/ssp/>

⁸ <https://www.darkenergysurvey.org/>

⁹ <https://kids.strw.leidenuniv.nl/>

¹⁰ <https://www.mpe.mpg.de/eROSITA>

¹¹ <https://www.lsst.org/>

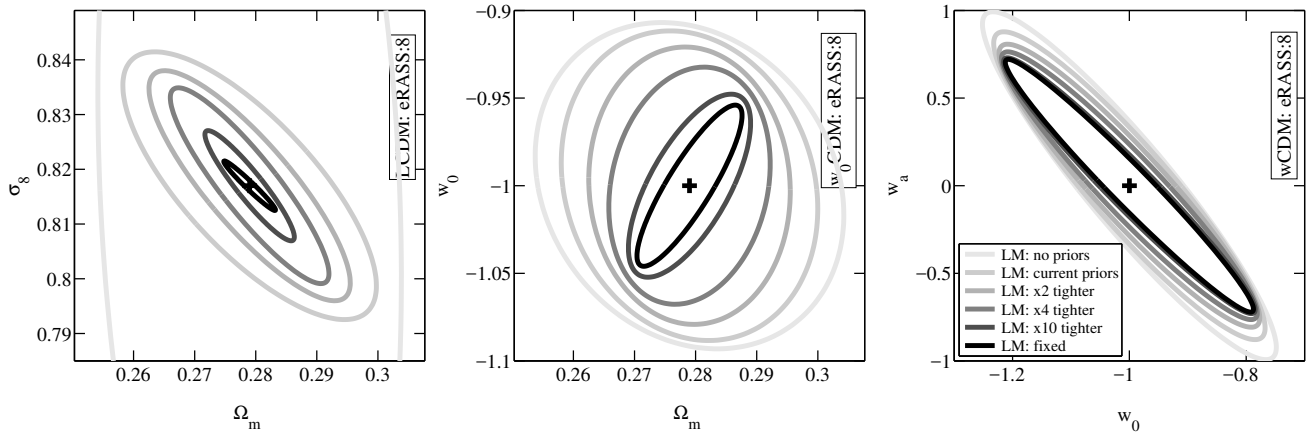


Fig. 19 Expected constraints on cosmological parameters from *eROSITA* (cluster mass function plus clustering) and their dependence on the mass calibration precision. For this purpose, the $L_X - M$ relation is modelled as a powerlaw with four parameters. The different grey shades illustrate increasing precision coming from direct mass measurements. Light grey means the parameters are completely unconstrained while black shows the constraints when fixing them (see inset on the right figure). As the authors describe, the improvement is strongest for the $\Omega_M - \sigma_8$ plane and weakest for the $w_0 - w_a$ plane. Reproduced from Pillepich et al. (2018) with permission.

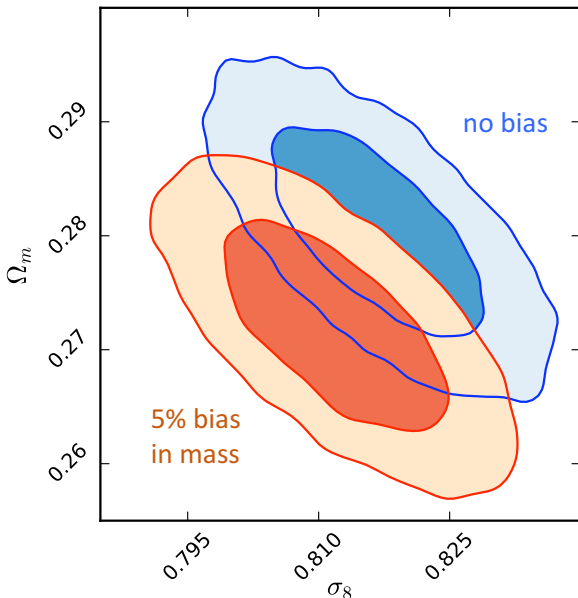


Fig. 20 Illustrative predicted *eROSITA* constraints on Ω_M and σ_8 from the cluster mass function and their dependence on the mass calibration accuracy. For the blue contours unbiased mass estimates are assumed while for the red ones a systematic mass bias of 5% is simulated. Shown are the 68% and 95% credibility levels as dark and light shades, respectively. One notes that, for *eROSITA*, this mass bias results in a significant (at the 95% credibility level) bias for these cosmological parameters. Figure credit: Katharina Borm.

galaxy population to redshift $z \sim 1.2$. Mass calibration using WL mass measurements will measure the cluster mass function. The LSST Dark Energy Science Collaboration (2018) have reported observational requirements for a dark energy analysis consistent with the Dark Energy Task Force definition of a Stage IV dark energy experiment, using conservative assumptions based on current observational resources.

The Euclid survey¹² (Laureijs et al. 2011; Racca et al. 2016) is a space-based optical/near-infrared survey mission that will operate at L2. A Euclid wide survey will cover $15,000 \text{ deg}^2$ with limiting magnitude $24 - 24.5$ during six-years of operations; the deep survey will cover 40 deg^2 at

about two magnitudes deeper. The Euclid survey will collect shape and photo-z for 1.5×10^9 background galaxies ($\sim 30 \text{ per arcmin}^{-2}$) available for WL mass measurements and spectra for 5×10^7 galaxies. The Euclid surveys will show the three-dimensional distribution of dark and luminous matter up to $z \sim 2$. Euclid will find $\sim 2 \times 10^5$ clusters with a S/N greater than 5 at $0.2 < z < 2$ (Sartoris et al. 2016), especially at $z > 1$ thanks to the near-infrared bands.

Ground-based telescopes are helpful to collect photometry in optical bands for an accurate estimation of photometric redshifts in a combination with Euclid bands. The on-going survey data from the DES, HSC-SSP, and KiDS will be used for the purpose. The CIFS survey using the CFHT will cover $\sim 5000 \text{ deg}^2$ with the r-band and $\sim 10000 \text{ deg}^2$ with the u-

¹² <https://www.euclid-ec.org/>

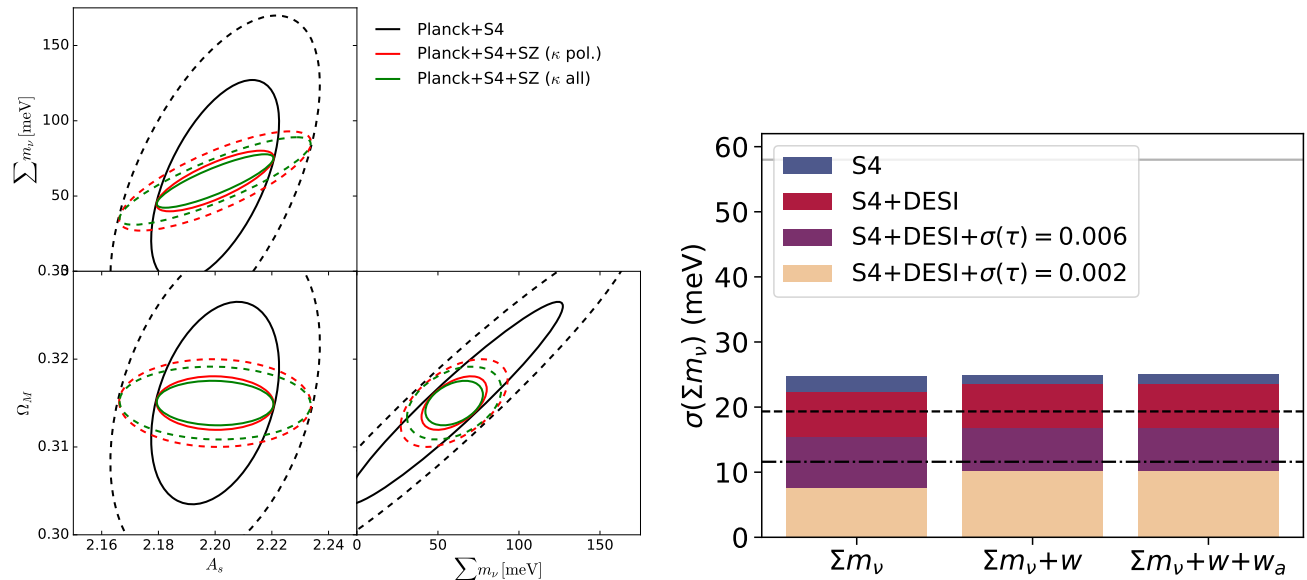


Fig. 21 *Left:* Uncertainties Ω_M , A_s and the sum of neutrino masses from an SZ catalogue carried out with CMB-S4 in combination with constraints from S4 primary and lensing power spectra, as well as *Planck* temperature and polarisation on $\ell < 30$. Results are shown in the absence of lensing mass estimates (black ellipses), and for lensing masses computed using only polarisation (red ellipses) and temperature and polarisation (green ellipses). The results are marginalised over all other cosmological parameters as well as the cluster nuisance parameters. Figure taken from [Louis & Alonso \(2017\)](#). *Right:* The $1 - \sigma$ uncertainty on neutrino mass obtained when marginalizing over ΛCDM , $\Lambda\text{CDM} + w_0$ and $\Lambda\text{CDM} + w_0 + w_a$, from tSZ clusters detected using a CMB Stage-4 telescope with 1' beam FWHM at 150 GHz. Constraints when the mass calibration is a combination of internal CMB and optical WL. Figure taken from [Madhavacheril et al. \(2017\)](#).

band by Jan. 31st 2020. The depth will be 24.1 mag and 23.6 mag, which is defined by 10σ aperture magnitudes for point sources within 2'' diameter, for the r-band and the u-band, respectively. The Javalambre-Euclid Deep Imaging Survey (JEDIS-g) using JST/T250 (Javalambre Suvery Telescope) will collect g-band data of ~ 5000 deg 2 of the northern sky in common with the CIFS survey.

In both Euclid and LSST, cluster mass measurements will be statistically and dramatically improved by the increase in the number of background galaxies. As a result, systematic biases on shape measurements and photometric redshifts will largely dominate over statistical errors. The main challenge for cluster mass measurements is control and minimisation of these systematic uncertainties. The resulting cosmological constraints from the cluster mass function will be complementary to cosmic-shear cosmology.

6.2.3 Simons Observatory and CMB-S4

The next decade of CMB survey instruments will continue to progress to large detector counts and additional bands from ~ 30 -300 GHz, promising to dramatically increase the statistical sample of SZ observations of galaxy clusters as well as facilitate the separation of the tSZ, kSZ and rSZ contributions in hundreds of high-mass systems¹³.

¹³ For more details, see the review by [Mroczkowski et al. 2018](#) in this volume.

Advanced ACTpol, which is the current generation instrument on ACT, and SPT-3G, the current generation camera on SPT, will also see some upgrades that will allow them to detect on the order of thousands of SZ selected clusters. Both are in the field and operating. SPT-3G for example is predicted to find ~ 5000 clusters at a signal-to-noise ≥ 4.5 ([Benson et al. 2014](#)). The ACT 6-meter will join the Simons Observatory, and both SPT and ACT will likely become part of CMB-S4.

The Simons Observatory¹⁴ (S.O.; [The Simons Observatory Collaboration 2018](#)) will combine several existing CMB experiments in the Atacama desert, and add a new 6-metre telescope with a similar optical design to CCAT-prime with an anticipated first light in 2021. Looking further ahead, CMB-S4¹⁵ will likely add up to three 6-metre antennas of similar design as the S.O. and CCAT-prime 6-m, and several more lower resolution 1-metre class antennas ([Abazajian et al. 2016](#)) with an anticipated first light in 2028.

S.O. and CMB-S4 will find on the order of 10^4 and 10^5 galaxy clusters respectively, including 10s to 1000s of high-z clusters ([Louis & Alonso 2017](#)), through the thermal SZ effect. Figure 21 shows that CMB-S4 will place competitive and independent constraints on cosmological parameters ([Louis & Alonso 2017](#)), including e.g. the sum of neutrino masses ([Madhavacheril et al. 2017](#)).

¹⁴ <https://simonsobservatory.org/>

¹⁵ <https://cmb-s4.org/>

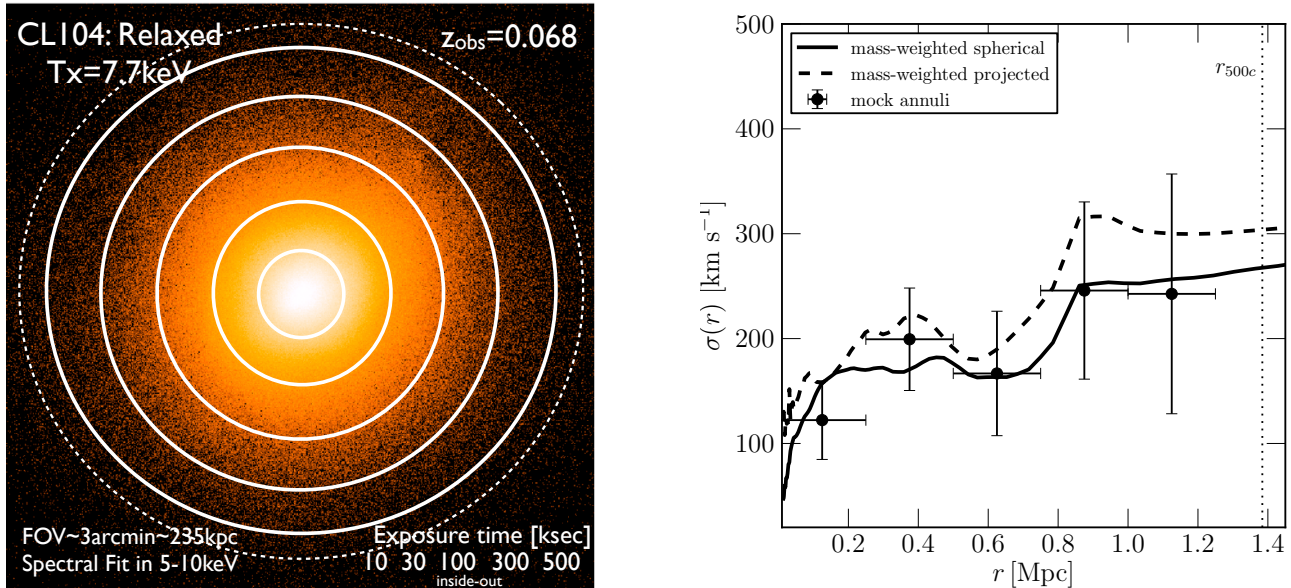


Fig. 22 Mock SXS / XRISM analysis of a relaxed galaxy cluster extracted from hydrodynamical simulations. *Left:* Mock XRISM image in a 5 – 10 keV band. The region shown is about 2.6 Mpc across, and the dotted circle indicates r_{500} . *Right panel:* XRISM/Resolve measurements of the gas velocity dispersion as a function of radius with 10, 30, 100, 300, 500 ksec exposures. The black lines represent the true mass-weighted 3-D (solid) and projected (dashed) gas velocity dispersion profiles. From Nagai et al. (2013).

6.2.4 XRISM and Athena

Gas motions in galaxy clusters play an important role in determining the properties of the ICM and in cosmological parameter estimation through X-ray and SZ effect observations of galaxy clusters. Recently, the Hitomi X-ray satellite has provided the first direct measurements of gas motions in the core of the Perseus Cluster (Hitomi Collaboration et al. 2016). Upcoming X-ray missions equipped with high-spectral resolution X-ray micro-calorimeters, such as XRISM and Athena, will continue Hitomi’s legacy by measuring ICM motions through Doppler shifting and broadening of emission lines in a larger number of galaxy clusters, and at larger radii.¹⁶

To assess the feasibility and future prospects of directly measuring the random and bulk gas motions at large cluster-centric radii in X-ray observations, Nagai et al. (2013) performed an analysis of mock *Hitomi* Soft X-ray Spectrometer (SXS; analogous to Resolve) spectra of a relaxed galaxy cluster extracted from cosmological numerical simulations, and find that a detailed characterization of the gas velocity profile out to beyond $r \approx R_{2500}$ will require of order 500 ksec of XRISM time, with a significant exposure spent on the outermost radial bins. However, if the significant investment of observing time is made, the gas velocity is recovered in good agreement with the 3D (deprojected) mass-weighted velocity

dispersion profile up to $r \approx R_{500}$ (see Figure 22) and enables us to correct for the hydrostatic mass bias of galaxy clusters. On the other hand, perhaps counterintuitively at first, the XRISM mock measurement is slightly ($\sim 30 - 50$ km s⁻¹) smaller than the *projected* mass-weighted gas velocity dispersion in a given radial bin, although the mock observations should probe the integrated motions along the line-of-sight. This difference occurs because the measured velocity is spectral-weighted, and hence the inner regions where the gas density is higher but the gas velocity is smaller carry a higher weight. Also, Ota et al. (2018) showed that XRISM is capable of measuring non-thermal pressure provided by bulk and random motions and correcting for the hydrostatic mass bias. Going forward, this synergy between numerical simulations, mock observations, and real data will need to be employed frequently in order to correctly interpret the measurements and uncover any potential biases or significant projection effects.

Some details of the upcoming missions include the following.

- The X-Ray Imaging and Spectroscopy Mission (XRISM), formerly XARM (the X-ray Astronomy Recovery Mission, Tashiro et al. 2018) is planned as a successor of the Hitomi satellite, and will carry a high spectral resolution X-ray microcalorimeter (Resolve), which is identical to the SXS.
- Athena¹⁷ (Nandra et al. 2013) is ESA’s second Large Mission after the planetary mission Juice, and before

¹⁶ Measurements will also be possible in the outskirts of high-redshift clusters using high-resolution SZ spectral imaging observations through tSZ pressure fluctuations and direct kSZ measurements of internal gas motions (see the review by Mroczkowski et al. 2018, in this volume).

¹⁷ <https://www.the-athena-x-ray-observatory.eu/>

the gravitational wave mission LISA. Details of cluster science expectations are provided in Pointecouteau et al. (2013); Ettori et al. (2013b); Croston et al. (2013). The expected launch is in the early 2030s. The major increase in collecting area together with the superb spectral resolution of the micro-calorimeter instrument (X-IFU) will allow us to map turbulence and bulk motions in the inner regions (Roncarelli et al. 2018). Together with measurements of these quantities in the outer parts of clusters, it is expected that we will be able to set tight limits on hydrostatic mass bias from non-thermal pressure support resulting from gas velocities. Furthermore, the wide field-of-view of the active pixel sensor (WFI) results in outstanding cluster survey capabilities.

6.2.5 Studies

X-ray satellite missions under study which would have an impact on cluster science include:

- AXIS, the Advanced X-ray Imaging Satellite¹⁸ (Mushotzky 2018), is a Probe-class mission under study for the 2020 Decadal. The concept combines $\sim 0.4''$ imaging across a $24' \times 24'$ field of view, with CCD-type spectral resolution.
- Lynx¹⁹ (The Lynx Team 2018) is a flagship mission concept under study for the 2020 NASA Decadal, for launch around the middle of the 2030s. A large collecting area ($\sim 2 \text{ m}^2$ at 1 keV), high resolution ($\lesssim 1''$) imaging, and high-resolution spectroscopy ($\lesssim 2 \text{ eV}$), combined with survey capability at CCD-type spectral resolution, will push spatially-resolved measurements of clusters and proto-clusters out to $z \sim 3$.

7 Summary

Galaxy cluster mass measurements are fundamental to our understanding of structure formation, and to the use of the cluster population and its evolution to constrain cosmological parameters. As illustrated in this review, there are a number of different methods with which to measure the mass of galaxy clusters, making use of galaxy velocity dispersions, WL, X-ray, and X-ray/SZ observations. In recent years, great progress has been made in all of these methods. Better observations have allowed more precise masses to be obtained; larger samples have allowed statistical analysis; inter-comparison between methods has enabled us to better understand systematic effects. A large parallel effort has been undertaken by the theoretical community, using numerical simulations to explore the assumptions and biases inherent in each mass estimation method.

¹⁸ <http://axis.astro.umd.edu/>

¹⁹ <https://www.lynxobservatory.com/>

In individual systems, mass profile measurements from *all* methods now indicate no significant deviation from the cusped dark matter profile shape predicted from numerical simulations, from local systems up to the most distant observations currently possible, at $z \sim 1$. Furthermore, the systematic effects inherent in each method are now well-identified: lack of dynamical equilibrium and triaxiality in optical; the hydrostatic bias in X-rays; the purity of background catalogues and triaxiality in lensing.

A fully consistent picture of the mass of galaxy clusters is necessary for both understanding their formation and evolution, and for their use as cosmological probes. Critically, the methods are fully independent, so that inter-comparison of their results can help to better understand the assumptions and biases inherent in each one. Further progress will require mass measurements of a large sample of clusters, selected in as unbiased a manner as possible, using all available methods. Extension to lower masses is also necessary, both to better understand cluster formation and evolution, and also to exploit the rich data sets that will be available from new surveys in optical (HSC, LSST, DES, Euclid), X-ray (*e*ROSITA), and SZ (Simons Observatory, CMB-S4). The combination of methods, such as using X-ray and SZ observations of similar angular resolution, will allow extension of mass measurements to higher redshifts. In the future, measurement of bulk motions and turbulence in the inner regions of nearby systems will be possible with XRISM and Athena, and in the outskirts and in high-redshift systems with high-resolution SZ imaging.

These new surveys in optical, X-ray, SZ, and lensing will yield new samples and allow us to probe selection effects and reveal the properties of the true underlying population. Further progress is expected given the wealth of current and forthcoming data.

Acknowledgements This work was initiated during a visit to the International Space Science Institute (ISSI) in Bern and we acknowledge ISSIs hospitality. GWP and MA acknowledge funding from the European Research Council under the European Union’s Seventh Framework Programme (FP7/2007-2013)/ERC grant agreement No. 340519. SE acknowledges financial contribution from the contracts NARO15 ASI-INAF I/037/12/0, ASI 2015-046-R.0, ASI-INAF n.2017-14-H.0 and funding from the European Union’s Horizon 2020 Programme under the AHEAD project (grant agreement n. 654215). DN acknowledges Yale University for granting a triennial leave and the Max-Planck-Institut für Astrophysik for hospitality when this work was carried out. THR acknowledges support from the German Aerospace Agency (DLR) with funds from the Ministry of Economy and Technology (BMWi) through grant 50 OR 1514.

References

- Abazajian, K. N., Adshead, P., Ahmed, Z., et al. 2016, ArXiv e-prints
 Abbott, T. M. C., Abdalla, F. B., Alarcon, A., et al. 2018, Phys. Rev. D, 98, 043526
 Adam, R., Comis, B., Bartalucci, I., et al. 2016, A&A, 586, A122

- Adam, R., Arnaud, M., Bartalucci, I., et al. 2017, *A&A*, 606, A64
- Aihara, H., Armstrong, R., Bickerton, S., et al. 2018a, *PASJ*, 70, S8
- Aihara, H., Arimoto, N., Armstrong, R., et al. 2018b, *PASJ*, 70, S4
- Allen, S. W., Evrard, A. E., & Mantz, A. B. 2011, *ARA&A*, 49, 409
- Allen, S. W., Rapetti, D. A., Schmidt, R. W., et al. 2008, *MNRAS*, 383, 879
- Allgood, B., Flores, R. A., Primack, J. R., et al. 2006, *MNRAS*, 367, 1781
- Ameglio, S., Borgani, S., Pierpaoli, E., & Dolag, K. 2007, *MNRAS*, 382, 397
- Ameglio, S., Borgani, S., Pierpaoli, E., et al. 2009, *MNRAS*, 394, 479
- Amodeo, S., Ettori, S., Capasso, R., & Sereno, M. 2016, *A&A*, 590, A126
- Anders, E., & Grevesse, N. 1989, *Geochim. Cosmochim. Acta*, 53, 197
- Andrade-Santos, F., Jones, C., Forman, W. R., et al. 2017, *ApJ*, 843, 76
- Applegate, D. E., von der Linden, A., Kelly, P. L., et al. 2014, *MNRAS*, 439, 48
- Applegate, D. E., Mantz, A., Allen, S. W., et al. 2016, *MNRAS*, 457, 1522
- Arnaud, M. 2017, *Astronomische Nachrichten*, 338, 342
- Arnaud, M., Pointecouteau, E., & Pratt, G. W. 2007, *A&A*, 474, L37
- Arnaud, M., Pratt, G. W., Piffaretti, R., et al. 2010, *A&A*, 517, A92
- Arnouts, S., Cristiani, S., Moscardini, L., et al. 1999, *MNRAS*, 310, 540
- Balestra, I., Mercurio, A., Sartoris, B., et al. 2016, *ApJS*, 224, 33
- Balmès, I., Rasera, Y., Corasaniti, P.-S., & Alimi, J.-M. 2014, *MNRAS*, 437, 2328
- Barnes, D. J., Kay, S. T., Bahé, Y. M., et al. 2017, *MNRAS*, 471, 1088
- Barnes, D. J., Vogelsberger, M., Kannan, R., et al. 2018, *MNRAS*
- Bartalucci, I., Arnaud, M., Pratt, G. W., & Le Brun, A. M. C. 2018, *A&A*, 617, A64
- Bartalucci, I., Arnaud, M., Pratt, G. W., et al. 2017, *A&A*, 608, A88
- Bartelmann, M. 1996, *A&A*, 313, 697
- Bartelmann, M., & Schneider, P. 2001, *Phys. Rep.*, 340, 291
- Basu, K., Zhang, Y.-Y., Sommer, M. W., et al. 2010, *A&A*, 519, A29
- Battaglia, G., Helmi, A., Tolstoy, E., et al. 2008, *ApJ*, 681, L13
- Battaglia, N., Bond, J. R., Pfrommer, C., & Sievers, J. L. 2012, *ApJ*, 758, 74
- Baxter, E. J., Raghunathan, S., Crawford, T. M., et al. 2018, *MNRAS*, 476, 2674
- Becker, M. R., & Kravtsov, A. V. 2011, *ApJ*, 740, 25
- Bellagamba, F., Sereno, M., Roncarelli, M., et al. 2019, *MNRAS*, 484, 1598
- Benson, B. A., Ade, P. A. R., Ahmed, Z., et al. 2014, in Proc. SPIE, Vol. 9153, Millimeter, Submillimeter, and Far-Infrared Detectors and Instrumentation for Astronomy VII, 91531P
- Bernstein, G. M., & Jarvis, M. 2002, *AJ*, 123, 583
- Bett, P., Eke, V., Frenk, C. S., et al. 2007, *MNRAS*, 376, 215
- Bhattacharya, S., Habib, S., Heitmann, K., & Vikhlinin, A. 2013, *ApJ*, 766, 32
- Biffi, V., Borgani, S., Murante, G., et al. 2016, *ApJ*, 827, 112
- Bilicki, M., Hoekstra, H., Brown, M. J. I., et al. 2017, ArXiv e-prints, arxiv:1709.04205
- Binney, J., & Mamon, G. A. 1982, *MNRAS*, 200, 361
- Binney, J., & Tremaine, S. 1987, *Galactic dynamics* (Princeton, NJ, Princeton University Press, 1987, 747 p.)
- Biviano, A., & Girardi, M. 2003, *ApJ*, 585, 205
- Biviano, A., Murante, G., Borgani, S., et al. 2006, *A&A*, 456, 23
- Biviano, A., & Poggianti, B. M. 2009, *A&A*, 501, 419
- Biviano, A., Popesso, P., Dietrich, J. P., et al. 2017a, *A&A*, 602, A20
- Biviano, A., van der Burg, R. F. J., Muzzin, A., et al. 2016, *A&A*, 594, A51
- Biviano, A., Rosati, P., Balestra, I., et al. 2013, *A&A*, 558, A1
- Biviano, A., Moretti, A., Paccagnella, A., et al. 2017b, *A&A*, 607, A81
- Bleem, L. E., Stalder, B., de Haan, T., et al. 2015, *ApJS*, 216, 27
- Blumenthal, G. R., Faber, S. M., Flores, R., & Primack, J. R. 1986, *ApJ*, 301, 27
- Bocquet, S., Saro, A., Mohr, J. J., et al. 2015, *ApJ*, 799, 214
- Bocquet, S., Dietrich, J. P., Schrabback, T., et al. 2018, *ApJ*, submitted. Pre-print: arXiv:1812.01679, arXiv:1812.01679
- Böhringer, H., Chon, G., & Collins, C. A. 2014, *A&A*, 570, A31
- Böhringer, H., Chon, G., & Fukugita, M. 2017a, *A&A*, 608, A65
- Böhringer, H., Chon, G., Retzlaff, J., et al. 2017b, *AJ*, 153, 220
- Borgani, S., Rosati, P., Tozzi, P., et al. 2001, *ApJ*, 561, 13
- Borm, K., Reiprich, T. H., Mohammed, I., & Lovisari, L. 2014, *A&A*, 567, A65
- Bourdin, H., Mazzotta, P., Kozmanyan, A., Jones, C., & Vikhlinin, A. 2017, *ApJ*, 843, 72
- Bridle, S., Balan, S. T., Bethge, M., et al. 2010, *MNRAS*, 405, 2044
- Broadhurst, T., Takada, M., Umetsu, K., et al. 2005, *ApJ*, 619, L143
- Broadhurst, T. J., Taylor, A. N., & Peacock, J. A. 1995, *ApJ*, 438, 49
- Bulbul, E., Chiu, I., Mohr, J. J., et al. 2018, *ApJ*, accepted. Pre-print: arXiv:1807.02556
- Bullock, J. S., Kolatt, T. S., Sigad, Y., et al. 2001, *MNRAS*, 321, 559
- Buote, D. A., Gastaldello, F., Humphrey, P. J., et al. 2007, *ApJ*, 664, 123
- Buote, D. A., & Humphrey, P. J. 2012, *MNRAS*, 421, 1399
- Buote, D. A., & Lewis, A. D. 2004, *ApJ*, 604, 116
- Carlberg, R. G., Yee, H. K. C., & Ellingson, E. 1997, *ApJ*, 478, 462
- Carrasco Kind, M., & Brunner, R. J. 2014, *MNRAS*, 438, 3409
- Chiu, I., Mohr, J. J., McDonald, M., et al. 2017, *MNRAS*, submitted
- Chiu, I.-N., Umetsu, K., Sereno, M., et al. 2018, *ApJ*, 860, 126
- Cibirka, N., Cypriano, E. S., Brimiouille, F., et al. 2017, *MNRAS*, 468, 1092
- Clerc, N., Sadibekova, T., Pierre, M., et al. 2012, *MNRAS*, 423, 3561
- Clerc, N., Ramos-Ceja, M. E., Ridl, J., et al. 2018, *A&A*, 617, A92
- Collister, A. A., & Lahav, O. 2004, *PASP*, 116, 345
- Corasaniti, P. S., Ettori, S., Rasera, Y., et al. 2018, *ApJ*, 862, 40
- Corless, V. L., King, L. J., & Clowe, D. 2009, *MNRAS*, 393, 1235
- Costanzi, M., Rozo, E., Simet, M., et al. 2018, Pre-print: arXiv:1810.09456
- Coupon, J., Arnouts, S., van Waerbeke, L., et al. 2015, *MNRAS*, 449, 1352
- Croston, J. H., Sanders, J. S., Heinz, S., et al. 2013, *Athena Supporting Paper*, arXiv:1306.2323, arXiv:1306.2323
- Cui, W., Knebe, A., Yepes, G., et al. 2018, *MNRAS*, 480, 2898
- da Silva, A. C., Kay, S. T., Liddle, A. R., & Thomas, P. A. 2004, *MNRAS*, 348, 1401
- Dark Energy Survey Collaboration, Abbott, T., Abdalla, F. B., et al. 2016a, *MNRAS*, 460, 1270
- . 2016b, *MNRAS*, 460, 1270
- De Filippis, E., Sereno, M., Bautz, M. W., & Longo, G. 2005, *ApJ*, 625, 108
- de Haan, T., Benson, B. A., Bleem, L. E., et al. 2016, *ApJ*, 832, 95
- de Jong, J. T. A., Verdoes Kleijn, G. A., Boxhoorn, D. R., et al. 2015, *A&A*, 582, A62
- Dejonghe, H., & Merritt, D. 1992, *ApJ*, 391, 531
- Diaferio, A. 1999, *MNRAS*, 309, 610
- Diaferio, A., & Geller, M. J. 1997, *ApJ*, 481, 633
- Diemer, B., & Kravtsov, A. V. 2014, *ApJ*, 789, 1
- . 2015, *ApJ*, 799, 108
- Dolag, K., Bartelmann, M., Perrotta, F., et al. 2004, *A&A*, 416, 853
- Donahue, M., Voit, G. M., Mahdavi, A., et al. 2014, *ApJ*, 794, 136
- Duffy, A. R., Schaye, J., Kay, S. T., & Dalla Vecchia, C. 2008, *MNRAS*, 390, L64
- Durret, F., Wakamatsu, K., Nagayama, T., Adam, C., & Biviano, A. 2015, *A&A*, 583, A124
- Dutton, A. A., & Macciò, A. V. 2014, *MNRAS*, 441, 3359
- Eckert, D., Roncarelli, M., Ettori, S., et al. 2015, *MNRAS*, 447, 2198
- Eckert, D., Ettori, S., Coupon, J., et al. 2016, *A&A*, 592, A12
- Eckert, D., Ghirardini, V., Ettori, S., et al. 2019, *A&A*, 621, A40
- Eggen, O. J., Lynden-Bell, D., & Sandage, A. R. 1962, *ApJ*, 136, 748

- Einasto, J. 1965, Trudy Astrofizicheskogo Instituta Alma-Ata, 5, 87
- Eisenstein, D. J., & Hu, W. 1998, ApJ, 496, 605
- Ettori, S., Donnarumma, A., Pointecouteau, E., et al. 2013a, Space Sci. Rev., 177, 119
- Ettori, S., Gastaldello, F., Leccardi, A., et al. 2010, A&A, 524, A68
- Ettori, S., Morandi, A., Tozzi, P., et al. 2009, A&A, 501, 61
- Ettori, S., Pratt, G. W., de Plaa, J., et al. 2013b, Athena Supporting Paper, arXiv:1306.2322
- Ettori, S., Ghirardini, V., Eckert, D., et al. 2019, A&A, 621, A39
- Evans, A. E. 1997, MNRAS, 292, 289
- Evans, A. E., Bialek, J., Busha, M., et al. 2008, ApJ, 672, 122
- Fadda, D., Girardi, M., Giuricin, G., Mardirossian, F., & Mezzetti, M. 1996, ApJ, 473, 670
- Gao, L., De Lucia, G., White, S. D. M., & Jenkins, A. 2004, MNRAS, 352, L1
- Gao, L., Navarro, J. F., Cole, S., et al. 2008, MNRAS, 387, 536
- Gao, L., Navarro, J. F., Frenk, C. S., et al. 2012, MNRAS, 425, 2169
- Gastaldello, F., Buote, D. A., Humphrey, P. J., et al. 2007, ApJ, 669, 158
- Geller, M. J., Hwang, H. S., Diaferio, A., et al. 2014, ApJ, 783, 52
- Ghirardini, V., Ettori, S., Eckert, D., et al. 2018, A&A, 614, A7
- Ghirardini, V., Eckert, D., Ettori, S., et al. 2019, A&A, 621, A41
- Gifford, D., Miller, C., & Kern, N. 2013, ApJ, 773, 116
- Giles, P. A., Maughan, B. J., Dahle, H., et al. 2017, MNRAS, 465, 858
- Giordani, S., Lovisari, L., Pointecouteau, E., et al. 2013, Space Sci. Rev., 177, 247
- Gnedin, O. Y., Kravtsov, A. V., Klypin, A. A., & Nagai, D. 2004, ApJ, 616, 16
- Gonzalez, A. H., Sivanandam, S., Zabludoff, A. I., & Zaritsky, D. 2013, ApJ, 778, 14
- Gonzalez, A. H., Zaritsky, D., & Zabludoff, A. I. 2007, ApJ, 666, 147
- Gottlöber, S., & Yepes, G. 2007, ApJ, 664, 117
- Grandis, S., Mohr, J. J., Dietrich, J. P., et al. 2018, arXiv:1810.10553
- Groener, A. M., Goldberg, D. M., & Sereno, M. 2016, MNRAS, 455, 892
- Gruen, D., Seitz, S., Becker, M. R., Friedrich, O., & Mana, A. 2015, MNRAS, 449, 4264
- Guennou, L., Biviano, A., Adami, C., et al. 2014, A&A, 566, A149
- Hahn, O., Martizzi, D., Wu, H.-Y., et al. 2017, MNRAS, 470, 166
- Hamana, T., Miyazaki, S., Okura, Y., Okamura, T., & Futamase, T. 2013, PASJ, 65, 104
- Hasselfield, M., Hilton, M., Marriage, T. A., et al. 2013, J. Cosmology Astropart. Phys., 7, 008
- Heymans, C., Van Waerbeke, L., Bacon, D., et al. 2006, MNRAS, 368, 1323
- Heymans, C., Van Waerbeke, L., Miller, L., et al. 2012, MNRAS, 427, 146
- Hikage, C., Oguri, M., Hamana, T., et al. 2018, PASJ, submitted. Preprint: arXiv:1809.09148
- Hildebrandt, H., Viola, M., Heymans, C., et al. 2017, MNRAS, 465, 1454
- Hildebrandt, H., Köhlinger, F., van den Busch, J. L., et al. 2018, A&A, submitted. Preprint: arXiv:1812.06076
- Hinshaw, G., Larson, D., Komatsu, E., et al. 2013, ApJS, 208, 19
- Hirata, C., & Seljak, U. 2003, MNRAS, 343, 459
- Hitomi Collaboration, Aharonian, F., Akamatsu, H., et al. 2016, Nature, 535, 117
- . 2018, PASJ, 70, 11
- Hoekstra, H. 2003, MNRAS, 339, 1155
- Hoekstra, H., Herbonnet, R., Muzzin, A., et al. 2015a, MNRAS, 449, 685
- . 2015b, MNRAS, 449, 685
- Hoekstra, H., Mahdavi, A., Babul, A., & Bildfell, C. 2012, MNRAS, 427, 1298
- Hofmann, F., Sanders, J. S., Clerc, N., et al. 2017, A&A, 606, A118
- Hopkins, P. F., Bahcall, N. A., & Bode, P. 2005, ApJ, 618, 1
- Hoyle, B., Gruen, D., Bernstein, G. M., et al. 2018, MNRAS, 478, 592
- Hwang, H. S., & Lee, M. G. 2007, ApJ, 662, 236
- Ichikawa, K., Matsushita, K., Okabe, N., et al. 2013, ApJ, 766, 90
- Ilbert, O., Arnouts, S., McCracken, H. J., et al. 2006, A&A, 457, 841
- Ilbert, O., McCracken, H. J., Le Fèvre, O., et al. 2013, A&A, 556, A55
- Ivezic, Z., Tyson, J. A., Abel, B., et al. 2008, ArXiv e-prints
- Ivezic, Ž., Kahn, S. M., Tyson, J. A., et al. 2008, arXiv:0805.2366
- Jarvis, M., Sheldon, E., Zuntz, J., et al. 2016, MNRAS, 460, 2245
- Jenkins, A., Frenk, C. S., White, S. D. M., et al. 2001, MNRAS, 321, 372
- Jing, Y. P. 2000, ApJ, 535, 30
- Jing, Y. P., & Suto, Y. 2002, ApJ, 574, 538
- Kaiser, N., Squires, G., & Broadhurst, T. 1995, ApJ, 449, 460
- Kasun, S. F., & Evans, A. E. 2005, ApJ, 629, 781
- Katgert, P., Biviano, A., & Mazure, A. 2004, ApJ, 600, 657
- Kawaharada, M., Okabe, N., Umetsu, K., et al. 2010, ApJ, 714, 423
- Kazantzidis, S., Kravtsov, A. V., Zentner, A. R., et al. 2004, ApJ, 611, L73
- Kelly, P. L., von der Linden, A., Applegate, D. E., et al. 2014, MNRAS, 439, 28
- Kitching, T. D., Miller, L., Heymans, C. E., van Waerbeke, L., & Heavens, A. F. 2008, MNRAS, 390, 149
- Kitching, T. D., Balan, S. T., Bridle, S., et al. 2012, MNRAS, 423, 3163
- Kitching, T. D., Rowe, B., Gill, M., et al. 2013, ApJS, 205, 12
- Klypin, A. A., Trujillo-Gomez, S., & Primack, J. 2011, ApJ, 740, 102
- Kravtsov, A. V., & Borgani, S. 2012, ARA&A, 50, 353
- Kravtsov, A. V., Nagai, D., & Vikhlinin, A. A. 2005, ApJ, 625, 588
- Kravtsov, A. V., Vikhlinin, A., & Nagai, D. 2006, ApJ, 650, 128
- Kuijken, K., Heymans, C., Hildebrandt, H., et al. 2015, MNRAS, 454, 3500
- Laganá, T. F., Martinet, N., Durret, F., et al. 2013, A&A, 555, A66
- LaRoque, S. J., Bonamente, M., Carlstrom, J. E., et al. 2006, ApJ, 652, 917
- Lau, E. T., Kravtsov, A. V., & Nagai, D. 2009, ApJ, 705, 1129
- Lau, E. T., Nagai, D., & Kravtsov, A. V. 2010, ApJ, 708, 1419
- Lau, E. T., Nagai, D., Kravtsov, A. V., & Zentner, A. R. 2011, ApJ, 734, 93
- Lau, E. T., Nagai, D., & Nelson, K. 2013, ApJ, 777, 151
- Laureijs, R., Amiaux, J., Arduini, S., et al. 2011, arXiv:1110.3193
- Le Brun, A. M. C., McCarthy, I. G., Schaye, J., & Ponman, T. J. 2014, MNRAS, 441, 1270
- . 2017, MNRAS, 466, 4442
- Leauthaud, A., Tinker, J., Bundy, K., et al. 2012, ApJ, 744, 159
- Lemze, D., Broadhurst, T., Rephaeli, Y., Barkana, R., & Umetsu, K. 2009, ApJ, 701, 1336
- Limousin, M., Morandi, A., Sereno, M., et al. 2013, Space Sci. Rev., 177, 155
- Lokas, E. L. 2002, MNRAS, 333, 697
- Lokas, E. L., & Mamon, G. A. 2003, MNRAS, 343, 401
- Louis, T., & Alonso, D. 2017, Phys. Rev. D, 95, 043517
- Lovell, M. R., Pillepich, A., Genel, S., et al. 2018, MNRAS
- Lovisari, L., Forman, W. R., Jones, C., et al. 2017, ApJ, 846, 51
- Ludlow, A. D., Navarro, J. F., Angulo, R. E., et al. 2014, MNRAS, 441, 378
- Macciò, A. V., Dutton, A. A., & van den Bosch, F. C. 2008, MNRAS, 391, 1940
- Madhavarachil, M. S., Battaglia, N., & Miyatake, H. 2017, Phys. Rev. D, 96, 103525
- Mahdavi, A., Hoekstra, H., Babul, A., et al. 2013, ApJ, 767, 116
- Mamon, G. A., Biviano, A., & Boué, G. 2013, MNRAS, 429, 3079
- Mamon, G. A., Biviano, A., & Murante, G. 2010, A&A, 520, A30
- Mamon, G. A., & Boué, G. 2010, MNRAS, 401, 2433
- Mandelbaum, R., Rowe, B., Armstrong, R., et al. 2015, MNRAS, 450, 2963
- Mandelbaum, R., Lanusse, F., Leauthaud, A., et al. 2017, ArXiv e-prints
- Mandelbaum, R., Miyatake, H., Hamana, T., et al. 2018, PASJ, 70, S25

- Mantz, A., Allen, S. W., Ebeling, H., Rapetti, D., & Drlica-Wagner, A. 2010a, MNRAS, 406, 1773
- Mantz, A., Allen, S. W., Rapetti, D., & Ebeling, H. 2010b, MNRAS, 406, 1759
- . 2010c, MNRAS, 406, 1759
- Mantz, A. B., Allen, S. W., & Morris, R. G. 2016a, MNRAS, 462, 681
- . 2016b, MNRAS, 462, 681
- Mantz, A. B., Allen, S. W., Morris, R. G., et al. 2014a, MNRAS, 440, 2077
- . 2014b, MNRAS, 440, 2077
- Mantz, A. B., Allen, S. W., Morris, R. G., & von der Linden, A. 2018, MNRAS, 473, 3072
- Mantz, A. B., von der Linden, A., Allen, S. W., et al. 2015, MNRAS, 446, 2205
- Marriage, T. A., Acquaviva, V., Ade, P. A. R., et al. 2011, ApJ, 737, 61
- Martino, R., Mazzotta, P., Bourdin, H., et al. 2014, MNRAS, 443, 2342
- Massey, R., Heymans, C., Bergé, J., et al. 2007, MNRAS, 376, 13
- Mathiesen, B., Evrard, A. E., & Mohr, J. J. 1999, ApJ, 520, L21
- Maughan, B. J. 2007, ApJ, 668, 772
- Maughan, B. J., Giles, P. A., Rines, K. J., et al. 2016, MNRAS, 461, 4182
- Mazzotta, P., Rasia, E., Moscardini, L., & Tormen, G. 2004, MNRAS, 354, 10
- McCarthy, I. G., Schaye, J., Bird, S., & Le Brun, A. M. C. 2017, MNRAS, 465, 2936
- McNamara, B. R., & Nulsen, P. E. J. 2007, ARA&A, 45, 117
- Medezinski, E., Broadhurst, T., Umetsu, K., et al. 2010, MNRAS, 405, 257
- Medezinski, E., Oguri, M., Nishizawa, A. J., et al. 2017, ArXiv 1706.00427
- . 2018, PASJ
- Mehrtens, N., Romer, A. K., Hilton, M., et al. 2012, MNRAS, 423, 1024
- Melchior, P., Gruen, D., McClintock, T., et al. 2017, MNRAS, 469, 4899
- Melin, J.-B., & Bartlett, J. G. 2015, A&A, 578, A21
- Menanteau, F., Sifón, C., Barrientos, L. F., et al. 2013, ApJ, 765, 67
- Meneghetti, M., Rasia, E., Merten, J., et al. 2010, A&A, 514, A93
- Meneghetti, M., Rasia, E., Vega, J., et al. 2014, ApJ, 797, 34
- Merloni, A., Predehl, P., Becker, W., et al. 2012, arXiv:1209.3114
- Merritt, D. 1987, ApJ, 313, 121
- Merten, J., Meneghetti, M., Postman, M., et al. 2014, ArXiv e-prints —. 2015, ApJ, 806, 4
- Miller, L., Heymans, C., Kitching, T. D., et al. 2013, MNRAS, 429, 2858
- Miyatake, H., Battaglia, N., Hilton, M., et al. 2018, arXiv:1804.05873
- Miyazaki, S., Oguri, M., Hamana, T., et al. 2018a, PASJ, 70, S27
- Miyazaki, S., Komiyama, Y., Kawanomoto, S., et al. 2018b, PASJ, 70, S1
- Morandi, A., & Cui, W. 2013, ArXiv e-prints
- Morandi, A., Nagai, D., & Cui, W. 2013, MNRAS, 436, 1123
- Motl, P. M., Hallman, E. J., Burns, J. O., & Norman, M. L. 2005, ApJ, 623, L63
- Mroczkowski, T., Bonamente, M., Carlstrom, J. E., et al. 2009, ApJ, 694, 1034
- Mroczkowski, T., Nagai, D., Basu, K., et al. 2018, arXiv e-prints, arXiv:1811.02310
- Munari, E., Biviano, A., Borgani, S., Murante, G., & Fabjan, D. 2013, MNRAS, 430, 2638
- Munari, E., Biviano, A., & Mamon, G. A. 2014, A&A, 566, A68
- Mushotzky, R. 2018, in Society of Photo-Optical Instrumentation Engineers (SPIE) Conference Series, Vol. 10699, Space Telescopes and Instrumentation 2018: Ultraviolet to Gamma Ray, 1069929
- Nagai, D., & Lau, E. T. 2011, ApJ, 731, L10+
- Nagai, D., Lau, E. T., Avestruz, C., Nelson, K., & Rudd, D. H. 2013, ApJ, 777, 137
- Nagai, D., Vikhlinin, A., & Kravtsov, A. V. 2007, ApJ, 655, 98
- Nandra, K., Barret, D., Barcons, X., et al. 2013, arXiv:1306.2307
- Navarro, J. F., Frenk, C. S., & White, S. D. M. 1996, ApJ, 462, 563
- . 1997, ApJ, 490, 493
- Navarro, J. F., Hayashi, E., Power, C., et al. 2004, MNRAS, 349, 1039
- Nelson, K., Lau, E. T., & Nagai, D. 2014a, ApJ, 792, 25
- Nelson, K., Lau, E. T., Nagai, D., Rudd, D. H., & Yu, L. 2014b, ApJ, 782, 107
- Nelson, K., Rudd, D. H., Shaw, L., & Nagai, D. 2012, ApJ, 751, 121
- Neto, A. F., Gao, L., Bett, P., et al. 2007, MNRAS, 381, 1450
- Nevalainen, J., David, L., & Guainazzi, M. 2010, A&A, 523, A22
- Ntampaka, M., Trac, H., Sutherland, D. J., et al. 2015, ApJ, 803, 50
- Oguri, M. 2014, MNRAS, 444, 147
- Oguri, M., Bayliss, M. B., Dahle, H., et al. 2012, MNRAS, 420, 3213
- Oguri, M., & Hamana, T. 2011, MNRAS, 414, 1851
- Oguri, M., & Keeton, C. R. 2004, ApJ, 610, 663
- Oguri, M., & Takada, M. 2011, Phys. Rev. D, 83, 023008
- Oguri, M., Takada, M., Umetsu, K., & Broadhurst, T. 2005, ApJ, 632, 841
- Oguri, M., Miyazaki, S., Hikage, C., et al. 2018, PASJ, 70, S26
- Okabe, N., Futamase, T., Kajisawa, M., & Kuroshima, R. 2014, ApJ, 784, 90
- Okabe, N., & Smith, G. P. 2016, MNRAS, 461, 3794
- Okabe, N., Smith, G. P., Umetsu, K., Takada, M., & Futamase, T. 2013, ApJ, 769, L35
- Okabe, N., Takada, M., Umetsu, K., Futamase, T., & Smith, G. P. 2010, PASJ, 62, 811
- Okabe, N., & Umetsu, K. 2008, PASJ, 60, 345
- Okabe, N., Umetsu, K., Tamura, T., et al. 2016, MNRAS, 456, 4475
- Okura, Y., & Futamase, T. 2018, ArXiv e-prints
- Ota, N., Nagai, D., & Lau, E. T. 2018, PASJ, 70, 51
- Pacaud, F., Clerc, N., Giles, P. A., et al. 2016, A&A, 592, A2
- Pacaud, F., Pierre, M., Melin, J.-B., et al. 2018, A&A, 620, A10
- Pike, S. R., Kay, S. T., Newton, R. D. A., Thomas, P. A., & Jenkins, A. 2014, MNRAS, 445, 1774
- Pillepich, A., Porciani, C., & Reiprich, T. H. 2012, MNRAS, 422, 44
- Pillepich, A., Reiprich, T. H., Porciani, C., Borm, K., & Merloni, A. 2018, MNRAS, 481, 613
- Pizzuti, L., Sartoris, B., Borgani, S., et al. 2016, J. Cosmology Astropart. Phys., 4, 023
- Pizzuti, L., Sartoris, B., Amendola, L., et al. 2017, J. Cosmology Astropart. Phys., 7, 023
- Planck Collaboration Int. III. 2013, A&A, 550, A129
- Planck Collaboration Int. V. 2013, A&A, 550, A131
- Planck Collaboration VI. 2018, arXiv:1807.06209v1
- Planck Collaboration VIII. 2011, A&A, 536, A8
- Planck Collaboration XI. 2011, A&A, 536, A11
- Planck Collaboration XIII. 2016, A&A, 594, A13
- Planck Collaboration XX. 2014, A&A, 571, A20
- Planck Collaboration XXIV. 2016, A&A, 594, A24
- Planck Collaboration XXIX. 2014, A&A, 571, A29
- Planck Collaboration XXVII. 2016, A&A, 594, A27
- Planelles, S., Borgani, S., Dolag, K., et al. 2013, MNRAS, 431, 1487
- Planelles, S., Borgani, S., Fabjan, D., et al. 2014, MNRAS, 438, 195
- Planelles, S., Schleicher, D. R. G., & Bykov, A. M. 2015, Space Sci. Rev., 188, 93
- Planelles, S., Fabjan, D., Borgani, S., et al. 2017, MNRAS, 467, 3827
- Pointecouteau, E., Arnaud, M., & Pratt, G. W. 2005, A&A, 435, 1
- Pointecouteau, E., Reiprich, T. H., Adami, C., et al. 2013, Athena Supporting Paper, arXiv:1306.2319
- Poole, G. B., Babul, A., McCarthy, I. G., et al. 2007, MNRAS, 380, 437
- Pratt, G. W., & Arnaud, M. 2002, A&A, 394, 375
- Pratt, G. W., Croston, J. H., Arnaud, M., & Böhringer, H. 2009, A&A, 498, 361
- Pratt, G. W., Pointecouteau, E., Arnaud, M., & van der Burg, R. F. J. 2016, A&A, 590, L1

- Pratt, G. W., Arnaud, M., Piffaretti, R., et al. 2010, *A&A*, 511, A85
- Predehl, P., Andritschke, R., Becker, W., et al. 2014, in Society of Photo-Optical Instrumentation Engineers (SPIE) Conference Series, Vol. 9144, 1
- Racca, G. D., Laureijs, R., Stagnaro, L., et al. 2016, in Proc. SPIE, Vol. 9904, Space Telescopes and Instrumentation 2016: Optical, Infrared, and Millimeter Wave, 99040O
- Rasia, E., Ettori, S., Moscardini, L., et al. 2006, *MNRAS*, 369, 2013
- Rasia, E., Lau, E. T., Borgani, S., et al. 2014, *ApJ*, 791, 96
- Reichardt, C. L., Stalder, B., Bleem, L. E., et al. 2013, *ApJ*, 763, 127
- Reiprich, T. H. 2017, *Astronomische Nachrichten*, 338, 349
- Reiprich, T. H., & Böhringer, H. 2002, *ApJ*, 567, 716
- Ribeiro, A. L. B., Lopes, P. A. A., & Trevisan, M. 2011, *MNRAS*, 413, L81
- Richardson, T., & Fairbairn, M. 2013, *MNRAS*, 432, 3361
- Ridl, J., Clerc, N., Sadibekova, T., et al. 2017, *MNRAS*, 468, 662
- Roberts, I. D., Parker, L. C., & Hlavacek-Larrondo, J. 2018, *MNRAS*, 475, 4704
- Romero, C. E., Mason, B. S., Sayers, J., et al. 2017, *ApJ*, 838, 86
- Roncarelli, M., Ettori, S., Borgani, S., et al. 2013, *MNRAS*, 432, 3030
- Roncarelli, M., Gaspari, M., Ettori, S., et al. 2018, *A&A*, 618, A39
- Rossetti, M., Gastaldello, F., Eckert, D., et al. 2017, *MNRAS*, 468, 1917
- Rossetti, M., Gastaldello, F., Ferrioli, G., et al. 2016, *MNRAS*, 457, 4515
- Rozo, E., Bartlett, J. G., Evrard, A. E., & Rykoff, E. S. 2014a, *MNRAS*, 438, 78
- Rozo, E., Evrard, A. E., Rykoff, E. S., & Bartlett, J. G. 2014b, *MNRAS*, 438, 62
- Rozo, E., Rykoff, E. S., Evrard, A., et al. 2009, *ApJ*, 699, 768
- Rudd, D. H., Zentner, A. R., & Kravtsov, A. V. 2008, *ApJ*, 672, 19
- Ruppin, F., Adam, R., Comis, B., et al. 2017, *A&A*, 597, A110
- Ruppin, F., Mayet, F., Pratt, G. W., et al. 2018, *A&A*, 615, A112
- Ryden, B. S., & Gunn, J. E. 1987, *ApJ*, 318, 15
- Rykoff, E. S., Koester, B. P., Rozo, E., et al. 2012, *ApJ*, 746, 178
- Rykoff, E. S., Rozo, E., Busha, M. T., et al. 2014a, *ApJ*, 785, 104
- . 2014b, *ApJ*, 785, 104
- Rykoff, E. S., Rozo, E., Hollowood, D., et al. 2016, *The Astrophysical Journal Supplement Series*, 224, 1
- Salvato, M., Ilbert, O., & Hoyle, B. 2018, *Nature Astronomy*
- Sánchez, C., Carrasco Kind, M., Lin, H., et al. 2014, *MNRAS*, 445, 1482
- Saro, A., Mohr, J. J., Bazin, G., & Dolag, K. 2013, *ApJ*, 772, 47
- Sartoris, B., Biviano, A., Rosati, P., et al. 2014, *ApJ*, 783, L11
- Sartoris, B., Biviano, A., Fedeli, C., et al. 2016, *MNRAS*, 459, 1764
- Sasaki, S. 1996, *PASJ*, 48, L119
- Sayers, J., Golwala, S. R., Mantz, A. B., et al. 2016, *ApJ*, 832, 26
- Schellenberger, G., & Reiprich, T. H. 2017a, *MNRAS*, 469, 3738
- . 2017b, *MNRAS*, 471, 1370
- Schellenberger, G., Reiprich, T. H., Lovisari, L., Nevalainen, J., & David, L. 2015, *A&A*, 575, A30
- Schmidt, R. W., & Allen, S. W. 2007, *MNRAS*, 379, 209
- Schneider, P., van Waerbeke, L., Jain, B., & Kruse, G. 1998, *MNRAS*, 296, 873
- Schuecker, P., Böhringer, H., & Voges, W. 2004, *A&A*, 420, 61
- Sembolini, F., Yepes, G., De Petris, M., et al. 2013, *MNRAS*, 429, 323
- Sembolini, F., Yépés, G., Pearce, F. R., et al. 2016a, *MNRAS*, 457, 4063
- Sembolini, F., Elahi, P. J., Pearce, F. R., et al. 2016b, *MNRAS*, 459, 2973
- Sereno, M. 2007, *MNRAS*, 380, 1207
- . 2015, *MNRAS*, 450, 3665
- Sereno, M., & Ettori, S. 2015a, *MNRAS*, 450, 3633
- . 2015b, *MNRAS*, 450, 3633
- . 2017, *MNRAS*, 468, 3322
- Sereno, M., Ettori, S., Umetsu, K., & Baldi, A. 2013, *MNRAS*, 428, 2241
- Sereno, M., & Umetsu, K. 2011, *MNRAS*, 416, 3187
- Sereno, M., Umetsu, K., Ettori, S., et al. 2018, *ApJ*, 860, L4
- Serra, A. L., Diaferio, A., Murante, G., & Borgani, S. 2011, *MNRAS*, 412, 800
- Shi, X., Komatsu, E., Nagai, D., & Lau, E. T. 2016, *MNRAS*, 455, 2936
- Shi, X., Komatsu, E., Nelson, K., & Nagai, D. 2015, *MNRAS*, 448, 1020
- Shi, X., Nagai, D., & Lau, E. T. 2018, *MNRAS*, 481, 1075
- Shirasaki, M., Lau, E. T., & Nagai, D. 2018, *MNRAS*, 477, 2804
- Shirasaki, M., Nagai, D., & Lau, E. T. 2016, *MNRAS*, 460, 3913
- Shitanishi, J. A., Pierpaoli, E., Sayers, J., et al. 2018, *MNRAS*
- Siegel, S. R., Sayers, J., Mahdavi, A., et al. 2018, *ApJ*, 861, 71
- Simionescu, A., Allen, S. W., Mantz, A., et al. 2011, *Science*, 331, 1576
- Smith, G. P., Mazzotta, P., Okabe, N., et al. 2016, *MNRAS*, 456, L74
- Smith, R. E., Peacock, J. A., Jenkins, A., et al. 2003, *MNRAS*, 341, 1311
- Stanek, R., Rasia, E., Evrard, A. E., Pearce, F., & Gazzola, L. 2010a, *ApJ*, 715, 1508
- . 2010b, *ApJ*, 715, 1508
- Sunyaev, R. A., & Zeldovich, Y. B. 1972, *Comments on Astrophysics and Space Physics*, 4, 173
- Suto, D., Kawahara, H., Kitayama, T., et al. 2013, *ApJ*, 767, 79
- Takizawa, M., Nagino, R., & Matsushita, K. 2010, *PASJ*, 62, 951
- Tanaka, M., Coupon, J., Hsieh, B.-C., et al. 2018, *PASJ*, 70, S9
- Tarrío, P., Melin, J.-B., & Arnaud, M. 2018, *A&A*, 614, A82
- Tashiro, M., Maejima, H., Toda, K., et al. 2018, in Society of Photo-Optical Instrumentation Engineers (SPIE) Conference Series, Vol. 10699, Space Telescopes and Instrumentation 2018: Ultraviolet to Gamma Ray, 1069922
- Tchernin, C., Eckert, D., Ettori, S., et al. 2016, *A&A*, 595, A42
- The LSST Dark Energy Science Collaboration. 2018, arXiv e-prints, arXiv:1809.01669
- The Lynx Team. 2018, arXiv e-prints, arXiv:1809.09642
- The Simons Observatory Collaboration. 2018, arXiv e-prints, arXiv:1808.07445
- Thomas, P. A., Colberg, J. M., Couchman, H. M. P., et al. 1998, *MNRAS*, 296, 1061
- Tinker, J., Kravtsov, A. V., Klypin, A., et al. 2008, *ApJ*, 688, 709
- Truong, N., Rasia, E., Mazzotta, P., et al. 2018, *MNRAS*, 474, 4089
- Umetsu, K., Broadhurst, T., Zitrin, A., et al. 2011, *ApJ*, 738, 41
- Umetsu, K., & Diemer, B. 2017, *ApJ*, 836, 231
- Umetsu, K., Medezinski, E., Broadhurst, T., et al. 2010, *ApJ*, 714, 1470
- Umetsu, K., Zitrin, A., Gruen, D., et al. 2016, *ApJ*, 821, 116
- Umetsu, K., Medezinski, E., Nonino, M., et al. 2014, *ApJ*, 795, 163
- Umetsu, K., Sereno, M., Medezinski, E., et al. 2015, *ApJ*, 806, 207
- Umetsu, K., Sereno, M., Tam, S.-I., et al. 2018, *ApJ*, 860, 104
- Urban, O., Simionescu, A., Werner, N., et al. 2014, *MNRAS*, 437, 3939
- van der Marel, R. P. 1994, *MNRAS*, 270, 271
- van der Marel, R. P., Magorrian, J., Carlberg, R. G., Yee, H. K. C., & Ellingson, E. 2000, *AJ*, 119, 2038
- van Uitert, E., Joachimi, B., Joudaki, S., et al. 2018, *MNRAS*, 476, 4662
- Vazza, F., Angelinelli, M., Jones, T. W., et al. 2018, *MNRAS*, 481, L120
- Vazza, F., Brunetti, G., Kritsuk, A., et al. 2009, *A&A*, 504, 33
- Vazza, F., Eckert, D., Simionescu, A., Brüggen, M., & Ettori, S. 2013, *MNRAS*, 429, 799
- Velliscig, M., van Daalen, M. P., Schaye, J., et al. 2014, *MNRAS*, 442, 2641
- Verdugo, T., Limousin, M., Motta, V., et al. 2016, *A&A*, 595, A30
- Vikhlinin, A. 2006, *ApJ*, 640, 710
- Vikhlinin, A., Kravtsov, A., Forman, W., et al. 2006a, *ApJ*, 640, 691
- . 2006b, *ApJ*, 640, 691
- Vikhlinin, A., Kravtsov, A. V., Burenin, R. A., et al. 2009a, *ApJ*, 692, 1060
- . 2009b, *ApJ*, 692, 1060
- Vikram, V., Chang, C., Jain, B., et al. 2015, *Phys. Rev. D*, 92, 022006
- Voigt, L. M., & Fabian, A. C. 2006, *MNRAS*, 368, 518
- von der Linden, A., Allen, M. T., Applegate, D. E., et al. 2014, *MNRAS*, 439, 2

- Walker, S., Simionescu, A., Nagai, D., et al. 2019, *Space Sci. Rev.*, 215, 7
- Walker, S. A., Fabian, A. C., Sanders, J. S., George, M. R., & Tawara, Y. 2012, *MNRAS*, 422, 3503
- Walker, S. A., Fabian, A. C., Sanders, J. S., Simionescu, A., & Tawara, Y. 2013, *MNRAS*, 432, 554
- White, M., Cohn, J. D., & Smit, R. 2010, *MNRAS*, 408, 1818
- White, S. D. M., Navarro, J. F., Evrard, A. E., & Frenk, C. S. 1993, *Nature*, 366, 429
- Wojtak, R. 2013, *A&A*, 559, A89
- Wojtak, R., & Łokas, E. L. 2010, *MNRAS*, 408, 2442
- Wojtak, R., Łokas, E. L., Mamon, G. A., & Gottlöber, S. 2009, *MNRAS*, 399, 812
- Wojtak, R., Łokas, E. L., Mamon, G. A., et al. 2008, *MNRAS*, 388, 815
- . 2007, *A&A*, 466, 437
- Wojtak, R., Old, L., Mamon, G. A., et al. 2018, *MNRAS*
- Wolf, J., Martinez, G. D., Bullock, J. S., et al. 2010, *MNRAS*, 406, 1220
- Wu, H.-Y., Evrard, A. E., Hahn, O., et al. 2015, *MNRAS*, 452, 1982
- Xu, W., Ramos-Ceja, M. E., Pacaud, F., Reiprich, T. H., & Erben, T. 2018, *A&A*, 619, A162
- Yahil, A., & Vidal, N. V. 1977, *ApJ*, 214, 347
- Yu, L., Nelson, K., & Nagai, D. 2015, *ApJ*, 807, 12
- Zandanel, F., Fornasa, M., Prada, F., et al. 2018, *MNRAS*, 480, 987
- Zhang, Y.-Y., Reiprich, T. H., Schneider, P., et al. 2017, *A&A*, 599, A138
- Zhuravleva, I., Churazov, E., Kravtsov, A., et al. 2013, *MNRAS*, 428, 3274
- Ziparo, F., Smith, G. P., Okabe, N., et al. 2016, *MNRAS*, 463, 4004
- Zuntz, J., Sheldon, E., Samuroff, S., et al. 2018, *MNRAS*, 481, 1149
- Zwicky, F. 1933, *Helvetica Physica Acta*, 6, 110
- . 1937, *ApJ*, 86, 217